Title
SIMPLE BOND RUPTURE REACTIONS IN MULTIPHOTON DISSOCIATION OF MOLECULES

Author
Sudbo, Aa.S.

Publication Date
1978-07-01

Lawrence Berkeley Laboratory
UNIVERSITY OF CALIFORNIA

Materials & Molecular Research Division

FORMATION AND DEGRADATION OF $Cu_{2-x}S$/CdS SINGLE-CRYSTAL HETEROJUNCTIONS: A HIGH-RESOLUTION TRANSMISSION ELECTRON MICROSCOPE STUDY

T.D. Sands
(Ph.D. Thesis)

April 1984

Prepared for the U.S. Department of Energy under Contract DE-AC03-76SF00098

DISCLAIMER

FORMATION AND DEGRADATION OF $Cu_{2-x}S$/CdS SINGLE-CRYSTAL HETEROJUNCTIONS: A HIGH-RESOLUTION TRANSMISSION ELECTRON MICROSCOPE STUDY

T. D. Sands

Materials and Molecular Research Division
Lawrence Berkeley Laboratory
and Department of Materials Science and Mineral Engineering
University of California
Berkeley, CA 94720

This work was supported by the Director, Office of Energy Research, Office of Basic Energy Sciences, Materials Science Division of the U.S. Department of Energy under Contract No. DE-AC03-76SF00098.

TABLE OF CONTENTS

ABSTRACT

The $Cu_{2-x}S$/CdS photovoltaic device is the most thoroughly studied and developed polycrystalline thin-film solar cell. However, many of the fundamental relationships between processing, microstructure, and device performance are essentially unknown. Further improvement of this device will require an understanding of the effects of surface texture, heat treatments, and long term exposure on device efficiency and stability. Critical to understanding these effects is the determination of the $Cu_{2-x}S$/CdS interface morphology and the phase distribution in the $Cu_{2-x}S$ absorber.

In this study electron-optical methods are applied to the structural characterization of single-crystal $Cu_{2-x}S$/CdS heterojunctions prepared by the aqueous ion-exchange process. Results obtained by scanning electron microscopy, transmission electron microscopy and diffraction, and cross-sectional high-resolution transmission electron microscopy (XHRTEM) are combined to develop a detailed description of the structural evolution of the $Cu_{2-x}S$/CdS heterojunction.

The XHRTEM images reveal the two-phase nature of the Cu_2S absorber. The tetragonal phase, a high-pressure polymorph of low chalcocite (Cu_2S), is found to form the metallurgical junction with CdS if the local surface orientation is nearly basal. However, only low chalcocite is detected in the absorber layer if the surface is steeply inclined to the basal plane. These results are rationalized on the basis of lattice misfit, structural compatibility, and the

nucleation of h.c.p.-to-f.c.c. transformation dislocations. Lattice misfit considerations are also found to be useful in explaining the morphology of degraded heterojunctions. In particular, the observed shape and orientation of djurleite ($Cu_{1.97}S$) domains in low chalcocite are consistent with the minimization of lattice mismatch. The implications of these results for the reproducible fabrication of high efficiency $Cu_{2-x}S$/CdS solar cells are discussed.

1. INTRODUCTION

1.1 Objective

First developed nearly thirty years ago, the thin-film $Cu_{2-x}S/CdS$ photovoltaic cell has become the prototype for several promising thin-film heterojunction solar cells with II-VI collectors. Unfortunately, this device has not been adequately modeled due to a lack of experimental data describing the interface morphology and the phase distribution in the $Cu_{2-x}S$ absorber layer. This information would be invaluable in explaining observations such as the sensitivity of device efficiency to surface texture[1] and the rapid degradation of short-circuit current output during exposure to air and water vapor at operating temperatures.[2] In this investigaton, electron-optical techniques have been applied in an effort to both describe and understand the structural evolution of the $Cu_{2-x}S/CdS$ heterojunction at the atomic level.

1.2 The Photovoltaic Effect in Absorber-Window Solar Cells

1.2.1 Device Structure

A solar cell is a device which directly converts a significant fraction (typically 5 to 25 percent) of the power in the incident solar radiation to usable electric power. In order to appreciate the implications of this study for the operation of a specific solar cell, the copper sulfide-cadmium sulfide cell, the reader must possess an understanding of the basic mechanism of the photovoltaic effect in semiconductor solar cells. The following physical description applies to the semiconductor heterojunction device in absorber-window

configuration. However, the photovoltaic effect in cells with other configurations (e.g., homojunction, semiconductor-insulator-semiconductor, and surface barrier) is similar in nature. A practical approach to solar cell design principles and applications can be found in the book by Green.[3] For a more rigorous treatment, the reader is referred to the book by Fonash.[4]

At the most fundamental level, a semiconductor solar cell is a device in which energy from an incident photon is used to promote a "ground state" (bonding) electron to a higher mobilized (conduction band) state. A spatial asymmetry in the device then separates the mobile electron from the resulting vacant site (mobile "hole"). Those photogenerated electrons and holes which successfully avoid recombination must lose their excess energy by another process. In the simplest case, the excess energy is given to an external load. Through this process, the energy in an incident photon is directly converted into usable electrical energy.

From the preceding discussion it is evident that the two most critical constituents of a solar cell are the absorber, a medium in which photons can efficiently transfer their energy to electrons, and the junction, a portion of the device which effectively separates the mobile electrons from the vacant bonding sites. The junction is generally formed by intimate contact of two semiconductors of the same material but different conductivity types (anisotype homojunction) or by the combination of two materials with different structures and compositions (heterojunction). It should be noted that the efficiency

of a heterojunction cell is predicted to be less than or equal to the efficiency of a homojunction cell made entirely of the absorber material.[5] Thus, the motivation for choosing the heterojunction configuration is based on practical considerations such as materials availability, restrictions in materials properties, or simplicity of fabrication.

The most commonly employed heterojunction configuration is the anisotype semiconductor-semiconductor heterojunction. In this device a semiconductor which can act as an absorber is placed in contact with a semiconductor of opposite conductivity type. The later semiconductor is called the collector since it acts to "collect" the minority carriers (e.g., electrons in a p-type absorber) which are photogenerated in the absorber layer. This collector layer may also be referred to as a window since most commonly employed collector materials are somewhat transparent to solar photons.

To continue this discussion at a more sophisticated level, the band diagram construction is required. In the following the absorber material is taken to be p-type (hole conduction dominates) and the window is assumed to be n-type (electron conduction dominates). The p-type absorber configuration is preferred since minority carrier electrons in p-type material are generally more mobile than minority carrier holes in n-type material. As will be shown below, these photogenerated minority carriers in the absorber play a central role in anisotype heterojunction cell operation.

Consider first the band diagrams of the isolated absorber (p-type, small bandgap) and window (n-type, large bandgap). The electron affinities, χ, work functions, ϕ, bandgaps, E_g, and Fermi levels, E_F, are labeled in Fig. 1.1. In this diagram, nondegenerate semiconductors are depicted (Fermi levels lie within the forbidden gaps). As the semiconductors are brought together, the Fermi levels, or electrochemical potentials for electrons, must equalize. The resulting equilibrium band diagram which neglects interface states and gradients in semiconductor properties is known as the ideal Anderson model.[6] Note that for the values of electron affinities chosen in Fig. 1.1 there is a conduction band jump of magnitude $X_w - X_a$. Similarly, if X_a were greater than X_w, a conduction band spike would result.

Perhaps a more physically intuitive way to rationalize the band diagram of Fig. 1.1 is to consider electron and hole flows immediately after contact. At the instant of contact a reservoir of holes is placed next to a reservoir of electrons and the "flood gate" is lifted. Electrons and holes then begin to flow across the junction. However, each electron which crosses the junction leaves behind a fixed positive charge, the donor ion core (similarly for holes which flow into the n-type material). Consequently, an electric field which opposes further intermixing is created. The potential difference due to this "built-in" field quickly reaches a magnitude ($\psi_o = \phi_a - \phi_w$) which prevents further <u>net</u> flow of electrons and holes. Attainment of this equilibrium condition is equivalent to the equalization of the Fermi level for electrons.

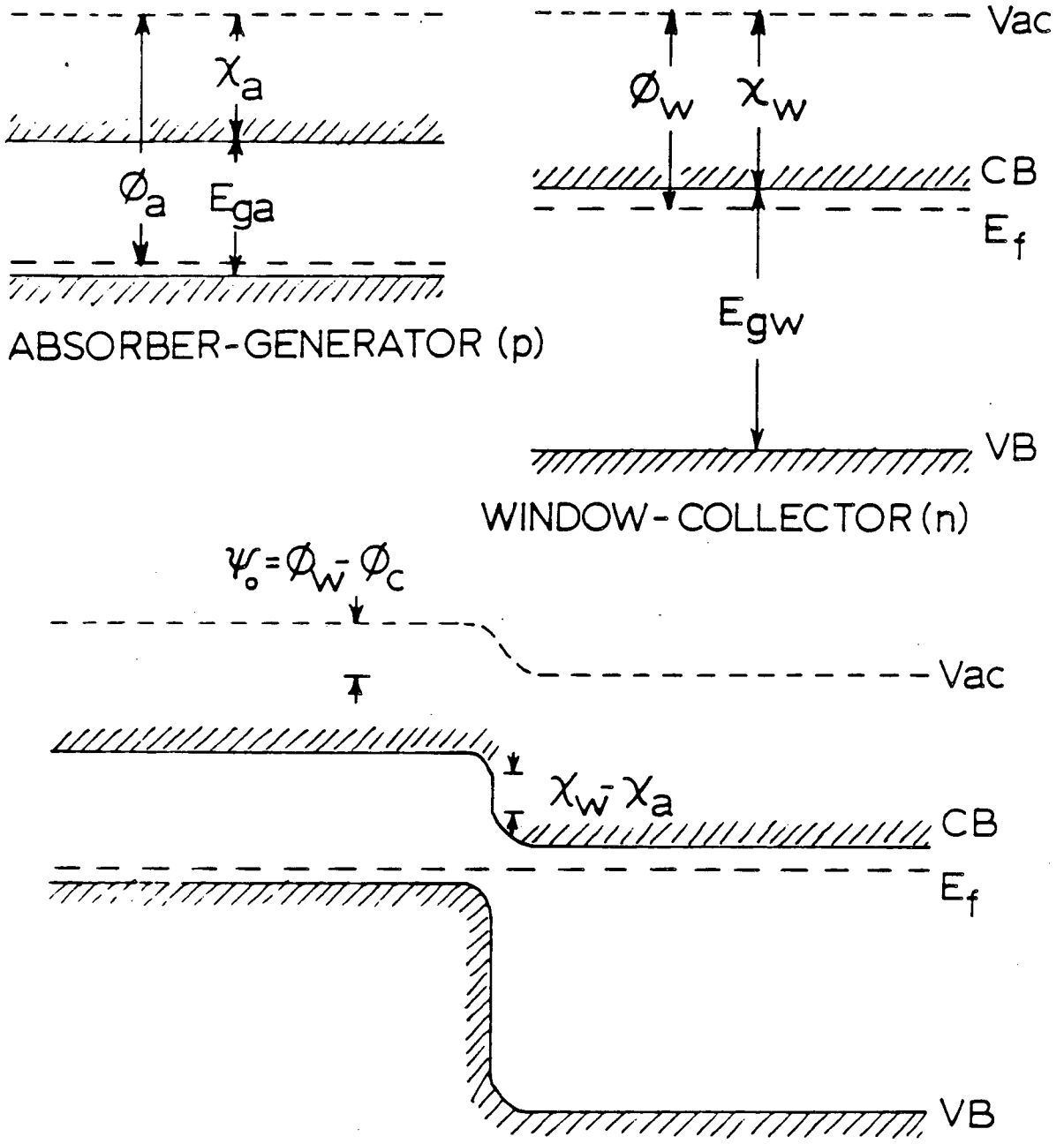

Fig. 1.1. Electron energy band diagrams of absorber and window semiconductors before (top) and after (bottom) intimate contact. Parameters are defined in text. XBL 843-1015

1.2.2 Dark Characteristics

Consider now this heterojunction in an unilluminated state and in thermal equilibrium with zero applied voltage. A small number of electrons will be thermally generated in the absorber and will flow "downhill" into the collector (the thermally generated holes in the collector can be neglected since the collector bandgap has been assumed to be large compared to the absorber bandgap). Since there is zero net flow in equilibrium, this thermally generated flow must be cancelled by the thermally activated flow of electrons over the barrier from the collector into the absorber.

If a negative voltage is applied to this device, the barrier to electron flow becomes larger, thereby reducing the thermally activated flow of electrons from collector to absorber (proportional to exp [qVapplied/kT] where q is the magnitude of the electronic charge and k is Boltzmann's constant). However, since the thermally generated electron flow in the reverse direction is essentially independent of applied voltage, the net current flow is approximately equal to this constant thermally generated current, also known as the reverse saturation current, I_o. The reverse saturation current is proportional to the junction area and is a sensitive function of the absorber bandgap (since I_o must counteract the thermally generated current from the absorber at zero bias).

In forward bias ($V_{applied} > 0$) the barrier to electron flow is reduced. Thus, majority carrier flow from collector to absorber dominates resulting in a forward current which depends exponentially

on $V_{applied}$. This description of the ideal dark characteristics leads to the familiar expression for diode behavior;

$$I = I_o \, (\exp[qV_{applied}/kT] - 1).$$

Real solar cells generally display a more complicated behavior. A discussion of these complications is beyond the scope of this introduction. The interested reader can find such discussions in any book on semiconductor device electronics, including the books by Green[3] and Fonash.[4]

1.2.3 Illuminated Characteristics

Under illumination, electron-hole pairs are generated in the absorber. The minority carrier electrons generated within a diffusion length of the junction have a high probaility of being collected. The collected electrons constitute a light-generated current I_L. If the cell is short-circuited the built-in potential, ψ_o, will impede electron flow in the opposing direction. If the cell is operated in an open-circuit condition the current in the external circuit must be zero. Therefore, the photogenerated flow to the collector, I_L, must be cancelled by a lowering of the barrier to flow of electrons from the collector. This reduction in junction potential difference is the open-circuit voltage, V_{oc}. Note that if a portion of the photo-generated current recombines before crossing the junction, then the open-circuit voltage required to produce sufficient bucking current is reduced.

This simplistic model can be described by the superposition of the light-generated current and the dark characteristics (Fig. 1.2). Thus,

$$I = I_o \, (\exp[qV/kT]-1) - I_L .$$

The power generated by this device is the product of the current and voltage at the operating point. Maximum power is given by the product of I_{sc}, V_{oc}, and the fill factor, FF. The fill factor of merely a measure of the "squareness" of the I-V curve. High quality cells have fill factors of between 0.6 and 0.8. Excessive series resistances or small shunt resistances will reduce the fill factor dramatically. The cell efficiency, η, is defined as the ratio of the electrical power output to the incident solar power (~100 mW/cm^2, maximum). Typical values of V_{oc}, I_{sc}, and η are 0.4-0.8V, 10-40 mA/cm^2, and 5-25 percent, respectively.

1.3 Materials Criteria for Effective Absorber-Window Combinations

As was mentioned in Section 1.2.1, the primary advantage of the heterojunction configuration is materials flexibility. The designer of a heterojunction cell can utilize materials with desirable properties which cannot be exploited in the homojunction configuration. Thus, materials such as Cu_2S, Cu_2O, and CdS which are available in only one conductivity type can be employed. Some of the materials properties which must be considered when choosing compatible materials for absorber-window cells are described below.

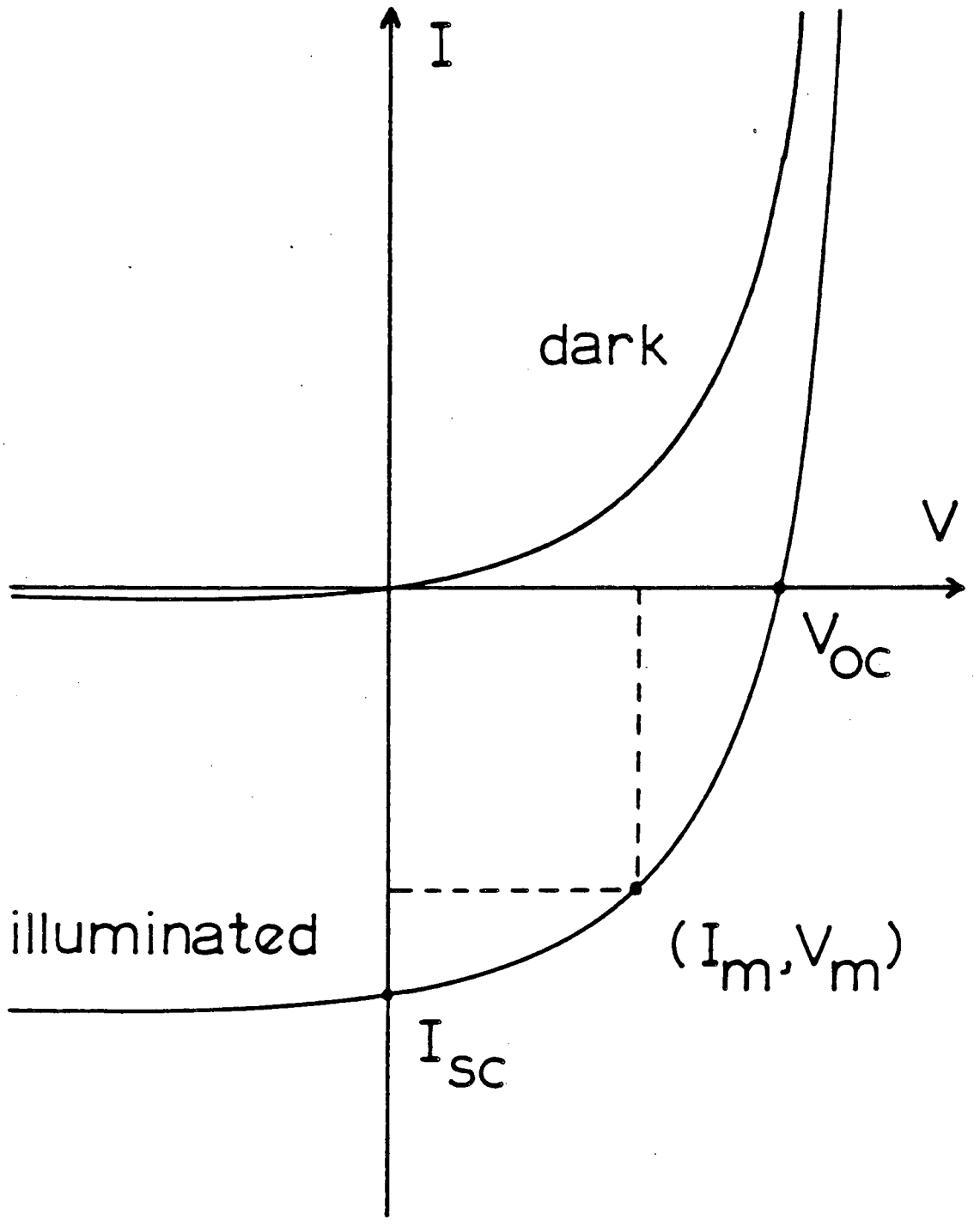

Fig. 1.2 Current-voltage characteristics of ideal solar cell in dark and illuminated. Parameters are defined in text. (Im,Vm) is maximum power point. XBL 843-1014

1.3.1 Bandgaps

The bandgap of the absorber material must be well matched to the solar spectrum. If the gap is too wide ($\geq$2 eV), then few of the incident photons will have sufficient energy to create electron-hole pairs. If the bandgap is too narrow ($\leq$1 eV), then the attainable open-circuit voltage will be small (since $I_0 \propto \exp[-Eg/kT]$). In addition, if the bandgap is narrow, much of the incident energy is wasted. For example, if an incident photon of energy 2 eV creates an electron-hole pair in an absorber with a bandgap of 1.1 eV, the additional 0.9 eV is shared between the electron and hole as kinetic energy. This excess kinetic energy is rapidly dissipated as heat and is not recoverable in the external circuit. It can be shown[7] that efficient solar cells must have absorber bandgaps in the range of 1.0 to 2.0 eV.

If the collector layer is to be used as a window, the bandgap should be a minimum of 2.5 eV. In this configuration ("backwall"), the window layer does not absorb a significant amount of light so that the photons can be absorbed near the junction in the absorber material, thereby increasing the collection efficiency. If the collector is used in the "frontwall" configuration (photons impinge on the outer surface of the absorber), the collector bandgap becomes a less critical parameter. However, some frontwall cells utilize large bandgap collectors and high-reflectivity back contacts so that photons can make a second pass at the absorber. Window layers can also be used to confine photogenerated minority carriers to the junction

region, away from high-efficiency recombination sites at the cell surfaces. For example, a large bandgap p-type material on the front surface of a frontwall cell creates a barrier in the conduction band that will prevent photogenerated electrons in the absorber from recombining at the outer surface. This barrier is often called a "minority carrier rejection potential."

1.3.2 Photon Absorption Length in the Absorber

Perhaps the most critical materials parameter is the absorption length in the absorber. A shorter absorption length allows the use of a thinner absorber layer. A thinner absorber implies that higher resistivities and shorter minority carrier diffusion lengths can be tolerated.

Photon absorption depends exponentially on penetration distance. This dependence is described by an absorption coefficient α which is a function of photon wavelength λ. Therefore, the light intensity, $I(x)$, as a function of distance into the absorber, x, is

$$I(x,\lambda) = I_0(o,\lambda)\exp[-\alpha(\lambda)\ x] \quad .$$

For a given λ, the intensity $I(x)$ drops to I_0/e at a depth of $1/\alpha$. Thus, for photons of wavelength 0.75 μm, the required absorber thicknesses are ~10 μm and ~0.2 μm for Si and Cu_2S, respectively. Consequently, a much shorter minority carrier diffusion length can be tolerated for Cu_2S.

1.3.3 Electron Affinity

To form an effective p-absorber/n-window pair the electron affinities of the two materials should be nearly equal. As can be deduced from the ideal Anderson model (Fig. 1.1), if the electron affinity of the window-collector is less than the electron affinity of the absorber, an undesirable conduction band spike will result. It can also be shown[5] that if $X_a < X_w$, the conduction band jump will reduce the maximum available open circuit voltage.

1.3.4 Lattice Mismatch

Since a heterojunction consists of two different materials there is, in general, lattice misfit at the metallurgical junction. There may, in fact, be no obvious relationship between the structures of the two materials, in which case the interface would be described as incoherent. However, in the crystalline semiconductor heterojunctions of interest, there is usually a simple orientation relationship and preferred interfacial habit plane (i.e. an "epitaxial" relationship). This effect can be attributed to the dominance of covalent bonding so that most semiconductors have similar structures which are based on tetrahedral bonding (e.g., diamond, wurtzite, and zincblende).

In the case of a very thin layer of one material on a thick substrate of a different material, the lattice misfit, if less than ~5 percent, may be accommodated elastically. However, as the overlayer becomes more than a few layers thick, the elastic accommodation energy increases to the point at which the introduction of misfit dislocations becomes favorable.[8] Beyond this point,

accommodation of misfit is shared between dislocations and elastic strain, with a larger fraction of the misfit being accommodated by misfit dislocations as the overlayer becomes thicker. Of course, this description assumes that misfit dislocations are available, which may not always be a valid assumption.

For thick epitaxial overlayers (overlayer lattice parameter smaller than substrate lattice parameter), a network of cracks may form to reduce the long range stresses which are not eliminated by misfit dislocations. In the case of overlayers which share a sublattice with the substrate (i.e. a "topotaxial" relationship), which is the situation when one sublattice in the surface region of a compound semiconductor is chemically exchanged for another, a network of cracks may form if the overlayer sublattice which is preserved is smaller than the corresponding sublattice in the substrate.

In the simple case of one-dimensional misfit at an epitaxial interface with the misfit defined by $\delta = (a_1 - a_2)/a_1$, where a_1 is the unstrained lattice spacing of the substrate and a_2 is the unstrained lattice spacing of the overlayer, the long range stresses may be completely canceled by the introduction of a set of misfit dislocations in edge orientation with spacing $D \cong |\vec{b}| / \delta$, where $\vec{b}$ is the Burgers vector of the dislocation. Here it is assumed that $\vec{b}$ lies in the interface plane and is parallel to the a-axes of both crystals. In the more general case of two-dimensional misfit, two or more arrays of dislocations are necessary to eliminate the long range stresses.

Dislocations in semiconductors are often depicted as rows of "dangling bonds." These unsatisfied bonds can give rise to electron states in the bandgap at the metallurgical interface. In order to obtain a rough estimate for the areal density of interface states, assume a square array of dislocations with spacing $D \cong |\vec{b}|/\delta$. where $|\vec{b}| \cong a$, the average lattice parameter in the interface plane, and $\delta \cong \Delta a/a$. Therefore, in an area D^2 there is a total dislocation line length of 2D. If the linear density of unsatisfied bonds on a dislocation line is assumed to be approximately 1/a (an overestimate in the case of significant reconstruction), and if each unsatisfied bond contributes a single interface state, then the areal density of interface states, N_i, is $(1/a) \cdot (2D/D^2) = 2\Delta a/a^3$. Thus, the density of localized interface states is expected to be between approximately 10^{13} and 10^{14} cm^{-2} for a lattice mismatch of 5 percent. It can be shown that a density of $10^{13} cm^{-2}$ can seriously affect solar cell performance.[5]

Several interfacial effects can limit cell performance (Fig. 1.3). Since the metallurgical junction often coincides with the space charge region of the heterojunction, any interface states due to lattice mismatch or differing coefficients of thermal expansion may act as recombination sites for photogenerated carriers. Secondly, lattice defects at the interface may also act as short-circuit diffusion paths for the electron bucking current flowing from collector to absorber, thereby increasing I_o and reducing V_{oc}. A third possibility is that the interface states (including those due to cross-diffusion of

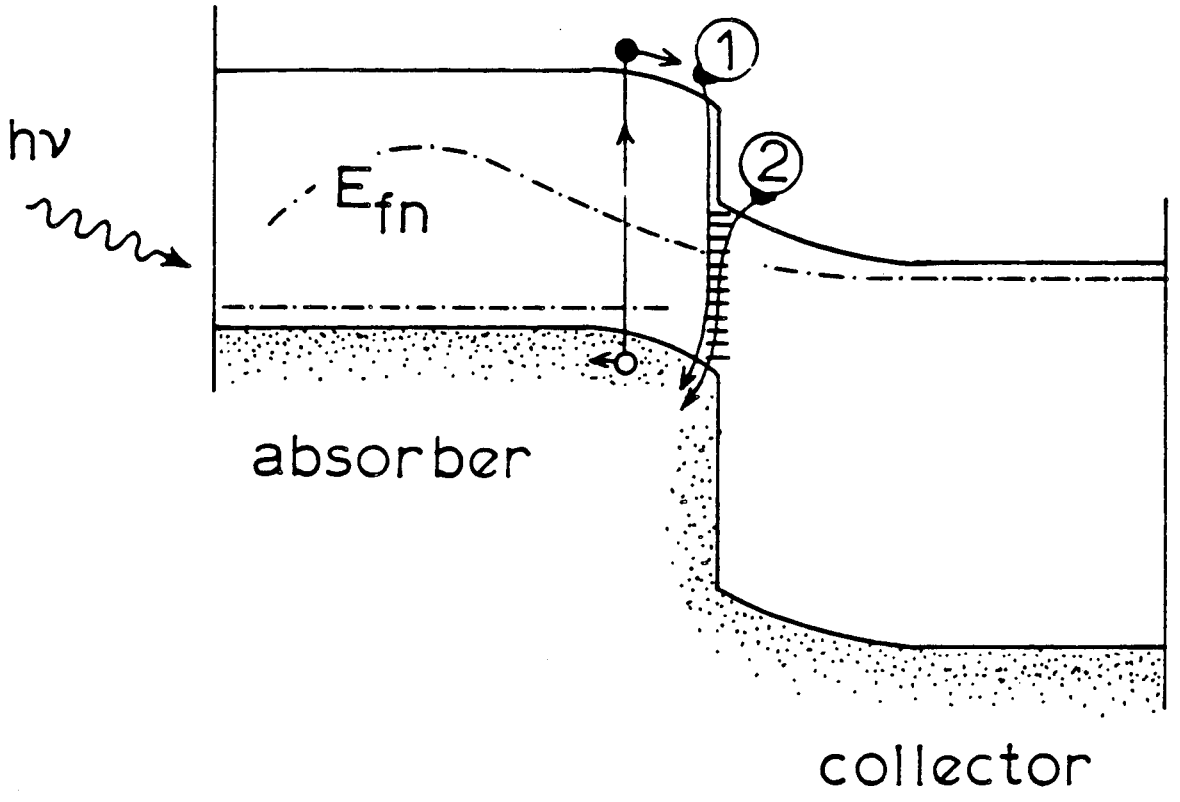

Fig. 1.3 Recombination via interface states. Path 1 is recombination of photo-generated electrons. Path 2 is shunting of electron bucking current through interface states. E_{fn} is electron quasi-Fermi level. XBL 843-1013

atomic species) store charge with the effect of altering the shape of the potential barrier. Unsatisfied bonds can also be electrically inactive if they are passivated by cross-diffusion or by impurities introduced during fabriation. It should also be mentioned that interfacial dislocation arrays can exist outside of the space-charge region. For example, if the absorber consists of two phases, the interfaces between these two materials may contain dislocations. If these dislocations were in a field-free region of the absorber they might act as very efficient recombination centers since there would be no field pulling the carriers through the array as there is in the space-charge region.[9]

1.3.5 Economic Considerations

Above all, the most important reasons for choosing the heterojunction configuration over the simpler homojunction configuration are economic. For instance, the principal reason that CdS is widely used is that thin textured CdS films can be formed on large area substrates with techniques such as evaporation, sputtering, and spraying. These techniques are inexpensive and are well suited to mass production. However, since CdS cannot be made p-type, an anisotype solar cell utilizing CdS must be a heterojunction.

Another material which is available in only one type, cuprous sulfide (p-type) has proven to be reasonably compatible with CdS in the areas discussed above. This $Cu_{2-x}S$/CdS cell is the subject of the next section.

1.4 The Copper Sulfide-Cadmium Sulfide Solar Cell

The $Cu_{2-x}S$/CdS solar cell has a history dating back to 1954 when Reynolds et al.[10] first detected a photovoltaic effect in single crystals of cadmium sulfide with indium base electrodes and various metallic counter electrodes. The cells with copper counter electrodes yielded the highest efficiencies (~1.5 percent). It was not until 1965 that Cusano et al.[11] suggested that the CdS cell was actually a heterojunction between Cu_2S and CdS.

Development of polycrystalline $Cu_{2-x}S$/CdS cells began in 1956 with the work of Carlson[12] and continued steadily through the 1960's and 1970's. During this time the "Clevite process" for polycrystalline cell fabrication was developed.[13] The most notable feature of this process was the fabrication of the $Cu_{2-x}S$ layer on evaporated CdS substrates by ion exchange in a hot (~90°C) aqueous bath of Cu_2Cl_2. Thus, the metallurgical interface was formed within the CdS crystal, thereby avoiding atmospheric contamination of the interface. Thin-film frontwall cells fabricated by this process have achieved efficiencies of greater than 9 percent in the laboratory.[14]

Recently, several other techniques for $Cu_{2-x}S$/CdS solar cell fabrication have shown promising results. Besides thermal evaporation, CdS layers may be prepared by sputtering, screen-printing and spraying. Although the aqueous ion exchange process ("wet process") currently gives the best results for $Cu_{2-x}S$ layer fabrication, several other techiques including the "dry process" and reactive sputtering have been explored. The various heterojunction fabrication techniques are

reviewed in detail by Hill[15] and Martinuzzi.[16] Since the emphasis here is on the fundamental characteristics of the $Cu_{2-x}S$/CdS heterojunction rather than device engineering, only the most established fabrication technique, a modified version of the Clevite process, will be discussed below.

1.4.1 Fabrication and Structure of the Evaporated and "Wet-Processed" Cell

The most attractive feature of the Cu_2S/CdS solar cell is that cells with reasonable efficiencies ($\geq$5 percent) can be fabricated by simple, low-temperature processes which are suitable for mass production. The first step in one such process, the Clevite process, is the thermal evaporation of CdS onto a conducting substrate. One of the most commonly used substrates for frontwall cells is zinc-coated copper sheeting. The high reflectivity of this substrate (after heat treatment) increases the probability of photon absorption for thin layers of copper sulfide. Also, the thermal expansion coefficient of zinc-coated copper is well matched to the thermal expansion coefficient of CdS ($\sim 5 \times 10^{-6}$ K^{-1}).[16] For backwall cells, the CdS is deposited onto a glass substrate coated with a nearly transparent conductor such as SnO_2.[17] The highest quality films are formed on substrates kept at 200-300°C during deposition. Film thicknesses of 10 to 30 μm are required to avoid short-circuiting through pin holes in the completed cell. The outstanding feature of these films is that they show a very strong preferred orientation with the c-axes of the CdS grains normal to the substrate (for evaporation at normal incidence)

with a standard deviation of 10 to 15°.[18] The grains are columnar so that most of the grain boundaries are normal to the substrate. Grain diameters are typically ~1 μm. This small grain size can be tolerated due to the relatively small thickness of the Cu_2S absorber (0.1 to 0.3μm). In other words, most of the photogenerated minority carriers can cross the junction without encountering a grain boundary.[19]

To minimize the contribution of the CdS collector to the series resistance of the cell, the resistivity of the CdS must be reduced to approximately 10 Ω-cm. This level of resistivity can be achieved by the introduction of sulfur vacancies or by intentional doping with donor impurities such as indium.[20]

Before heterojunction formation, the CdS surface is cleaned and textured by an etching treatment in concentrated HCl. The texture of the etched surface serves to efficiently trap the incident light. The etchant also exposes CdS grain boundaries, thereby dramatically increasing the surface area of the cell.[21]

The copper sulfide layer is formed by a short (5 to 10 sec) immersion in an aqueous bath of Cu_2Cl_2 (6 g/l) and NaCl (2 g/l) at 90-99°C.[22] The global reaction,

$$CdS + Cu_2Cl_2 \rightleftarrows Cu_2S + CdCl_2$$

($\Delta G^\circ \cong -5.22$ J/mole Cu_2S),[15]

is manifested by the exchange of Cu^{+} and Cd^{++} ions, leaving the sulfur network essentially intact. Thus, the resulting $Cu_{2-x}S$ film is topotaxial. The pH of the exchange solution is often adjusted to increase film texture. Low pH solutions ($\leq$pH 4) lead to enhanced penetration down grain boundaries and an overall linear growth rate. Higher pH solutions result in a diffusion-limited parabolic growth rate.[23]

The desired copper sulfide phase, low chalcocite, is a p-type deficit semiconductor (deficient in cations) with a hole concentration approximately equal to the concentration of copper vacancies. The near-optimum bandgap (1.2 eV), high absorption coefficient (10^5 cm^{-1} at 750 nm) and adequate minority carrier diffusion length (~0.3 μm) of low chalcocite contribute to its effective operation as an absorber layer.[24] Unfortunately, copper deficiencies as slight as 0.5 percent result in the formation of djurleite, $Cu_{1.97-1.94}S$,[25] a phase with inferior photovoltaic properties.[26,27]

To avoid the formation of djurleite, the presence of Cu^{++} must be avoided in the ion exchange solution. Procedures such as bubbling an inert or reducing gas into the solution[22] and purifying the Cu_2Cl_2 with an HCl rinse[1] help to insure the formation of low chalcocite. The plating bath temperature is also important. Temperatures lower than ~90°C result in the formation of djurleite.[27] Consequently, the CdS substrates are sometimes pre-heated to reaction temperature to avoid thermal inertia effects.[1,28] The stoichiometry of the copper sulfide layer can also be adjusted following conversion

by the evaporation of a thin layer (5-8 nm) of copper onto the $Cu_{2-x}S$ surface.[29] Following heat treatment, the Cu_2S stoichiometry is restored. The main disadvantage of this technique is that the amount of copper deposited should be individually tailored to each cell to realize a significant improvement. In fact, the optimum composition of the $Cu_{2-x}S$ layer is probably not Cu_2S, but rather ~$Cu_{1.997}S$ due to the increased propensity for electrochemical degradation at compositions close to $Cu_{2.000}S$.[30]

Following $Cu_{2-x}S$ layer formation the heterojunction is usually given a heat treatment in air to improve the cell response. The reason for the improvement is not clear, although several explanations have been proposed. Using spectral response measurements, Caswell et al.[31] showed that a heat treatment in air results in the formation of a copper-diffused photoconductive region in the CdS near the junction. This photoconductive region may result from the trapping of holes at levels induced by the diffused copper. These trapped holes would increase the positive charge on the CdS side of the depletion region, thereby reducing the depletion layer width. The reduced depletion layer width would result in an increased electric field which might act to reduce the recombination of photogenerated carriers at interface states.[32]

The need for an air atmosphere during heat treatment is usually rationalized by assuming that a layer of Cu_xO is formed at the surface of the copper sulfide. This large bandgap, p-type copper oxide would result in the formation of a minority carrier rejection

potential at the surface, thereby increasing the current collection efficiency of the cell.[33]

While these effects are probably real, recent results with single-crystal devices suggest that the effects of the heat treatment depend to a great degree on the surface texture of the CdS substrate.[1,34] In fact, the best single-crystal cells do not show improvement after heat treatment.[1] These surface texture effects will be explored in more detail in Section 1.4.2.

Contacts to the copper sulfide are generally made with an Au-Cu or Cu-Cr-Pb mixture. The cell is then coated with an anti-reflection layer such as SiO_x or Ta_2P_5 (frontwall configuration) and encapsulated hermetically in glass. A schematic diagram of a completed frontwall cell is presented in Fig. 1.4.

1.4.2 Effect of Surface Texture on Device Performance

As described in the previous section, CdS is etched in HCl prior to $Cu_{2-x}S$ barrier formation. This etching treatment exposes a fresh surface for conversion to $Cu_{2-x}S$. The HCl etch also creates a heavily textured surface which enhances light trapping, thereby improving the short-circuit current output of the cell.[21,35,36] This improvement may be partially cancelled by the reduction in V_{oc} due to an increase in junction area.[21,23,35,36]

Since $Cu_{2-x}S$ and CdS have different crystal structures (see Section 2.), the density of misfit dislocations, and hence "dangling bonds," depends on the local orientation of the interface plane. Therefore, the specific crystallographic nature of the surface texture

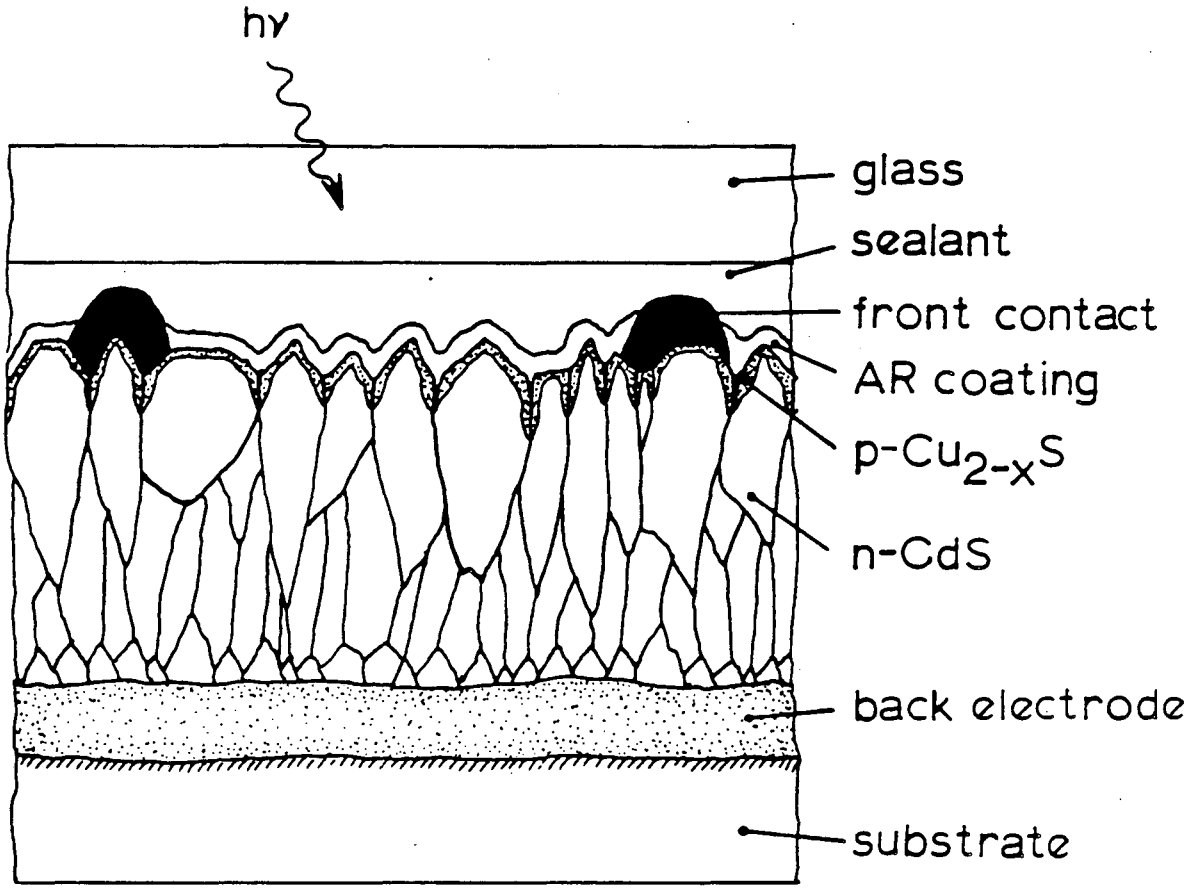

XBL 843-1012

Fig. 1.4 Schematic cross-section of polycrystalline $Cu_{2-x}S$/CdS solar cell.

will also affect device performance. The surface crystallography of etched CdS has been described by Wolff et al.[37] These authors show that the etched cadmium basal surface (0001), contains hexagonal etch pits. The etch pit faces are probably $\{1\bar{1}0\ell\}$-type planes as found on the surface of epitaxially grown CdS.[38] Etch pits with pointed bottoms are due to preferential etching of dislocations. A flat basal bottom results when the dislocation or other defect has been etched away. Unlike the etched cadmium surface, the etched sulfur surface $(000\bar{1})$, contains no large basal facets and is instead composed of hexagonal pyramids or hillocks. The surface crystallography of the hillocks can vary depending on whether the etching is concave or convex.[37] The basic crystallographic features of the etched $(000\bar{1})$ and (0001) faces are illustrated in Fig. 1.5.

The density of Cu_2S/CdS interface states as a function of interface orientation has been estimated by Cheng and Jones[39] and Jones et al.[40] However, these authors have assumed that the copper sulfide phase is low chalcocite for all orientations and they have neglected to account for the actual structure of low chalcocite. For example, the 60° large-angle grain boundary (rotation about the c-axis) described by Cheng and Jones[39] is more properly termed an "orientation domain boundary" or twin (see Section 10.2). Since the sulfur sublattice is continuous across this boundary, the effect of this domain boundary on device performance is probably negligible compared with the effect of a large-angle grain boundary in the sulfur sublattice.

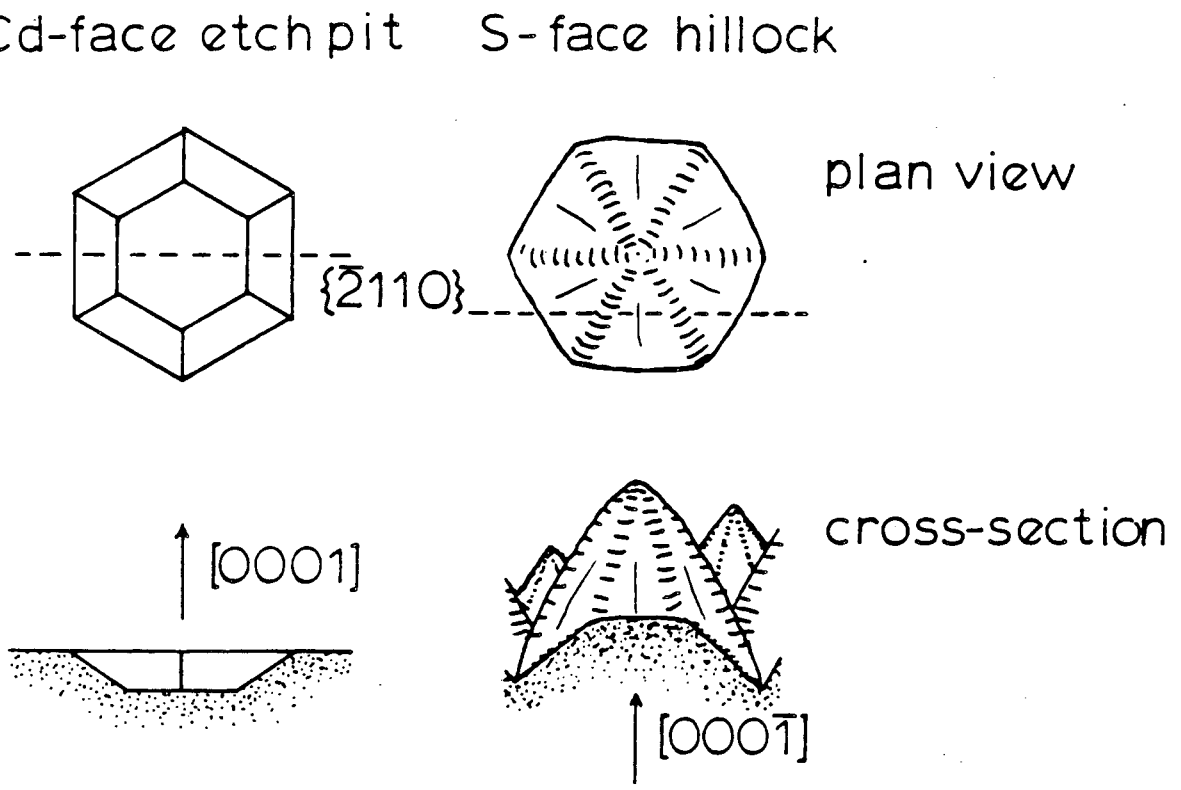

Fig. 1.5 Surface features of etched CdS. XBL 843-1011

Recent work with single-crystal $Cu_{2-x}S$/CdS devices has emphasized the importance of surface texture on device performance. Oktik et al.[1] found that heterojunctions formed on the faceted hillocks of the etched $(000\bar{1})$ surface showed good photovoltaic characteristics in the as-prepared state. Heat treatment of these devices only degraded their characteristics. Heterojunctions formed on etched $(000\bar{1})$ surfaces with terraced hillocks showed poor efficiencies in the as-prepared state. Heat treatment improved the photovoltaic characteristics of these cells. However, the efficiencies of the terraced cells after heat treatment remained well below the efficiencies of the as-prepared faceted cells.

The effect of etching time on surface morphology was also investigated. Oktik et al.[1] found that a 30 second etch in concentrated HCl resulted in the desired faceted hillocks. Since these etching studies were performed on single crystals, the CdS surface was polished mechanically before etching. The mechanically damaged surface layer was found to consist of polycrystalline sphalerite CdS. The presence of this sphalerite surface layer may, in part, explain the results of Cheng et al.[34] These authors found that heterojunctions formed on polished CdS surfaces demonstrated poor response to a scanning light spot, whereas heterojunctions formed on adjacent etched surfaces showed higher response.

It is clear from these recent results that surface texture is one of the most important factors determining the performance of $Cu_{2-x}S$-CdS solar cells. Furthermore, the behavior of $Cu_{2-x}S$/CdS

solar cells cannot be accurately modeled until the structural nature of the $Cu_{2-x}S$/CdS interface is revealed. In particular, the interface morphology and the $Cu_{2-x}S$ phase distribution as a function of local surface orientation must be determined.

1.4.3 Degradation of Short-Circuit Current Output

Degradation of short-circuit current is one of the major problems with $Cu_{2-x}S$/CdS devices. Extended exposure to a combination of air and water vapor at elevated temperatures leads to a rapid decline in I_{sc}.[2,41-44] This degradation can be reversed by a hydrogen heat treatment. Both degradation in moist air and recovery in hydrogen can be described by the exponential variation of I_{sc}:[42,44]

$$I_{sc} = I_{sc_o} \exp[\pm(t/\tau)^{1/2}]$$

where the minus sign corresponds to degradation. The time constant varies from ~300 minutes for degradation at 178°C[42] to ~4 x 10^5 minutes for degradation at 70°C.[44] This behavior has led several authors to speculate that the fundamental degradation/recovery mechanism is the surface oxidation/reduction of $Cu_{2-x}S$.[26,42,44-47] Oxidation of Cu_2S in moist air has been shown to increase the bandgap and decrease the minority carrier diffusion length in the absorber layer.[2] These changes in electrical and optical properties are concomitant with a change in structure from the low chalcocite phase (Cu_2S) to the djurleite phase ($Cu_{1.97-1.94}S$).[48] In addition, Peterson and Washburn[9] propose that the dislocation array

at the low chalcocite-djurleite interface may greatly enhance the recombination of photogenerated minority carriers. Formation of copper oxide at the surface has not been detected directly but has been inferred from electrochemical measurements.[22,26] Fortunately, this mode of degradation can be slowed by glass encapsulation.[44]

A second mode of degradation involves the electrochemical decomposition of the copper sulfide layer at operating voltages above 0.33V.[30,49] When electrochemical degradation is operative, copper nodules form at the front-surface electrode in contact with the $Cu_{2-x}S$ layer. These nodules may short-circuit the cell if they penetrate the thin $Cu_{2-x}S$ absorber. Further degradation may be a result of the transformation to djurleite in the copper-depleted regions between the grid lines.

A third mode of degradation is the loss of copper by diffusion into the CdS layer. Significant diffusion is thought to occur during extended processing treatments at 150 to 250°C[13] but not at operating temperatures (<70°C).[44,50,51]

All three primary degradation modes involve the loss of copper from the $Cu_{2-x}S$ layer. Since this copper loss is manifested by a change in structure, the low chalcocite-to-djurleite transformtion has been the subject of some recent structural studies. The reflection electron diffraction experiments of Russell and Woods[52] confirmed that the ion exchange process converted the CdS surface layer to topotaxial low chalcocite and that the aging of these films in the laboratory ambient (2-1/2 years) resulted in mixed low

chalcocite-djurleite films. Echigoya and Edington[53] found that thin unsupported transmission electron microscope (TEM) specimens of low chalcocite rapidly degraded to djurleite in the laboratory ambient, but that some low chalcocite remained in aged films which were supported by CdS, even after 1400 hours. Sands et al.[54,55] applied the TEM technique to the study of low chalcocite-djurleite interfaces in $Cu_{2-x}S$ thin films. In these latter papers, the relationship between the low chalcocite and djurleite structure is discussed and a model for the transformation involving the ordering of copper vacancies is presented. This structural model will be discussed in more detail in Section 5.

2. CRYSTALLOGRAPHY AND PHASE RELATIONSHIPS IN THE $Cu_{2-x}S$/CdS SYSTEM

2.1 Cadmium Sulfide

Cadmium sulfide generally adopts the equilibrium wurtzite structure consisting of interpenetrating hexagonal-close-packed (h.c.p.) networks of Cd and S separated by ~0.375 $\vec{c}_o$ (Fig. 2.1). Depending on the growth technique, growth temperature, and level of mechanical damage, the sphalerite structure (interpenetrating face-centered-cubic (f.c.c.) networks of Cd and S) is sometimes formed.[56] However, CdS single crystals and the evaporated CdS films used for solar cells are entirely wurtzite (unless mechanically damaged).

The wurtzite structure (space group $P6_3mc$), being non-centrosymmetric, exhibits two basal faces. As discussed in Section 1.4.2, the Cd (0001) surface has dramatically different etching properties than the S($000\bar{1}$) surface.

2.2 The Cu-S Phase Diagram

The complex Cu-S phase diagram was first described in detail by Roseboom.[57] More recently, Potter[25] has refined the equilibrium phase diagram and has described the relationships of the various metastable phases to the equilibrium phases. The stable invariant points and the standard free energies of formation are listed in Tables 2.1 and 2.2, respectively. The phase diagram for Cu : S > 1.75 and 25°C < T < 150°C is presented in Fig. 2.2.

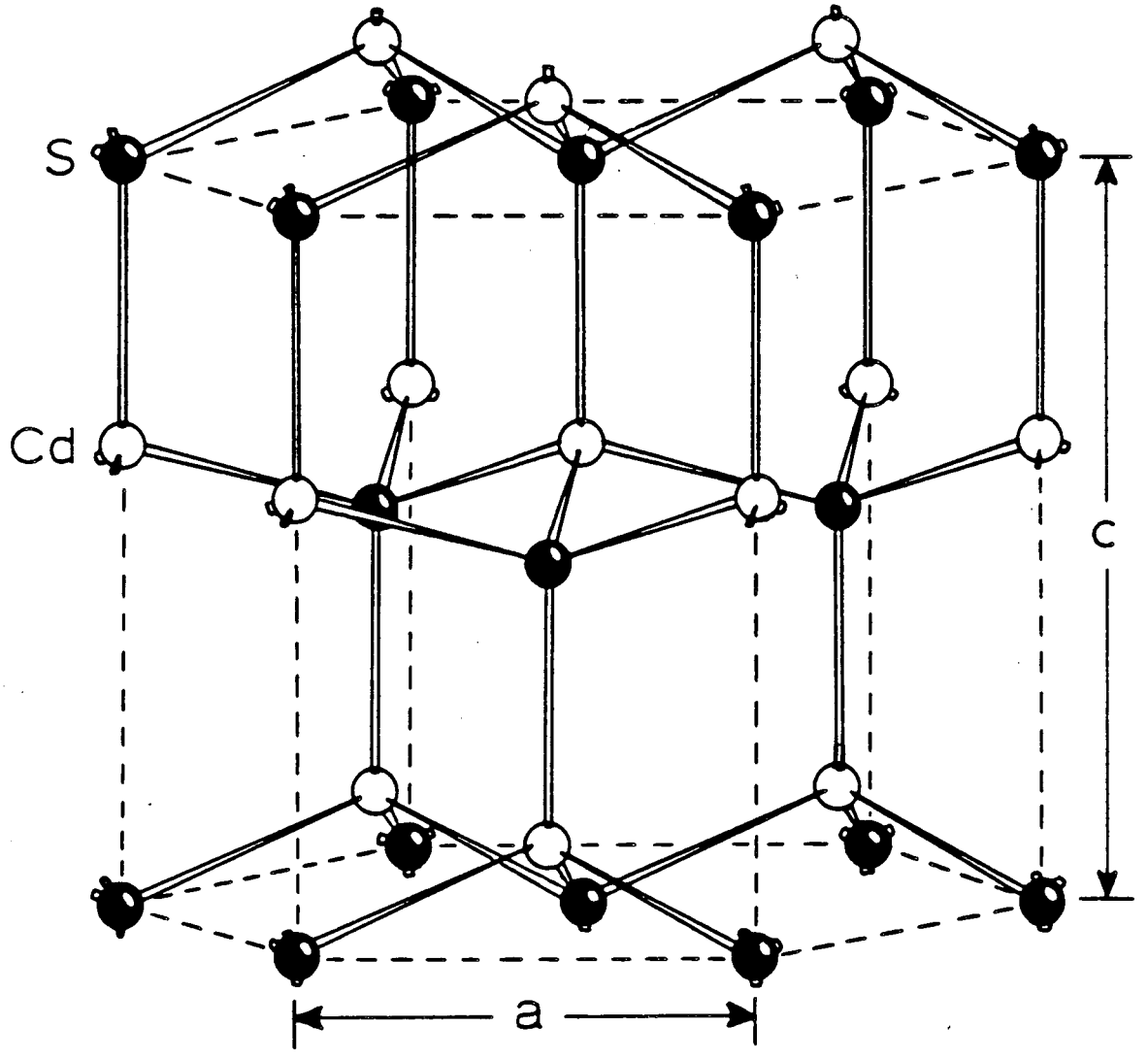

Fig. 2.1 Hexagonal wurtzite structure. XBL 843-1010

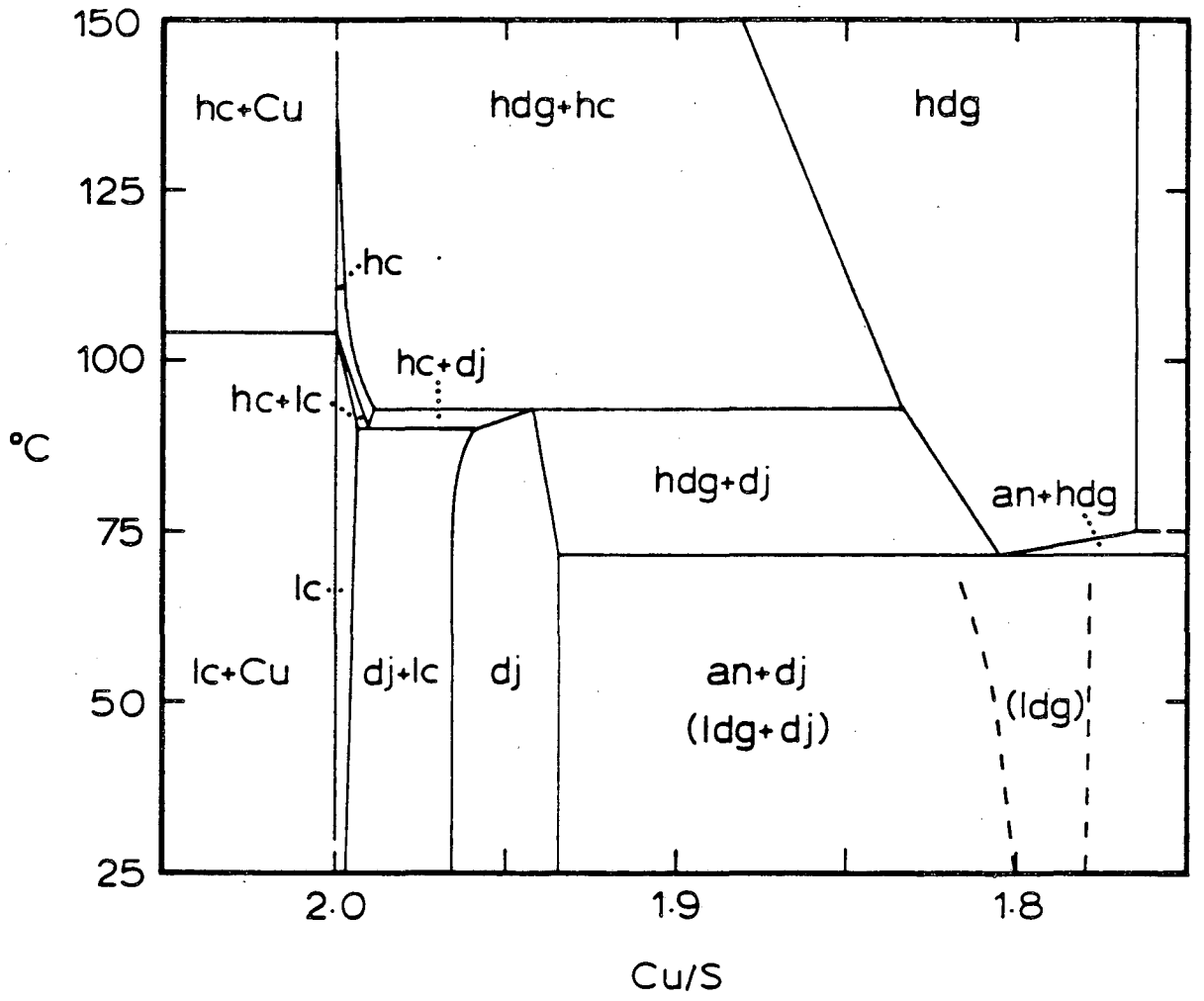

Fig. 2.2 Copper-sulfur phase diagram (after Potter[25]): lc, low chalcocite; dj, djurleite; an, anilite; hc, high chalcocite, hdg, high digenite; ldg, metastable low digenite.

Table 2.1 Stable invariant points in the Cu-S phase diagram (after Potter).[25]

high chalcocite (Cu/S = 2.000 ± 0.004) + Cu	
----------→ high digenite (2.000 ± 0.004) + Cu	T = 435 ± 8°C
low chalcocite (2.000 ± 0.002) + Cu	
----------→ high chalcocite (2.000 ± 0.002) + Cu	T = 103.5 ± 0.5°C
djurleite (1.942 ± 0.002)	
----------→ high digenite (1.834 ± 0.002) + high chalcocite (1.988 ± 0.005)	T = 93 ± 2°C
low chalcocite (1.993 ± 0.002)	
----------→ djurleite (1.960 ± 0.002) + high chalcocite (1.990 ± 0.005)	T = 90 ± 2°C
high digenite (1.805 ± 0.002)	
----------→ anilite (1.750 ± 0.003) + djurleite (1.934 ± 0.002)	T = 72 ± 3°C

Table 2.2 Standard free energies of formation of the copper-rich Cu-S phases (after Potter).[25]

high chalcocite (Cu: S = 2.000) : 376.65 to 708.15 K

$$\Delta G_F^\circ = -18{,}386 - 6.01\ T\ (K) - 0.000941T^2 \pm 300\ \text{cal/mole}$$

low chalcocite (2.000) : 273.15 to 376.65 K

$$\Delta G_F^\circ = -19{,}226 - 4.112T \pm 120\ \text{cal/mole}$$

djurleite (1.965) : 273.15 to 363.15 K

$$\Delta G_F^\circ = -19{,}178 - 3.53\ T \pm 100\ \text{cal/mole}$$

djurleite (1.934) : 273.15 to 345.15 K

$$\Delta G_F^\circ = -19{,}063 - 3.28\ T \pm 100\ \text{cal/mole}$$

low digenite (1.765) : 273.15 to 348.15 K

$$\Delta G_F^\circ = -18{,}366 - 1.17\ T \pm 100\ \text{cal/mole}$$

anilite (1.750) : 273.15 to 348.15 K

$$\Delta G_F^\circ = -18{,}169 - 2.02\ T \pm 70\ \text{cal/mole}$$

2.3 The Copper Sulfide Phases (Cu : S > 1.8): Structure, Composition, and Coordination

The structural properties of the relevant copper sulfide phases are summarized in Table 2.3. These phases can be classified into two types; phases based on distorted h.c.p. sulfur networks and phases based on distorted f.c.c. sulfur networks. Corresponding plane spacings in CdS and the $Cu_{2-x}S$ phases are compared in Table 2.4. This data will play an important role in the analysis of the TEM results.

The structure, composition, and bonding coordination of each of the copper-rich $Cu_{2-x}S$ phases are described below.

Table 2.3 Structural properties of the Cd-Cu-S phases

Phase	Sulfur Network	Space Group	Lattice Parameters [nm]	Cell content	references
CdS	h.c.p.	$P6_3mc$ (hexagonal)	a = 0.41368 (3) c = 0.67163 (2)	2 CdS	58
high chalcocite	h.c.p.	$P6_3/mmc$ (hexagonal)	a = 0.3961 c = 0.6722	$2Cu_2S$	59
low chalcocite	~h.c.p.	$P2_1/c$ (monoclinic)	a = 1.5246 (4) b = 1.1884 (2) c = 1.3494 (3) $\beta = 116.35\ (1)^\circ$	$48Cu_2S$	60-62
djurleite	~h.c.p.	$P2_1/n$ (monoclinic)	a = 2.6897 (6) b = 1.5745 (3) c = 1.3565 (3) $\beta = 90.13\ (3)^\circ$	8 $Cu_{31}S_{16}$ (128 $Cu_{1.938}S$)	61,62
high digenite	f.c.c.	Fm3m (cubic)	a = 0.556	$4Cu_{2-x}S$	63
tetragonal phase	~f.c.c.	$P4_32_12$ (tetragonal)	a = 0.4008 c = 1.1268	$4Cu_2S$	59,64
low digenite	~f.c.c.	pseudo-cubic	$2a_o$-$6a_o$ d_o = 0.554	20 $Cu_{1.8}S$ ($5a_o$)	65-67

Table 2.4 Comparison of plane spacings

Phase	Spacing [nm]	Percent misfit rel. to CdS	Spacing [nm]	Percent Misfit rel. to CdS
CdS	$d_{0\bar{1}10} = 0.3583$	----	$d_{0002} = 0.3358$	---
low chalcocite	$d_{\bar{4}00} = 0.3415$	(-4.7)	$d_{\bar{2}04} = 0.3374$	(+0.5)
	$d_{\bar{2}30} = 0.3427$	(-4.4)		
tetragonal phase	$2/3d_{\bar{1}0\bar{4}} = 0.3456$	(-3.5)	$d_{102} = 0.3268$	(-2.7)
	$1/3d_{\bar{1}3\bar{4}} = 0.3467$	(-3.2)		
djurleite	$d_{004} = 0.3391$	(-5.4)	$d_{800} = 0.3362$	(+0.1)
	$d_{042} = 0.3404$	(-5.0)		
low digenite ($6a_o$)	$d_{\bar{4}48} = 0.339$	(-5.4)	$d_{66\bar{6}} = 0.320$	(-4.7)

2.3.1 High Chalcocite

High chalcocite is the high-temperature parent phase of low chalcocite and djurleite. The copper ions in high chalcocite are distributed in a nearly fluid state among the triangular intersticies of the h.c.p. sulfur network.[68,69] As high chalcocite, Cu_2S, is cooled to below 103°C, the copper ions order to form the complicated superstructure of low chalcocite. For slightly copper-deficient compositions, super-cooling of high chalcocite results in the

metastable proto djurleite phase[25,70] (see Section 10.3). Protodjurleite then decomposes into the stable mixture of low chalcocite and djurleite.[65]

2.3.2 Low Chalcocite

The arrangement of copper ions in low chalcocite ($1.993 < Cu \div S < 2.000$) is extremely complex.[71] The monoclinic unit cell contains 24 distinct copper sites. As predicted by theory,[72] most of the copper ions are in nearly triangular coordination with sulfur. Evans[60,62] has determined the space group and lattice parameters of low chalcocite (Table 2.3). Fortunately, the monoclinic unit cell can be substituted with a pseudo-orthorhombic unit cell which is more easily related to the distorted h.c.p. sulfur network. A vector (u,v,w) in the monoclinic lattice can be expressed as a vector (u',v',w') in the psuedo-orthorhombic lattice by the transformation.

$$\begin{pmatrix} 0 & -1 & 0 \\ 1/2 & 0 & 0 \\ -1/2 & 0 & 1 \end{pmatrix} \begin{pmatrix} u \\ v \\ w \end{pmatrix} = \begin{pmatrix} u' \\ v' \\ w' \end{pmatrix}$$

The relationships between the monoclinic and pseudo-orthorhombic supercells and the high-temperature subcell are diagrammed in Fig. 2.3. These unit cells are further illustrated in the high-resolution micrographs of Figs. 2.4 and 2.5.

2.3.3 Djurleite

Djurleite, a phase closely related to low chalcocite, was first detected by Djurle.[59] Potter[25] determined the solid solution

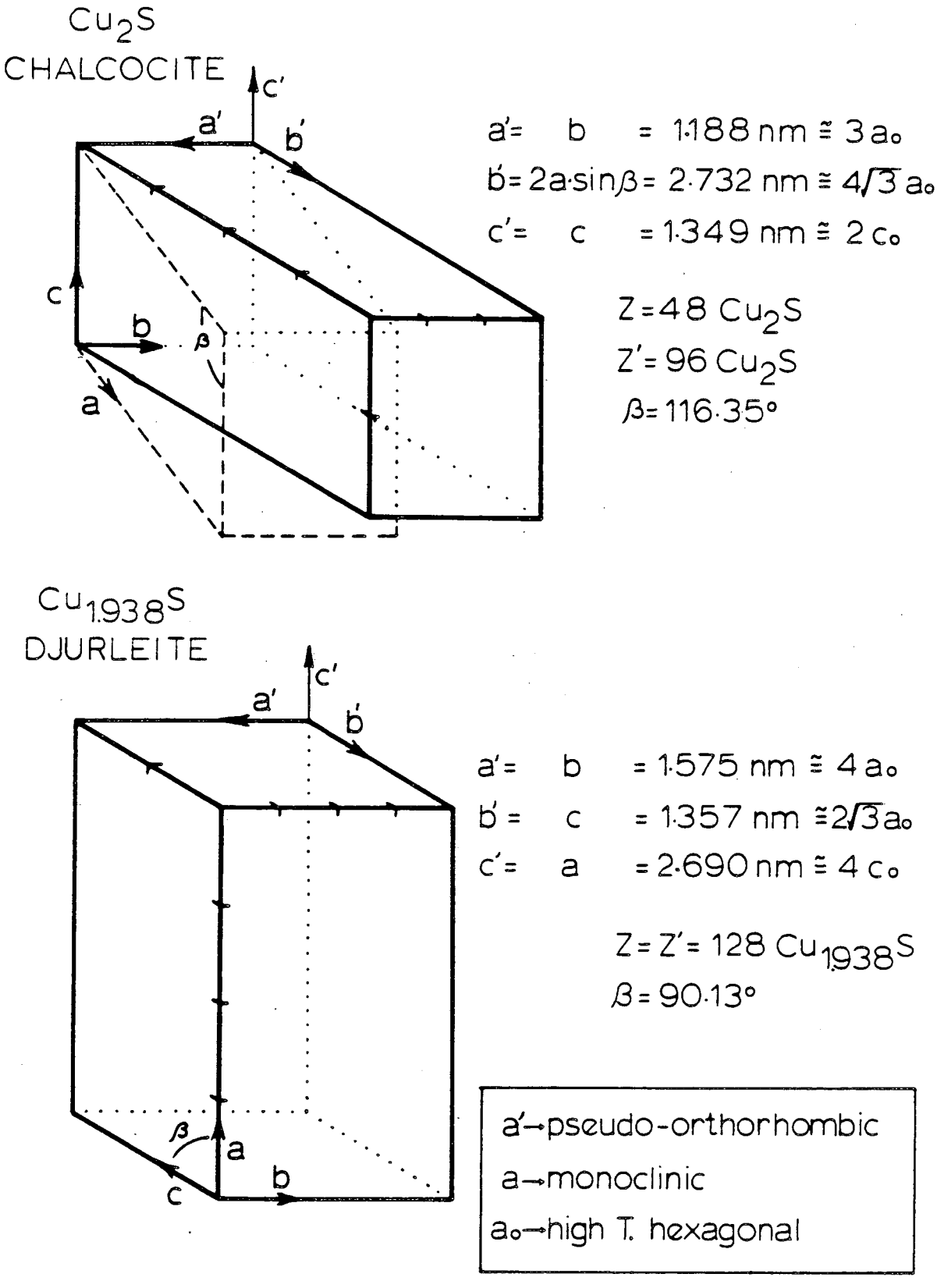

Fig. 2.3 Comparison of low chalcocite and djurleite unit cells.

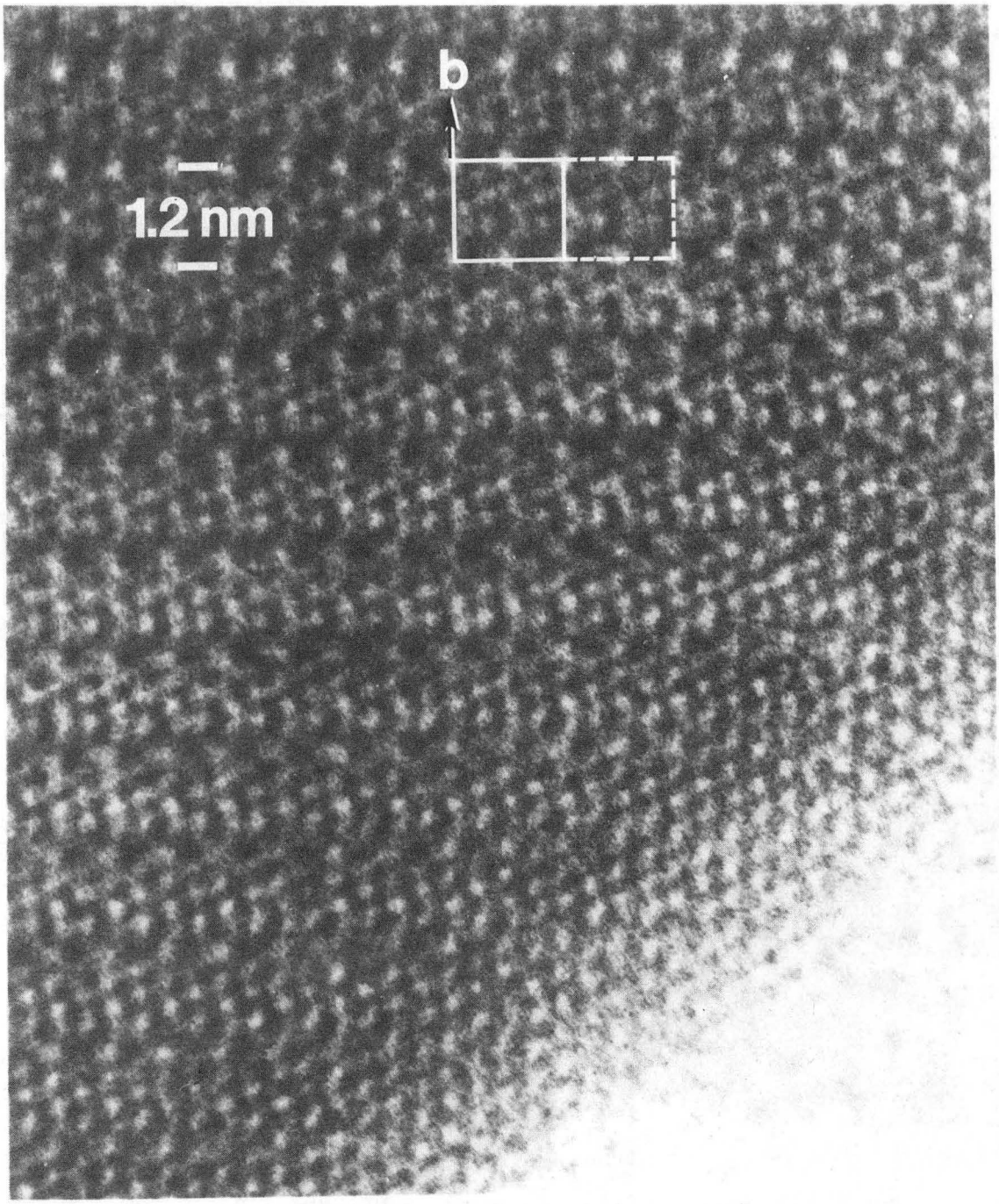

Fig. 2.4 High-resolution transmission electron microscope image of low chalcocite in [001] zone-axis orientation. Monoclinic (solid) and pseudo-orthothombic (dashed) unit cells are indicated. XBB 833-2567B

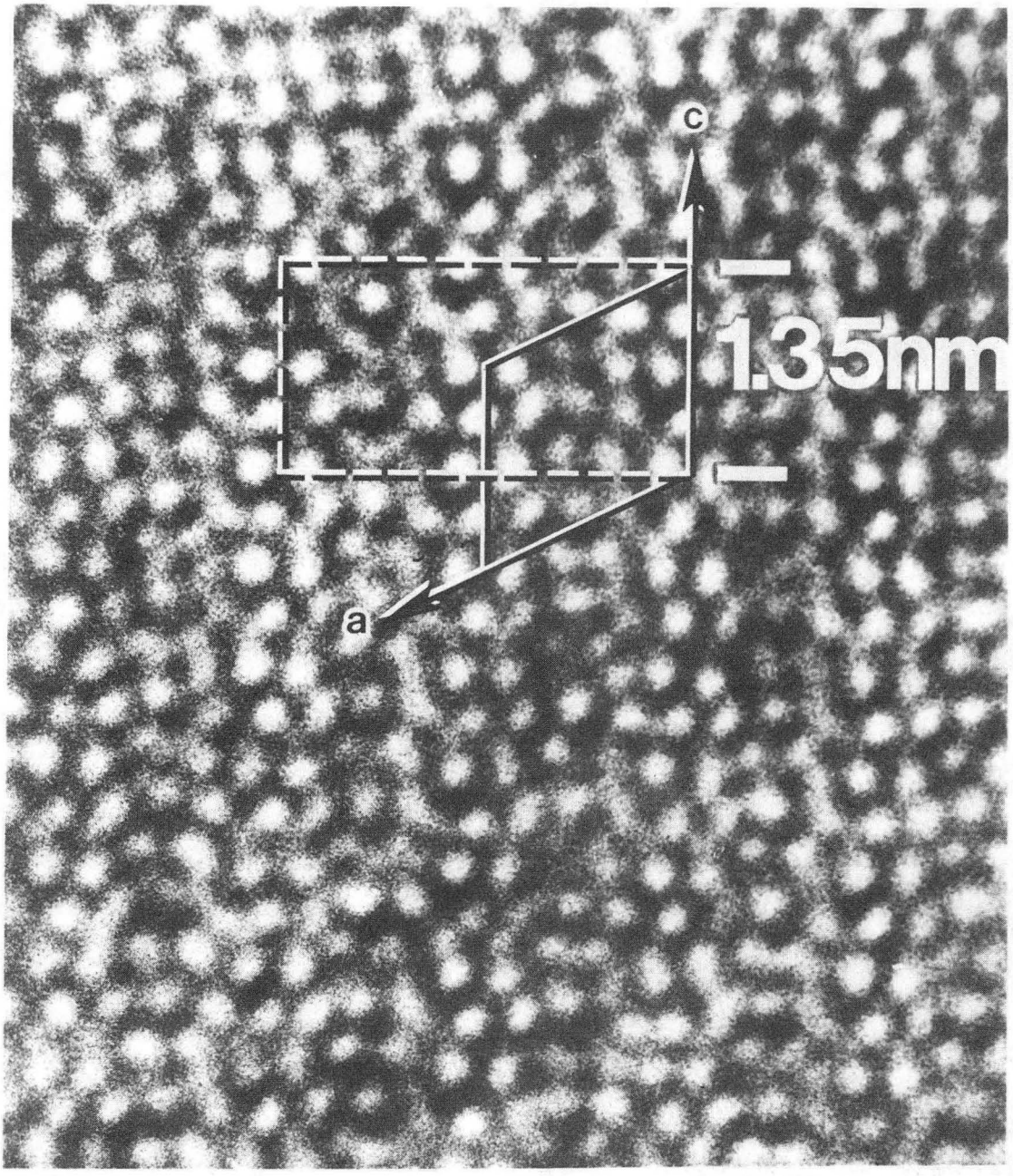

Fig. 2.5 High-resolution transmission electron microscope image of low chalcocite in [0$\bar{1}$0] zone-axis orientation. Monoclinic (solid) and pseudo-orthorhombic (dashed) unit cells are indicated. XBB 843-1726

range of djurleite to be $1.934 < Cu : S < 1.965$. The crystal structure and space group of djurleite ($Cu_{1.938}S$) was established by Evans[61,62] (Table 2.3). Evans found that most of the copper ions are in triangular coordination with sulfur. However, a significant fraction (9/62) are in tetrahedral coordination with sulfur. This trend toward tetrahedral coordination and reduced covalent character[72] persists as the Cu : S ratio is reduced.[71]

The compositional homogeneity range as determined by Potter corresponds approximately to the composition range $Cu_{62}S_{32}$ to $Cu_{63}S_{32}$ ($1.938 < Cu : S < 1.969$). However, Evans[71] was unable to determine the location of the extra copper ion (per asymmetric unit) in copper-rich djurleite. This subject is discussed in more detail in Section 5.4.1.

In a similar manner to the treatment of the low chalcocite unit cell, the monoclinic unit cell of djurleite can be related to a pseudo-orthorhombic unit cell. A vector (u,v,w) in the monoclinic lattice can be expressed as a vector (u',v',w') in the pseudo-orthorhombic lattice by the transformation,

$$\begin{pmatrix} 0 & -1 & 0 \\ 0 & 0 & -1 \\ 1 & 0 & 0 \end{pmatrix} \begin{pmatrix} u \\ v \\ w \end{pmatrix} = \begin{pmatrix} u' \\ v' \\ w' \end{pmatrix}$$

The relationships between the monoclinic and pseudo-orthorhombic supercells and the high temperature subcell are illustrated in Fig. 2.3.

2.3.4 High Digenite

The high digenite phase is based upon an f.c.c. sulfur network.[63] At high temperatures (>72°C), the copper ions are disordered among the intersticies. At low temperatures, the copper ions order to form the superstructure of low digenite or the equilibrium anilite phase.[65]

2.3.5 Low Digenite

Low digenite ($6a_o$) is a metastable phase[73] with a pseudo-cubic unit cell of lattice parameter $6a_o$, where a_o is the lattice parameter of the high-temperature subcell. The high digenite-to-low digenite transformation is thought to involve the spinodal clustering of vacant tetrahedral sites and the subsequent local ordering of these vacancy clusters.[65] The development of the low digenite superstructures has been thoroughly investigated with transmission electron diffraction by van Dyck et al.[74,75]

2.3.6 The Tetragonal Phase

The tetragonal phase, a high-pressure polymorph of chalcocite,[76] was first described by Djurle.[59] Pressures greater than ~2 kilobars are required to transform low chalcocite into the tetragonal phase,[76] which may explain, in part, the formation of the tetragonal phase during grinding of low chalcocite at room temperature.[77] Potter[25] found that the tetragonal phase formed in electrodes with bulk composition $1.85 < Cu : S < 1.99$ in the temperature range 115 to 145°C. Complete inversion to the stable high chalcocite phase required seventeen days at 118°C. The sluggish nature of this

transformation is due to the involvement of the sulfur network. The f.c.c. sulfur network[64] of the tetragonal phase can be converted to the h.c.p. sulfur network of high chalcocite by the passage of Shockley partial dislocations on every other close-packed plane. Since the rearrangement of the highly mobile[78] copper ions is rapid, the passage of Shockley partials (or possibly the nucleation of Shockley partials) is the rate limiting step.

Janosi[64] has described the structure of the tetragonal phase. As mentioned by Evans,[71] the structure is relatively simple, with only triangular coordination of copper with sulfur. This structure is illustrated in Fig. 2.6. A vector (u,v,w) in the tetragonal lattice can be expressed as a vector (u',v',w') in the face-centered-cubic sublattice by the transformation,

$$\begin{pmatrix} 1/2 & -1/2 & 0 \\ 1/2 & 1/2 & 0 \\ 0 & 0 & 2 \end{pmatrix} \begin{pmatrix} u \\ v \\ w \end{pmatrix} = \begin{pmatrix} u' \\ v' \\ w' \end{pmatrix}.$$

Previous to this study, detection of the tetragonal phase in copper sulfide layers formed by the aqueous ion-exchange of CdS had not been reported. However, the tetragonal phase has been detected in vacuum-evaporated films[79] and in films formed by sulphurization of copper.[80]

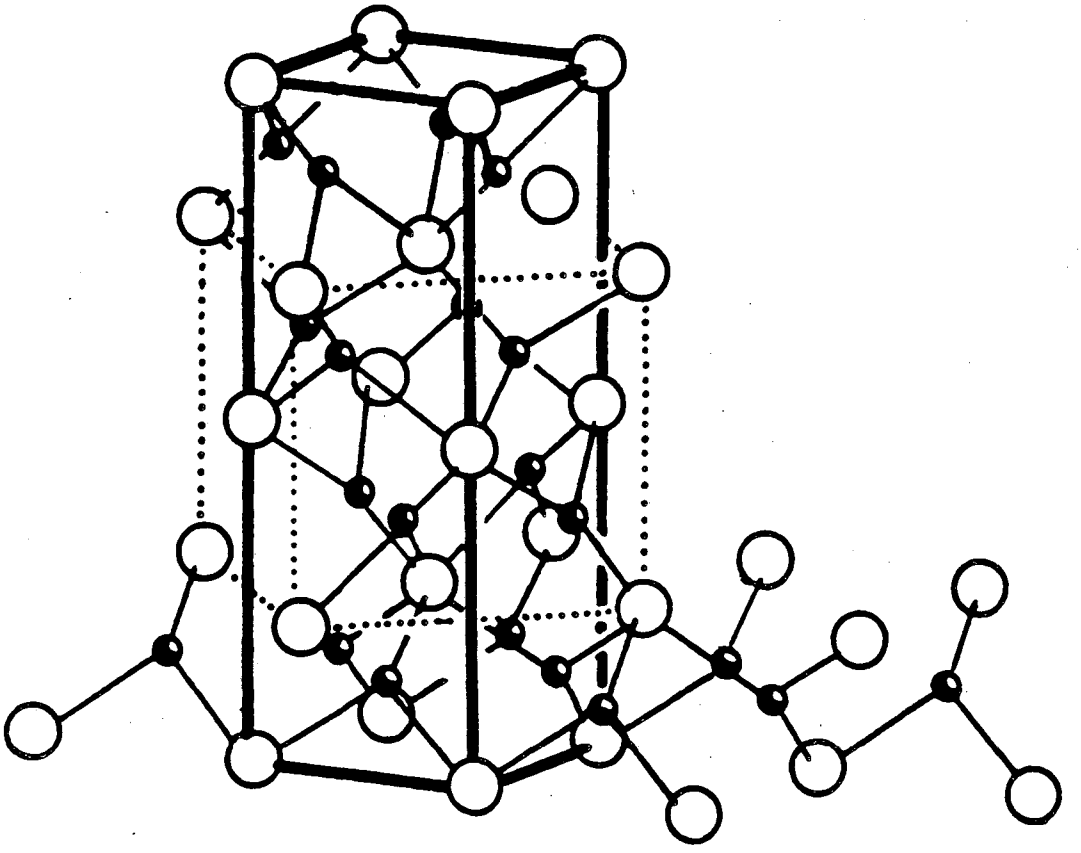

Fig. 2.6 Structure of tetragonal phase (after Evans[71]). Open circles are sulfur. Closed circles are copper. Dashed lines indicate ~f.c.c. sulfur subcell. XBL 843-1009

3. EXPERIMENTAL METHODS

3.1 Heterojunction Fabrication

In order to avoid the complicating effects of grain boundaries and high dopant levels, experiments were performed with undoped single-crystal CdS (Eagle-Picher). CdS boules approximately 2 cm in diameter were oriented with the Laue back-reflection x-ray technique and then cut into 2 mm thick {0001} slices. These slices were mechanically polished on both faces. The final polish was achieved with 1 μm diamond paste. The CdS slices were then etched in fresh 37 percent HCl at room temperature for 30-60 seconds. The etching treatment served three purposes. First, the mechanically-damaged surface layer which has been shown to consist of polycrystalline sphalerite CdS[1] was removed. Secondly, the HCl etch provided a textured surface for enhanced light trapping. Finally, the radically different etching behavior of the two basal surfaces provided a means for surface identification.

The copper sulfide layer was formed immediately following the etching treatment. All heterojunctions used for this study were prepared by the "wet process" described in Section 1.4.1. The exchange bath consisted of 6 g/l Cu_2Cl_2 (99.999%) and 2 g/l NaCl reagent[22] (pH unadjusted). The details of the conversion process and the subsequent modifications of this technique are described below.

The ion exchange bath was prepared by boiling 250 ml of distilled H_2O for approximately 15 minutes in a covered and vented pyrex flask. A thermometer and a gas bubbler were inserted through rubber

stoppers in two necks of the flask. Bubbled argon gas served to help purge the bath of dissolved oxygen[22] and to agitate the solution during the conversion process. Following the purging treatment, the Cu_2Cl_2 and NaCl were added. After the solution temperature was stabiliz ed at the desired reaction temperature (usually 99°C), the specimen, which was mounted with wax on a glass slide, was lowered into the solution by means of a glass rod attached to the slide. The specimen remained in the conversion solution for from 5 to 12 seconds. To terminate the reaction and to remove the unreacted Cu_2Cl_2, the specimen was rinsed in room temperature distilled water. Excess water was drawn off with filter paper and the specimen was allowed to dry in air.

The conversion technique as described above was found to yield phase distributions of copper sulfide which were not reproducible. Transmission electron microscopy and diffraction of separated films (described in Section 3.2.1) revealed the presence of the copper-deficient phases, djurleite and low digenite, in many samples. These undesirable copper sulfide phases were also observed when the conversion bath was intentionally held at temperatures below ~90°C (see Section 5.1). Therefore, the copper deficiency was thought to result from a depressed reaction temperature due to the thermal inertia of the glass specimen mount. In an effort to minimize this effect, the conversion technique was altered in the following three ways:

i) The specimen was held in distilled water at the desired conversion temperature for 5 minutes immediately prior to conversion.

ii) The specimen was lowered into the conversion bath with stainless steel tweezers. The portion of the specimen held by the tweezers was discarded. This technique had the advantage that both faces of the specimen could be converted simultaneously.

iii) Mechanical agitation was substituted for argon gas agitation during conversion, thereby eliminating any undesirable thermal effects due to the argon gas bubbles.

This revised conversion technique was found to be simpler and more reproducible than the previous technique. Transmission electron microscope studies (Section 4) showed that the specimens prepared by the revised technique were entirely low chalcocite and the tetragonal phase with no trace of the copper-deficient phases, djurleite and low digenite.

3.2 Specimen Preparation for Transmission Electron Microscopy

3.2.1 Plan-View Separated Copper Sulfide Films

Although the HCl etchant readily attacks the CdS, the same etchant has no effect on copper sulfide. Shirland[81] used this selective-etching property to produce free-standing copper sulfide films for scanning electron microscope (SEM) examination. This specimen preparation technique has been refined and extended to produce TEM specimens for the present study.

Immediately following heterojunction formation the converted CdS was placed in a beaker of room temperature 37 percent HCl. The etchant attacked the CdS through cracks in the copper sulfide film. Within ~60 seconds, the interfacial layer of CdS was dissolved. The

copper sulfide film could then be lifted by surface tension onto the surface of a distilled water bath. Copper sulfide films which had been grown for 5 seconds or less were difficult to remove intact, however, films grown for 10 seconds or more were easily removed. Films as large as 5 mm x 5 mm could be separated in one piece.

Floating films were gently lifted from the surface with folding TEM grids (2.3 or 3 mm diameter) bent to an angle of ~120°C. Water was drawn off the specimen by touching the grid to filter paper. Tweezers were then used to fold the upper grid onto the specimen-laden lower grid. This rapid and dependable specimen preparation technique permitted observation of specimens in the TEM immediately following copper sulfide film formation. In addition, virtually all of a given film could be examined by preparing several specimens.

3.2.2 Cross-Section Specimens

Cross-section $Cu_{2-x}S$/CdS specimens were found to be extremely difficult to prepare. However, the potential wealth of information available in cross-sectional views justified the effort. Although many techniques were tried, only the most successful specimen preparation technique is described below and illustrated in Figure 3.1.

After conversion to copper sulfide the etch-pit geometry of the (0001) face was examined to determine the orientation of the $\{\bar{2}110\}$ cleavage planes. Slight pressure of a razor blade was found to produce macroscopically flat cleavage faces in thin specimens (<1 mm). Two thin cleaved strips were bonded sulfur face-to-cadmium face with epoxy. In this manner, both the sulfur and cadmium faces

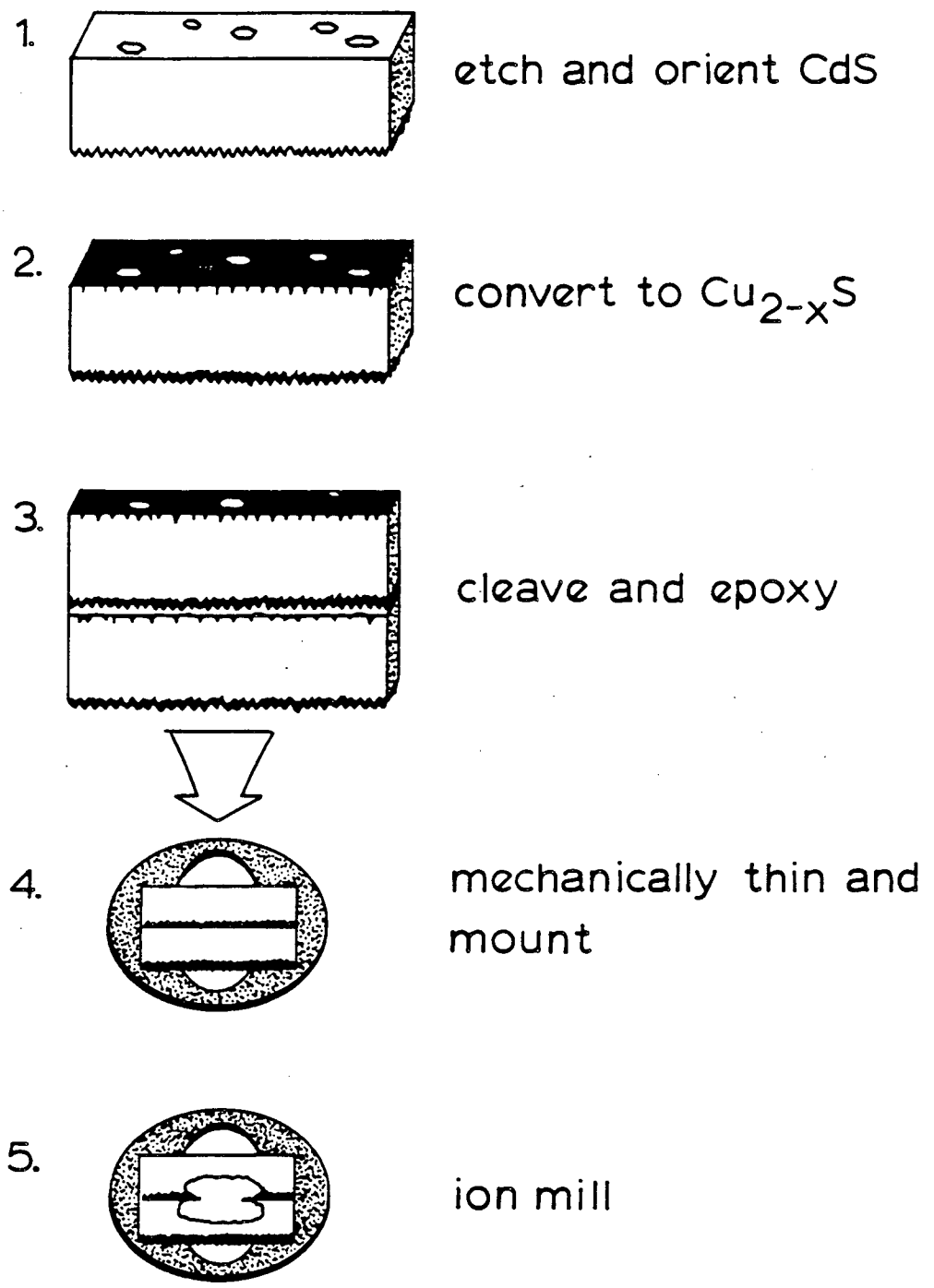

Fig. 3.1 Preparation of $Cu_{2-x}S$/CdS cross-section specimens.
XBL 843-1008

from the same CdS wafer were accessible in a single cross-section specimen. After a minimum setting period of 24 hours, the specimen was mounted with wax (~80°C melting temperature) onto a glass polishing disk ($Cu_{2-x}S$/CdS interfaces perpendicular to the plane of the disk). The specimen was then polished mechanically on a rotating wheel with 600 grit paper. The final polish was accomplished with 6 μm and then 1 μm diamond paste. This polishing procedure was repeated on the other side of the specimen until a final thickness of between 50 and 100 μm was achieved. The specimen was separated from the glass disk by dissolving the wax in a warm (60–80°C) beaker of dimethyl formamide (performed in a fume hood, avoiding any contact with the solvent or its vapors). The solvent was poured into a second beaker, leaving the specimen in the first beaker. A stream of acetone was used to gently wash the specimen onto filter paper. The specimen was then glued to a copper ring (2.3 or 3 mm diameter) for support and ease of handling. The final thinning was accomplished with argon ion-beam milling at 15° specimen tilt, 4kV gun voltage, and ~20 μA specimen current. The rotating specimen stage of the Gatan ion mill was cooled with liquid nitrogen to avoid beam heating effects. At the first appearance of a hole (after 4 to 10 hours of milling) the specimen was removed and examined with an optical microscope. Unfortunately, the first hole was usually formed in the CdS adjacent to the interface due to the faster milling rate of CdS. The yield for high resolution specimens prepared by this technique was approximately

30 percent. Significantly higher yield may be possible by dimpling the interfacial region of the specimen to a thickness of 10 to 30 μm before ion milling.

3.3 Phase Identification by Lattice Imaging

In order to study the $Cu_{2-x}S$/CdS interface morphology and the distribution of copper sulfide phases in the absorber layer, a technique with high spatial resolution is required. Although x-ray diffraction can provide phase identification, neither technique can give real-space information at the desired level of resolution ($\leq$1 nm). A third technique, dark field electron microscopy, is useful if the density of spots in reciprocal space is low. However, the interfacial areas of interest in this study often contained three phases. In addition, each copper sulfide phase occasionally exhibited two or more variants in close proximity. Therefore, in the worst case, five or six complicated diffraction patterns overlapped making spot selection for dark-field microscopy (see Section 3.3.1) extremely difficult. The only technique which provides both phase identificaton and an accurate map of the phase distribution is phase-contrast transmission electron microscopy, also known as lattice (or in special cases, structure) imaging. This technique is especially well-suited to the study of large unit cell materials such as the copper sulfide phases.

Qualitative descriptions of electron diffraction and phase contrast imaging are presented below. Thorough and quantitative

treatments can be found in the books by Hirsch et al.,[82] Thomas and Goringe,[83] Spence,[84] and the monograph by Edington.[85] The subject of phase-contrast electron microscopy is reviewed by Gronsky.[86]

3.3.1 Electron Diffraction in the Transmission Electron Microscope

A monochromatic beam of high energy ($\geq$100 keV) electrons in the evacuated column of the TEM can be used to probe the structure of solids at the atomic level. In a conventional TEM, a fine beam of electrons emitted from a tungsten or LaB_6 filament is manipulated by a series of apertures and magnetic lenses in a manner analogous to the manipulation of light by apertures and glass lenses in a light-optical microscope. The object of interest, generally a thin crystal, is placed in the path of the collimated and focused electron beam. Since the wavelength of the electrons (0.037Å at 100 keV) is considerably smaller than the range of interatomic distances, the electron beam experiences the periodic potential of the specimen. As in the simple Bragg description of diffraction, the scattering of the electron beam by the periodic potential is significant (constructive interference) only when the path difference between waves scattered by adjacent parallel atomic planes of spacing d is an integral multiple of the electron wavelength. This constructive interference effect is known as the Bragg law, $\lambda = 2d \sin \theta$, where d is the separation of the scattering planes and θ is the angle between the scattering planes and the incident beam (Fig. 3.2).

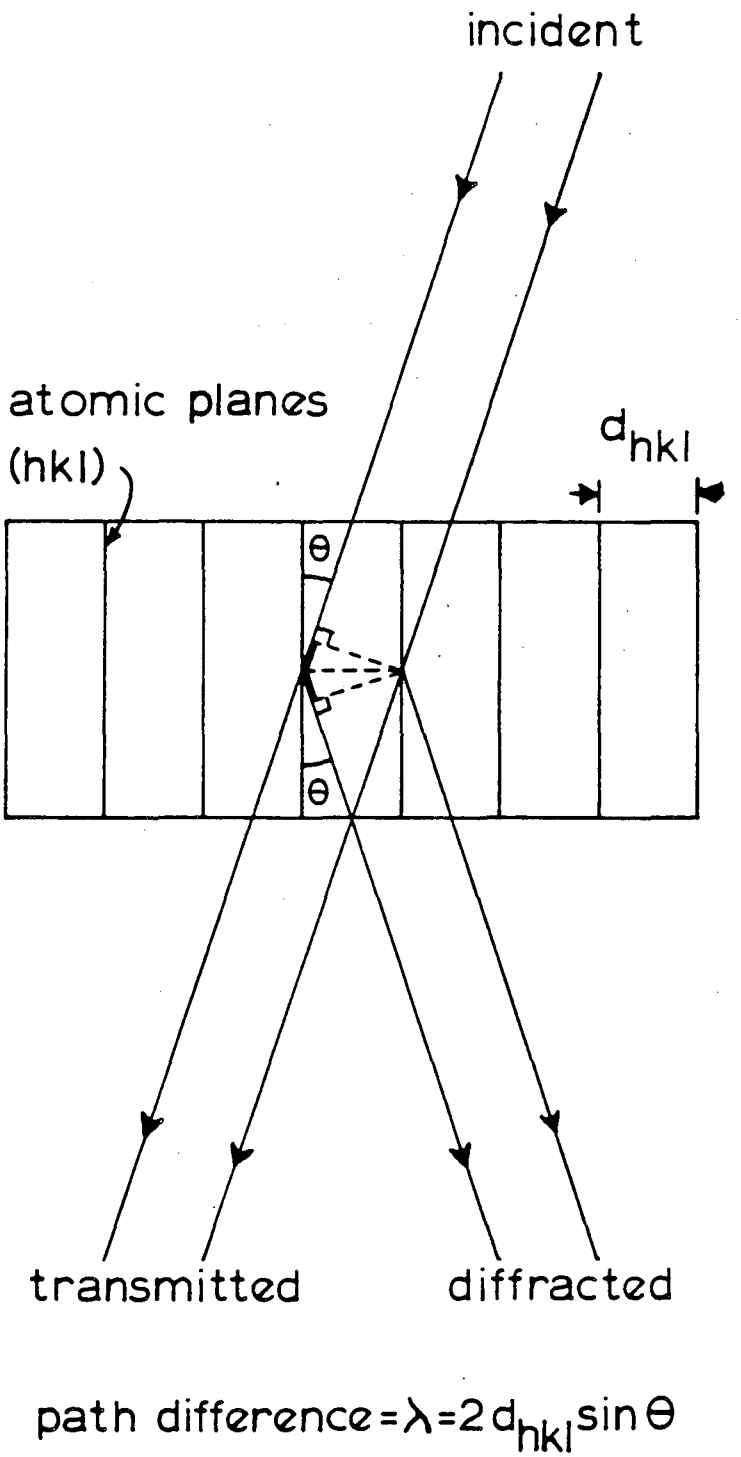

Fig. 3.2 Bragg law of diffraction. Path difference is indicated by heavy line. XBL 843-1007

For an electron beam at 100 keV and a plane spacing of 2Å, the reflecting angle, θ, is less than a degree. Therefore, all sets of reflecting planes with normals approximately perpendicular to the incident direction will produce diffracted beams. If this "diffraction pattern" is recorded on photographic emulsion, the distance between the diffracted and transmitted (forward-scattered) spots will be approximately proportional to 1/d. In addition, the vectors connecting the transmitted and diffracted spots will lie in the planes which are perpendicular to the corresponding reflecting planes and which contain the incident direction.

Noting the reciprocal dependence of spot position on plane spacing, one can imagine that a reciprocal lattice construction might be useful. To construct the reciprocal lattice of a given crystalline specimen, a reciprocal lattice vector, $\vec{g}_{hkl}$, is associated with each set of planes, (hkl). The length of the vector $\vec{g}_{hkl}$ is given by $|\vec{g}_{hkl}| = 1/d_{hkl}$ and the vector $\vec{g}_{hkl}$ is perpendicular to the set of planes (hkl). Except for a constant factor of 2π, this space is identical to the "k-space" used by physicists.

The reciprocal lattice construction allows a more sophisticated but essentially equivalent description of diffraction than the Bragg law as described above. Elementary elastic scattering theory[87] shows that the three-dimensional equivalent of Bragg's law is given by

$$|\vec{k}/2\pi + \vec{g}| = |\vec{k}/2\pi|$$

where $\vec{k}$ is the incident wave vector ($|\vec{k}| = 2\pi/\lambda$). In other words, constructive interference occurs if the diffracted wave vector differs from the incident wavevector by $2\pi\vec{g}$ and if the diffracted and incident wave vectors are equal in magnitude (as required for elastic scattering). Geometrically, this equation describes a sphere (called the "Ewald sphere") of radius $|\vec{k}/2\pi| = 1/\lambda$ passing through the origin of reciprocal space (see Fig. 3.3).

the vector extending from the center of the Ewald sphere to the origin of reciprocal space is the incident wave vector divided by 2π. Those reciprocal lattice points which lie on this sphere represent the possible diffracted beams of non-zero amplitude. Actually, the reciprocal lattice "points" have finite extent for diffracting objects with finite dimensions so that the center of the reciprocal lattice "point" need not lie exactly on the sphere in order to contribute non-zero amplitude.

Since the radius of the Ewald sphere is $1/\lambda$, the small wavelength of TEM electrons results in a large Ewald sphere. If oriented tangent to a low index reciprocal lattice plane, the Ewald sphere's intersection with the reciprocal lattice is a nearly planar section of the reciprocal lattice. This characteristic two-dimensional axial diffraction pattern can be viewed in the TEM with a properly oriented specimen by imaging the back focal plane of the objective lens.

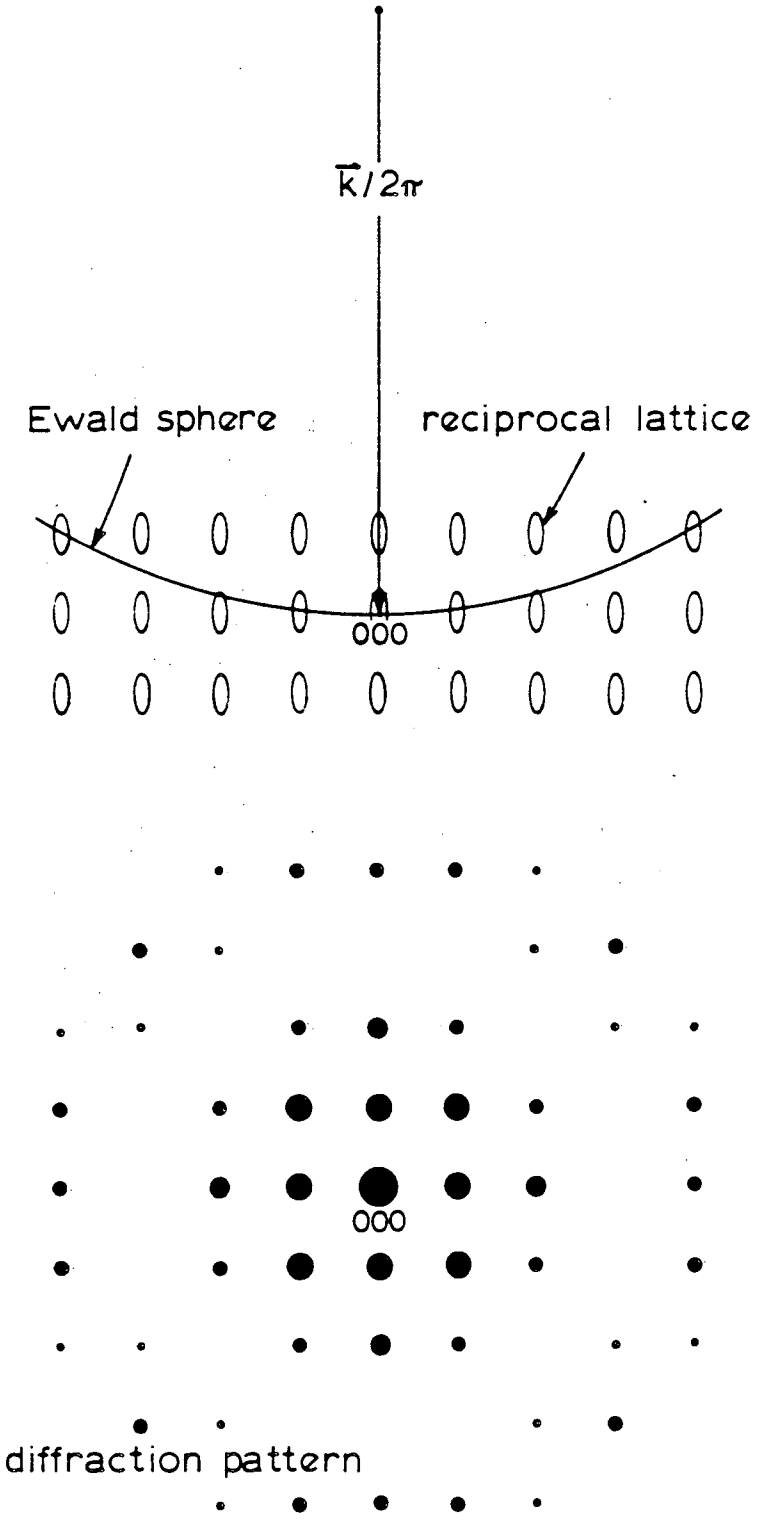

Fig. 3.3 Ewald sphere construction. Corresponding electron diffraction pattern is also shown. XBL 843-1020

Each diffracted beam contains a "map" of the specimen. For example, the 200 beam from a cubic crystal contains information from all areas of the specimen which scatter incident electrons into the 200 beam. With the aid of objective apertures in the back focal plane of the objective lens, the microscopist has the freedom to exclude certain information (i.e., certain diffracted beams). The remaining beams can then be recombined to form an image. If only a diffracted beam is allowed to pass through the magnification system of the microscope, the image will contain only information from regions of the specimen which scattered into that particular diffracted beam. The resulting image, recorded photographically, is called a dark-field image. Similarly, the microscopist may choose to accept only the transmitted beam. In this case, a bright-field image is recorded. These single beam images are known as amplitude-contrast images since the amplitude, and not the phase, determines image intensity. A third option is to allow more than one diffracted beam to recombine and form an image. Since each beam contains both phase and amplitude information, the diffracted beams can interfere to produce a phase-contrast image. Phase-contrast imaging is the subject of the following section.

3.3.2 Phase-Contrast Imaging

If the relative phases of the various diffracted beams were undistorted, the number of beams which could be recombined with full information transfer would be limited only by the curvature of the Ewald sphere. In reality, complete reconstruction for thin specimens

which are weak-phase objects (phase changes due to the specimen are much less than $\pi/2$) is limited by lens aberrations and microscope instabilities. The most serious limitation is imposed by the spherical aberration of the objective lens. The effect of phase distortion due to spherical aberration can be modeled as the product of a phase factor and the electron wave function in the back focal plane. This "contrast transfer function" (CTF) can be written as:[88]

$$\exp[i\chi] = \exp\left\{i\,\frac{\pi}{\lambda}\left(\frac{C_s\alpha^4}{2} + \Delta z\,\alpha^2\right)\right\}$$

where $\alpha = |\vec{g}|\,\lambda$ is the angle between the diffracted beam and the forward-scattered beam, C_s is the spherical aberration coefficient, and Δz is the defect of focus. It is clear from the dependence of the CTF on α that the phase distortion due to spherical aberration increases rapidly as g moves away from the optic axis. Scherzer[89] noted that this effect can be minimized by operating in an underfocused condition with

$$\Delta z_{sch} \cong -\,1.2\,(C_s\lambda)^{1/2} \quad .$$

Nevertheless, the spherical aberration places a severe limitation on the attainable point-to-point resolution. At Scherzer defocus the spherical aberration limits the point-to-point resolution to

$$d_{sch} \cong 0.7\,C_s{}^{1/4}\lambda^{3/4} \quad .$$

For example, at 100 keV with C_s = 1.5 mm, d_{sch} = 3.7Å. Thus, beams corresponding to reciprocal lattice vectors with magnitudes greater than $1/3.7Å^{-1}$ will contribute only to the backround intensity in the image. The microscopist can exclude these beams by choosing a suitable objective aperture, thereby improving image contrast. The microscopist may also decide to eliminate beams which do contribute faithfully to the phase-contrast image. This is often the case when only superstructural information is required. In summary, the best choice for the objective aperture is generally the smallest aperture that transmits the required level of information. Extraneous detail or background noise is to be avoided.

The process of recording a high-resolution micrograph involves many steps in addition to objective aperture selection. First, the illumination condition must be optimized. Generally, the filament is operated in an undersaturated condition for maximum coherence. A condenser aperture is inserted for the optimum tradeoff between brightness (exposure time) and beam coherence. Following careful alignment of the imaging system, the specimen must be oriented to produce the highest symmetry in the diffraction pattern (for axial imaging) corresponding to the chosen zone axis.

Perhaps the most critical step is the adjustment of objective astigmatism. Astigmatism is corrected (with objective aperture in place) by application of a small corrective magnetic field. At low magnification (~80 kX), the stigmator coils are adjusted to give a Fresnel fringe of even width around a hole or protrusion. The next

level of astigmatism correction requires observation of amorphous material (usually the contamination layer at the specimen edge is chosen) at high magnification (400kX and above). The stigmators and objective lens current (focus) are adjusted to obtain an image with minimum contrast and maximum definition (theoretically, at $\Delta z_{mc} = -0.44\ (C_s\lambda)^{1/2}$). At this stigmator setting, the amorphous material should show fine-grain non-directional contrast as the focus is taken above and below the minimum contrast condition. A thru-focal series of images, starting in an over focused condition and proceeding incrementally through minimum contrast and beyond Scherzer defocus, is taken of the desired specimen area. Note that the optimum magnification (with respect to exposure time) is generally between 200 kX and 400 kX. Therefore, either the microscope must be adjusted so that the astigmatism correction is preserved at different magnifications or the astigmatism correction must be fine-tuned at the final magnification.

It is important to include a portion of the amorphous contamination layer in each image. Information about defocus, astigmation and specimen drift can be extracted from this portion of the developed negative by optical diffraction on a laser bench.[90] This information is required for meaningful comparisons with computer-simulated images.

Microscopes used for this study were the Siemens 102 and the JEOL-JEM 200-CX. The ±45° specimen tilt, the low spherical aberration coefficient (~1.2 mm) and the variable specimen height of the Siemens

102 (100 keV) made this microscope suitable for both low magnification work and superstructure imaging (i.e., phase-contrast imaging with the transmitted beam and superlattice reflections only).

When information from the sublattice was required, the JEM 200-CX was employed. Operated at 200 keV with a LaB_6 filament, this microscope ($C_s \cong 1.2$ mm, $\Delta z_{mc} \cong -240$Å, $\Delta z_{sch} \cong -660$Å) easily provided the necessary 3.4Å point-to-point resolution.

4. STRUCTURE OF THE AS-PREPARED Cu_2S/CdS HETEROJUNCTION

4.1 Experimental Results

4.1.1 Surface Morphology of Etched Cadmium Sulfide.

As discussed in Section 2.1, wurtzite CdS is non-centrosymmetric and exhibits two basal planes with different properties. The etched (0001) surface (Cadmium face) was found to consist primarily of basal facets. In crystals with nominally off-basal surface orientations, the surface was composed of ledges and basal terraces. Etch pits on the cadmium face were found to be hexagonal with terraced walls. Electron diffraction of copper sulfide replicas (see Section 4.1.4) showed that the etch pit walls were $\{1\bar{1}0\ell\}$-type surfaces. These surfaces features are illustrated in the SEM micrograph of Fig. 4.1.

The etched sulfur face was found to display an entirely different surface morphology. Scanning electron microscopy revealed pyramidal hillocks with dimensions on the order of several microns (Fig. 4.2). Electron diffraction of copper sulfide replicas (see Section 4.1.5) showed that the hillock facets were planes of the type $\{\bar{2}11\bar{\ell}\}$ corresponding to convex[37] etching. Cross-sectional SEM and TEM measurements gave $\ell \cong 2$. Slight concave etching was indicated by the broken ridges on the hillocks.[37] The size and shape of these hillocks explains the matte appearance of the etched sulfur face when examined with the light-optical microscope.

Etching studies were performed to determine the effect of etching time on hillock size and shape. Figure 4.3 shows that the hillock dimensions were of the order of 1 μm after 2 seconds in fresh

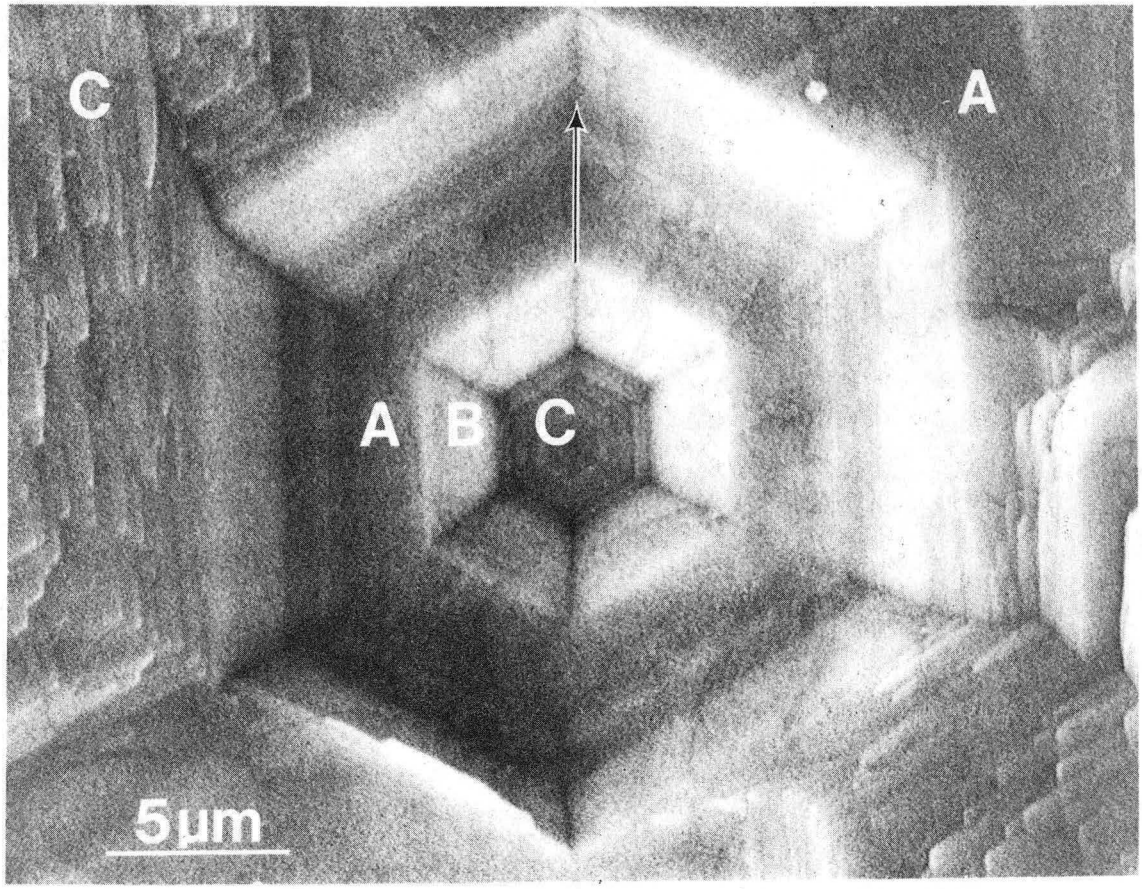

Fig. 4.1 SEM image of etched Cd face of CdS single crystal. "A" is basal facet, "B" is terraced etch pit wall, "C" is terraced off-basal surface. Arrow indicates $\langle\bar{2}110\rangle$ direction. XBB 839-8240.

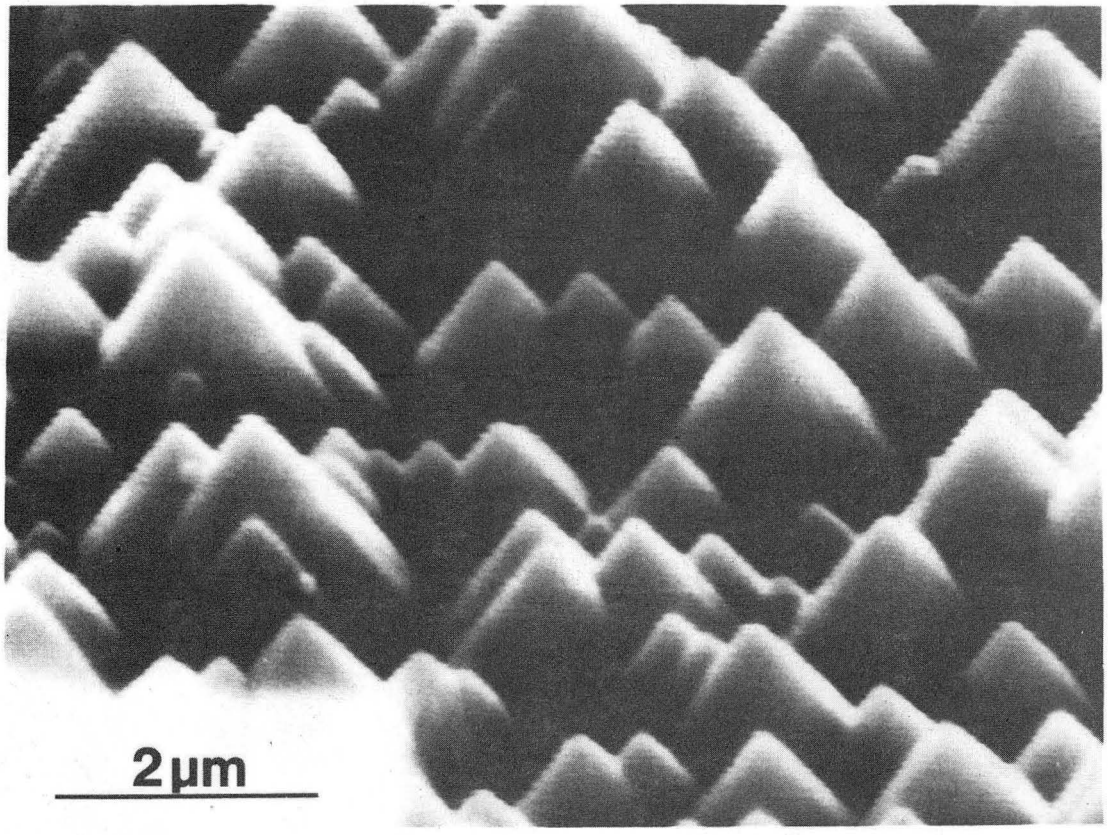

Fig. 4.2 SEM image of etched S face of CdS single crystal. Specimen was etched for 15 sec. in 37 percent HCl. XBB 830-10842

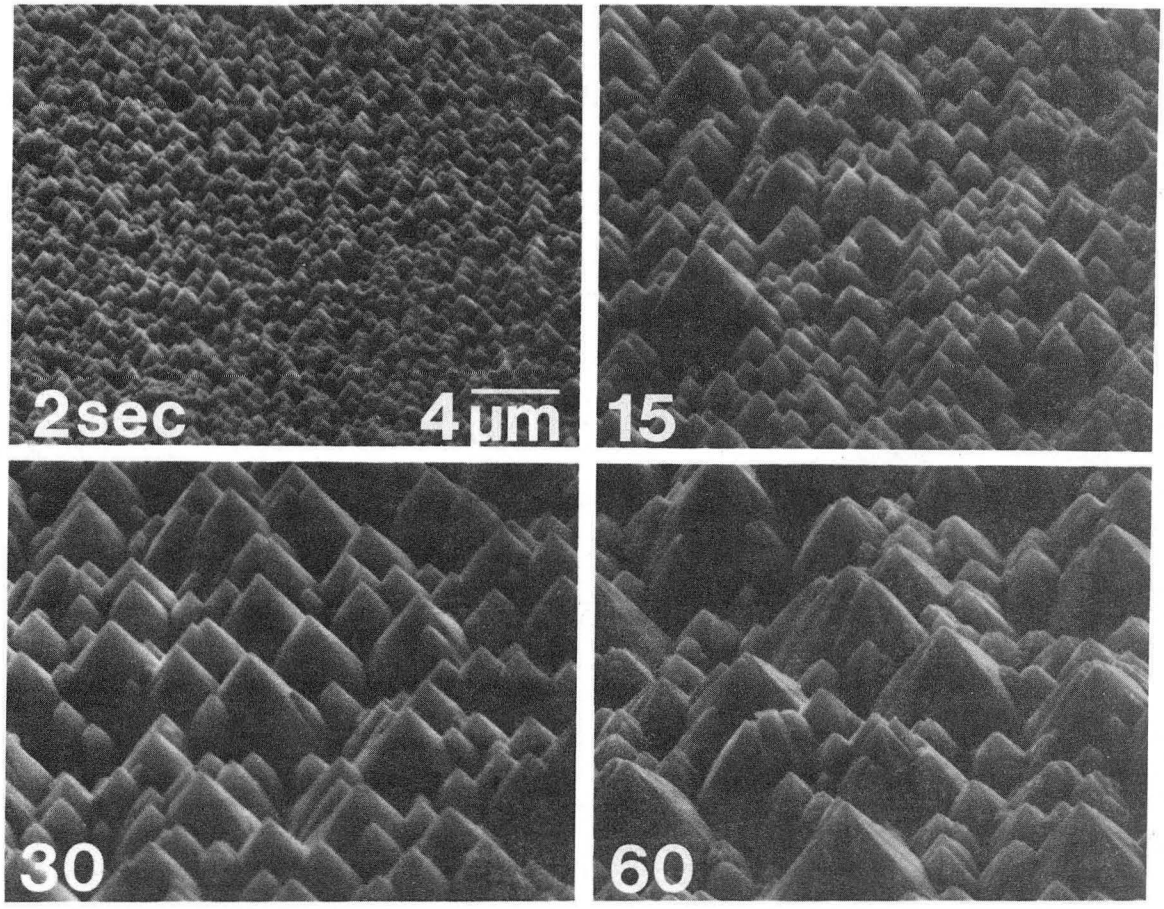

Fig. 4.3 Effect of etching time on hillock size and shape. CdS single crystal was polished and then cleaved into four pieces to insure uniformity in surface preparation before etching. Secondary hillocks are visible after 60 sec in 37 percent HCl. XBB 843-1728

37 percent HCl at room temperature. As the etching time was extended, the hillocks coarsened, but still retained their faceted sides. For etching times in excess of ~60 seconds, terraces, ledges and secondary hillocks began to form on the sides of the primary hillocks, in agreement with the observations of Oktik et al.[1] Large hillocks also showed evidence of the development of secondary ridges in the middle of the $\{\bar{2}11\bar{2}\}$ facets (Fig. 4.3). Again, this feature is indicative of slight concave etching.

4.1.2 Development of Heavily-Textured Cu_2S Films in Basally-Oriented (0001) CdS.

Micrographs of separated films at the earliest observable stage (formed during a 3-5 second immersion in the Cu_2Cl_2 bath at 99°C) indicated that the initial reaction produced small islands of low chalcocite (Fig. 4.4a). As the reaction proceeded, the islands grew laterally and coalesced. The pores remaining between the islands were, in many cases, bounded by inclusions of the tetragonal phase (Fig. 4.5).

The next stage of the reaction began at the pores. The pores acted as short-circuit diffusion paths for the reacting species resulting in a locally accelerated reaction. As the penetrations of copper sulfide deepened, the pores developed into cracks on $\{\bar{2}110\}$, the cleavage planes of CdS, thereby facilitating further reaction with the solution. A film in the final heavily textured state is imaged in Fig. 4.4b. Electron diffraction indicated that these deep penetrations of copper sulfide were primarily low chalcocite. This

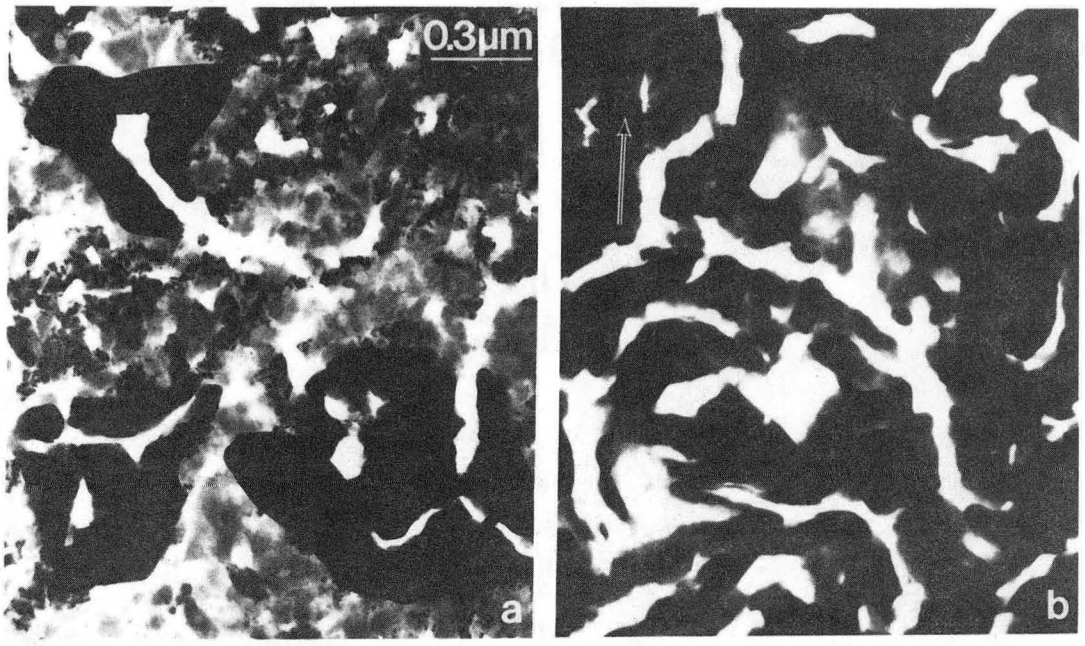

Fig. 4.4 Development of basal films. a) Separated film showing film morphology during early stages of reaction. b) Film in final highly textured state. Arrow indicates $\langle 0\bar{1}10 \rangle$ sublattice direction. XBB 839-8242

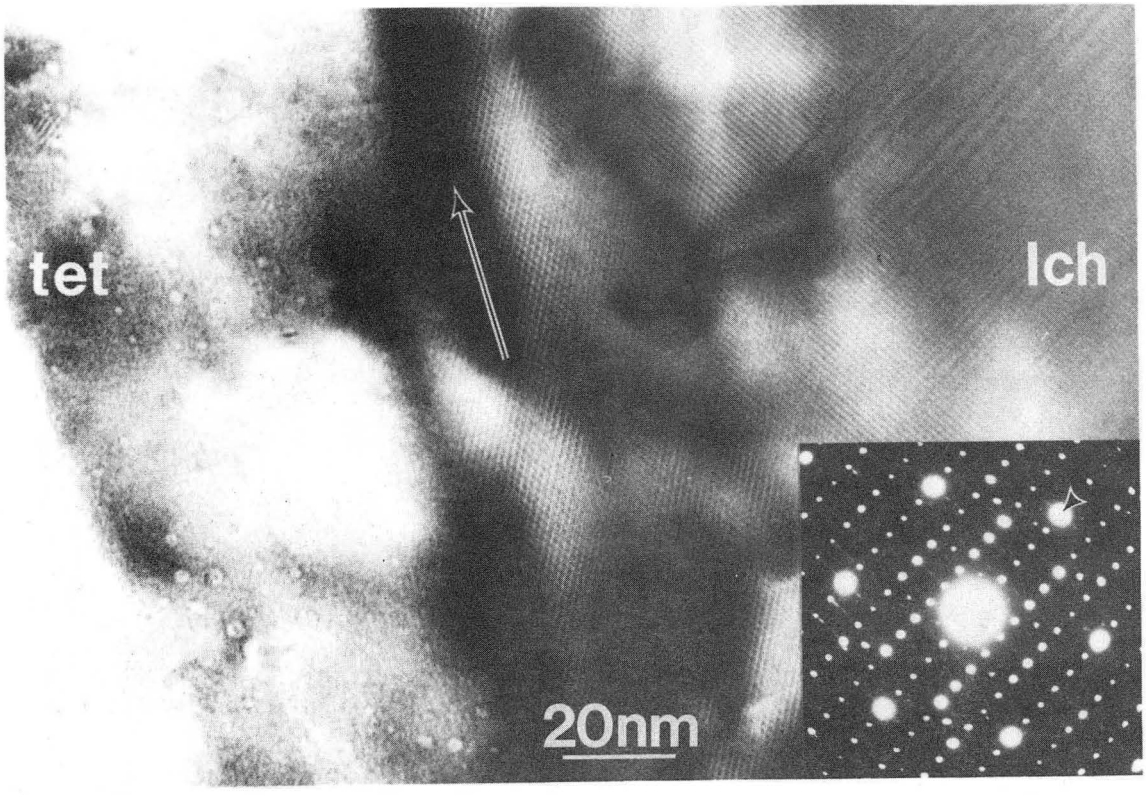

Fig. 4.5 Tetragonal phase inclusion at island edge in low chalcocite separated film. Arrow indicates a $\langle \bar{2}110 \rangle$ sublattice direction. Note antiphase boundaries on (200) planes of low chalcocite (upper right). These boundaries are commonly found in low chalcocite films grown in basal CdS substrates.[54] Low chalcocite (lch) and tetragonal phase (tet) are in [001] and $[40\bar{1}]$ zone-axis orientations, respectively. 060 lch and 020 tet spots are located at arrow in inset diffraction pattern. XBB 839-8241

result is confirmed by cross-sectional high-resolution TEM (XHRTEM) images such as Fig. 4.6. The superstructure of low chalcocite in [010] zone-axis orientation is apparent on the right side of this image near a crack. The low chalcocite-CdS interface is steeply inclined to the basal plane. In addition, a thin skin of low chalcocite ($[6\bar{4}3]$ zone-axis orientation) which formed in the early stages of the reaction is visible at the surface. However, the most important feature in Fig. 4.6 is the layer of tetragonal phase between the thin skin of low chalcocite and the CdS substrate. This "sandwich" structure was found to be a common morphological feature in films with a nominally basal surface orientation.

4.1.3 Uncracked and Twinned Cu_2S films Formed in Basally-Oriented (0001) CdS.

A second copper sulfide film morphology was observed in small regions of separated basal films. These regions, although surrounded by the heavily textured copper sulfide described above, remained thin ($\leq$30 nm) and uncracked and showed no trace of the tetragonal phase. Instead these thin low chalcocite films were found to contain a high density of plate-shaped defects on $\{0\bar{1}1\ell\}$ planes (Fig. 4.7a). These plates gave rise to extra spots in the diffraction pattern (Fig. 4.7c). The extra spots could be seen most clearly by intentionally heating the specimen with the electron beam, thereby promoting the low chalcocite-to-high chalcocite transformation and the disappearance of the superlattice spots (see Section 10.2). Dark-field images using the extra spots confirmed that they were due to the plate-shaped

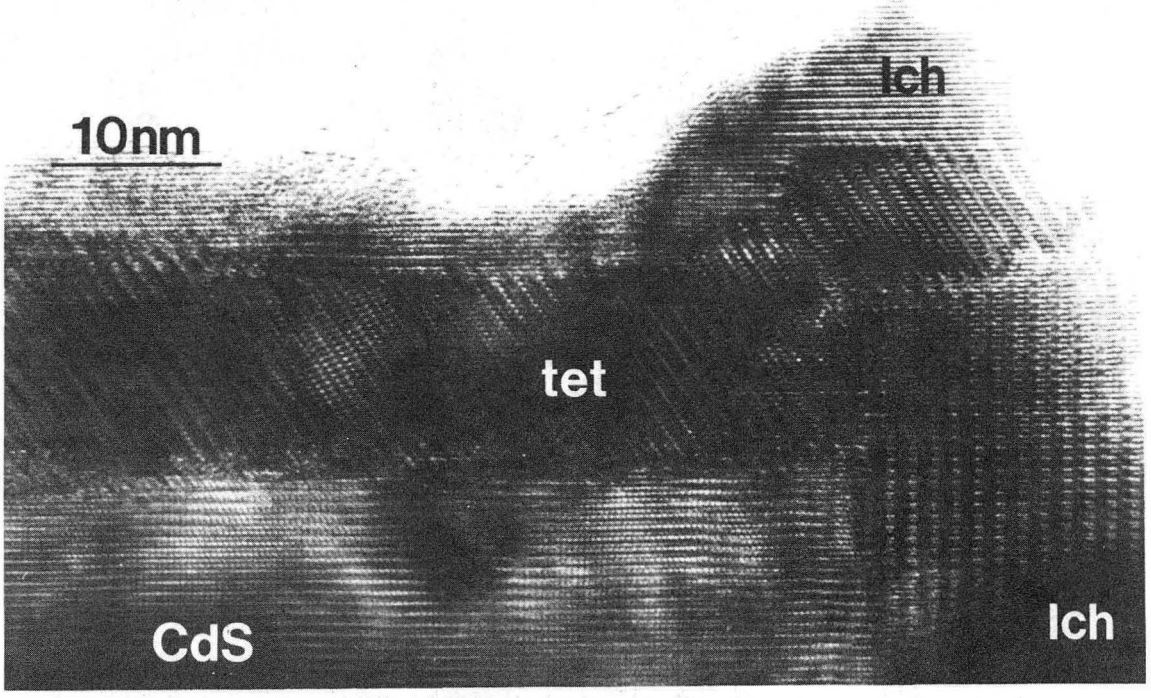

Fig. 4.6 XHRTEM image of Cu_2S/CdS heterojunction formed in 5 sec. at 99°C. First layer to form was thin skin of low chalcocite (lch) in $[6\bar{4}3]$ zone-axis orientation. Tetragonal phase (tet) is in [010] zone-axis orientation. Deep penetration of low chalcocite near crack (lower right) is in [010] zone-axis orientation. Note that tet-CdS interface is parallel to basal plane (horizontal), whereas lch-CdS interface is steeply inclined. CdS is in $[\bar{2}110]$ zone-axis orientation. XBB 830-10048

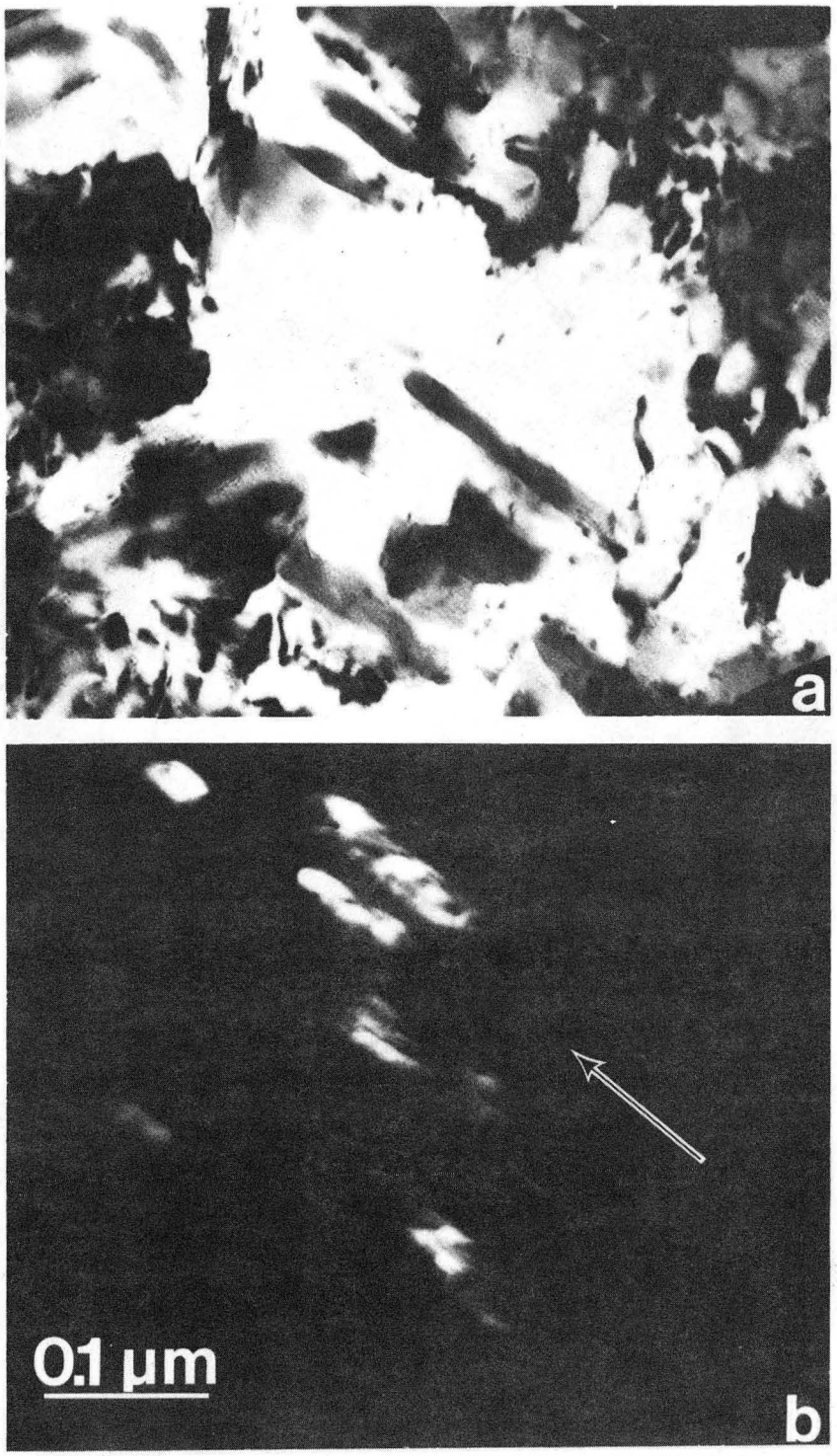

Fig. 4.7 a) Bright-field and b) dark-field micrographs of microtwins in separated copper sulfide film formed in basal facet of CdS. Dark-field was taken with $1\bar{1}02$-type twin spot. XBB 833-2667B

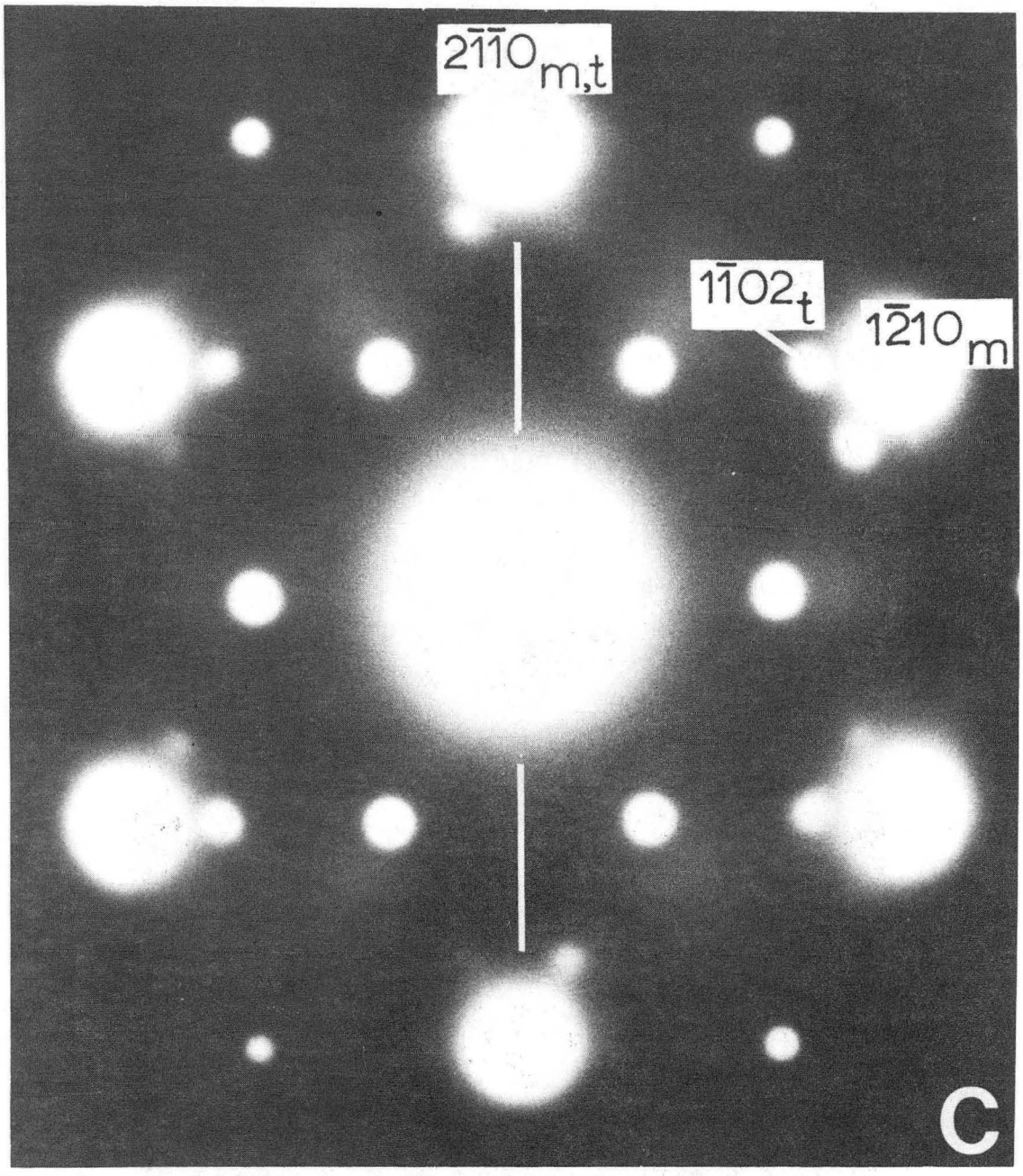

Fig. 4.7 c) Diffraction pattern in [0001] zone-axis orientation showing twin spots due to six twin variants (m is matrix, t is twin). XBB 833-2665A

defects (Fig. 4.7b). This imaging technique also revealed the presence of six defect variants (three distinguishable variants in the [0001] zone).

Excellent fit with the microscopy and diffraction data is achieved by modeling these defects as $\{0\bar{1}13\}$ reflection microtwins (Fig. 4.8). This twin effectively expands the copper sulfide lattice by 10 percent in the $<01\bar{1}0>$ direction perpendicular to the long axis of the twin. The twinning shear also has a smaller component parallel to the c axis (of the sulfur sublattice) as diagrammed in Fig. 4.8.

4.1.4 Cu_2S Films Formed in Terraced Off-Basal CdS.

Conversion of terraced surfaces such as the etch pit walls visible in Fig. 4.1 resulted in the formation of thin, uncracked films of the tetragonal phase (Fig. 4.9). These films contained a dense network of stacking faults on the inclined {111} planes of the sulfur sublattice. The XHRTEM images of Figs. 4.6 and 4.10 illustrate the basal habit of the tetragonal phase. The orientation relationship is the standard h.c.p.-f.c.c. orientation relationship:

$$\{111\}_{f.c.c.} \parallel (0001)_{CdS}$$

$$<110>_{f.c.c.} \parallel <\bar{2}110>_{CdS} \quad .$$

An overall off-basal interface orientation is accommodated by ledges at the interface (Fig. 4.10, upper right).

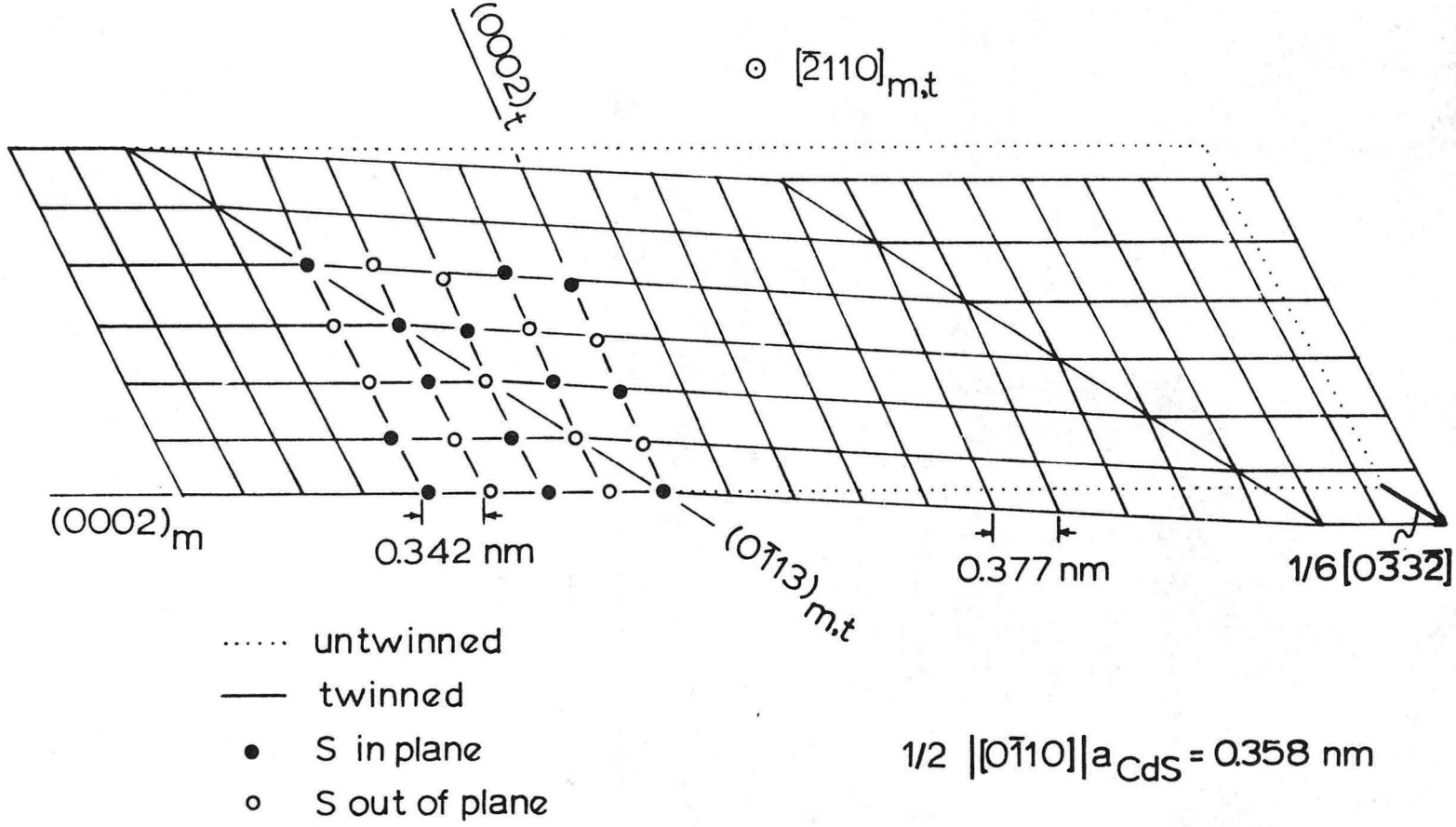

Fig. 4.8 Schematic diagram of $(01\bar{1}3)$ reflection twin viewed along $[\bar{2}110]$ direction. Note that twin effectively expands copper sulfide lattice by 10 percent in the $[01\bar{1}0]$ direction.
XBL 833-11601

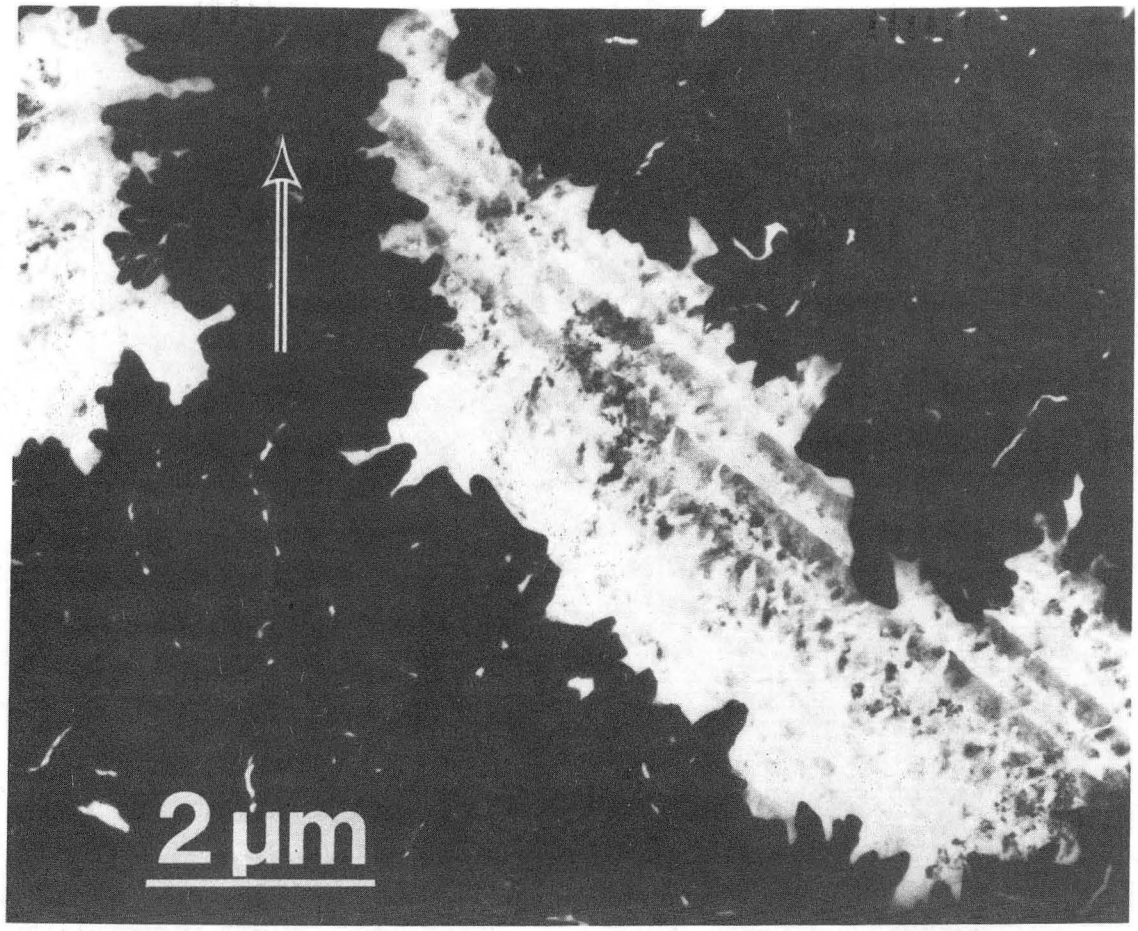

Fig. 4.9 TEM image of separated Cu_2S film. Thin portion of film is terraced etch pit wall containing the tetragonal phase. Stacking faults on {111} f.c.c. are visible. Arrow indicates $<\bar{2}110>$ direction. XBB 839-8239

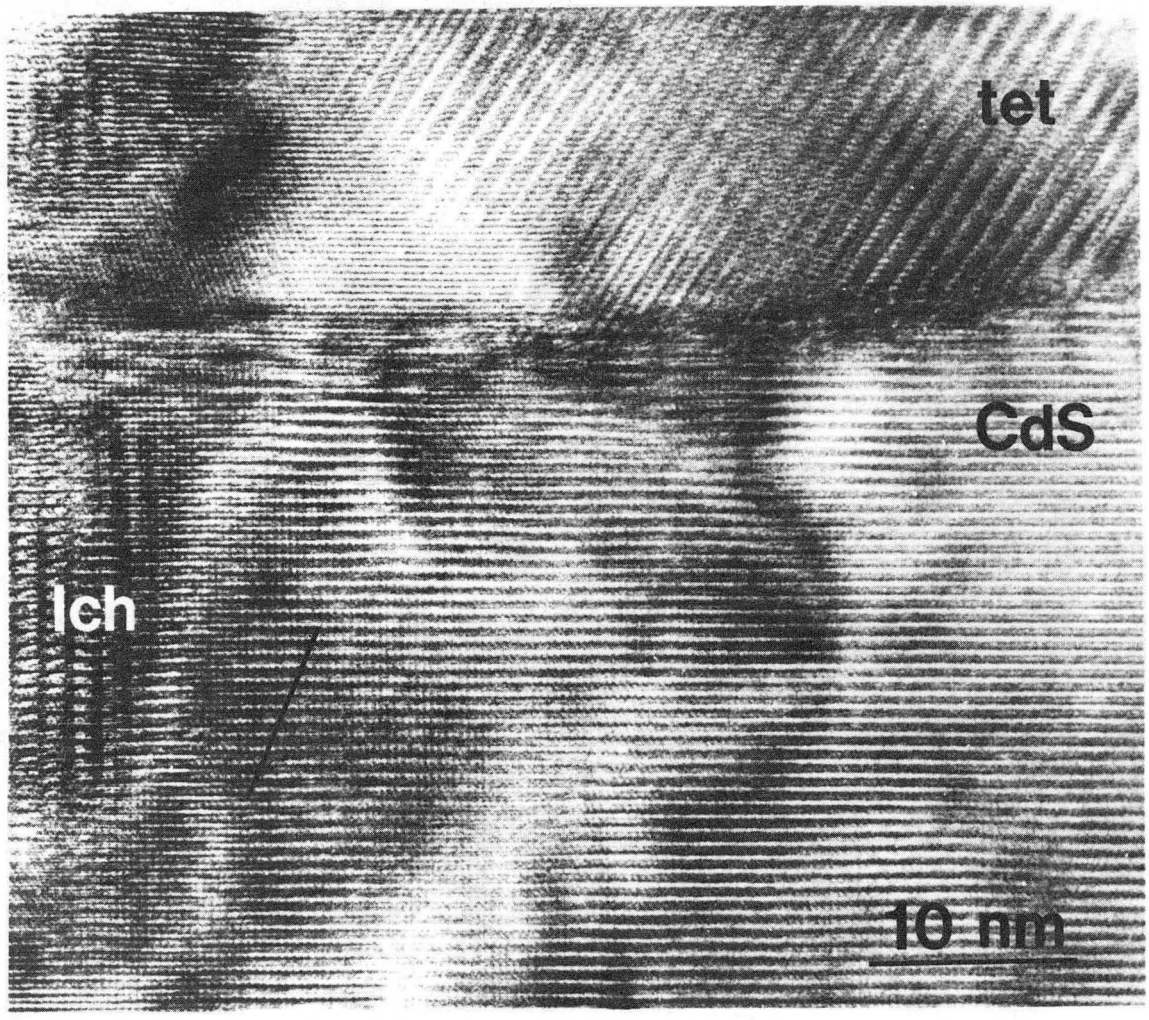

Fig. 4.10 XHRTEM image of Cu_2S/CdS heterojunction formed in 5 sec. at 99°C in the etched Cd-face of CdS. Line (lower left) indicates low chalcocite (lch)-CdS invariant line. Off-basal tetragonal phase (tet)-CdS interface is accommodated by ledges (upper right). Low chalcocite and tetragonal phase are in [010] zone-axis orientation. CdS is in $[\bar{2}110]$ zone-axis orientation. CdS basal planes are horizontal. XBB 830-10050

4.1.5 Cu_2S Films Formed in the Pyramidal Hillocks of Etched $(000\bar{1})$ CdS.

Conversion of pyramidal hillocks to copper sulfide resulted in low chalcocite films. Figure 4.11 is a XHRTEM image of a converted pyramidal hillock. Again, the low chalcocite-CdS interface is at a steep angle to the basal plane, as indicated by the low chalcocite-CdS moire' fringes due to interference between the $\{0\bar{1}10\}$ planes of CdS and the $\{400\}$ planes of low chalcocite. No tetragonal phase was detected in the films with well-developed hillocks.

Separated copper sulfide films showed that the penetration of copper sulfide was not uniform. The deepest penetrations were found at the intersections of neighboring hillocks where cracks had formed. Deep penetrations were also found along the ridges at the intersections of hillock facets. This film morphology is illustrated in Fig. 4.12.

4.1.6 Cubic Copper Sulfide Films Formed in Polished CdS Surfaces.

Oktik et al.[1] detected a polycrystalline cubic layer of CdS on the CdS surface after mechanical polishing. This result is confirmed in Fig. 4.13 by the TEM image and diffraction pattern of a separated film formed on the mechanically polished $(000\bar{1})$ CdS surface. The selected-area diffraction pattern was taken from the thin film separating the thicker protrusions of copper sulfide. The indexed diffraction pattern is that of polycrystalline cubic copper sulfide which formed topotaxially in the thin sphalerite surface layer of the unetched CdS crystal. This polycrystalline copper sulfide was only present in small patches on the separated film. Most of the separated

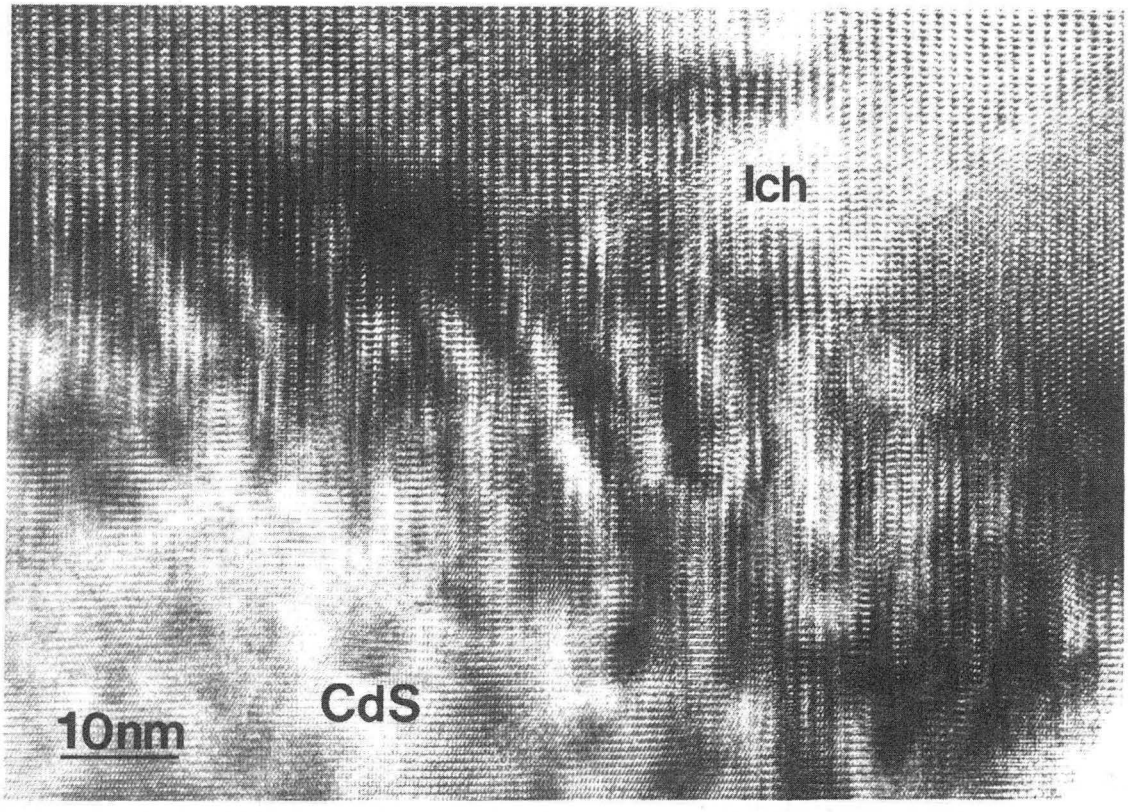

Fig. 4.11 XHRTEM image of low chalcocite (lch)-CdS interface in S-face hillock. Interface is inclined to beam direction resulting in moire' fringes. CdS basal planes are horizontal. CdS is in [$\bar{2}$110] zone-axis orientation. Low chalcocite is in [010] zone-axis orientation.
XBB 830-10049

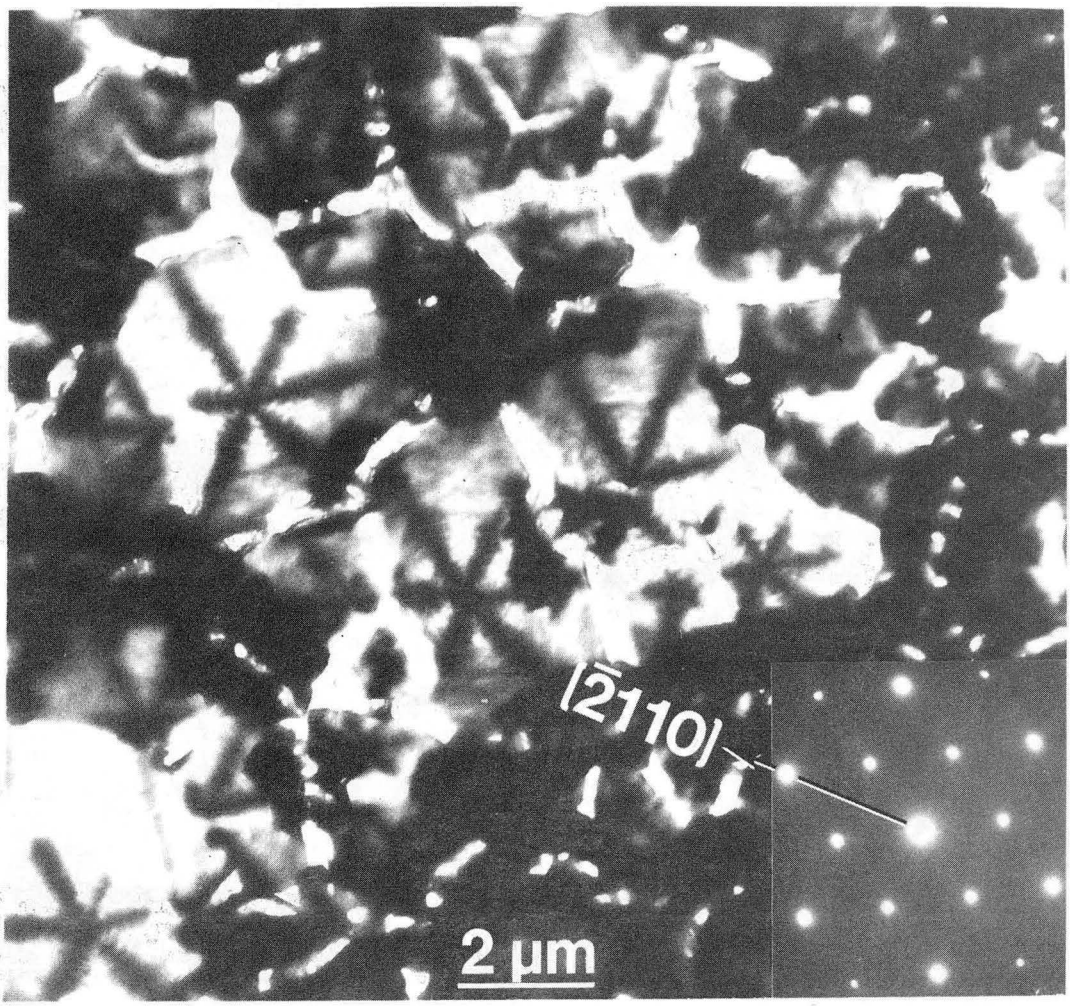

Fig. 4.12 TEM micrograph of separated copper sulfide film from etched S-face. Deep penetrations between hillocks and along hillock ridges are visible. XBB 843-1722

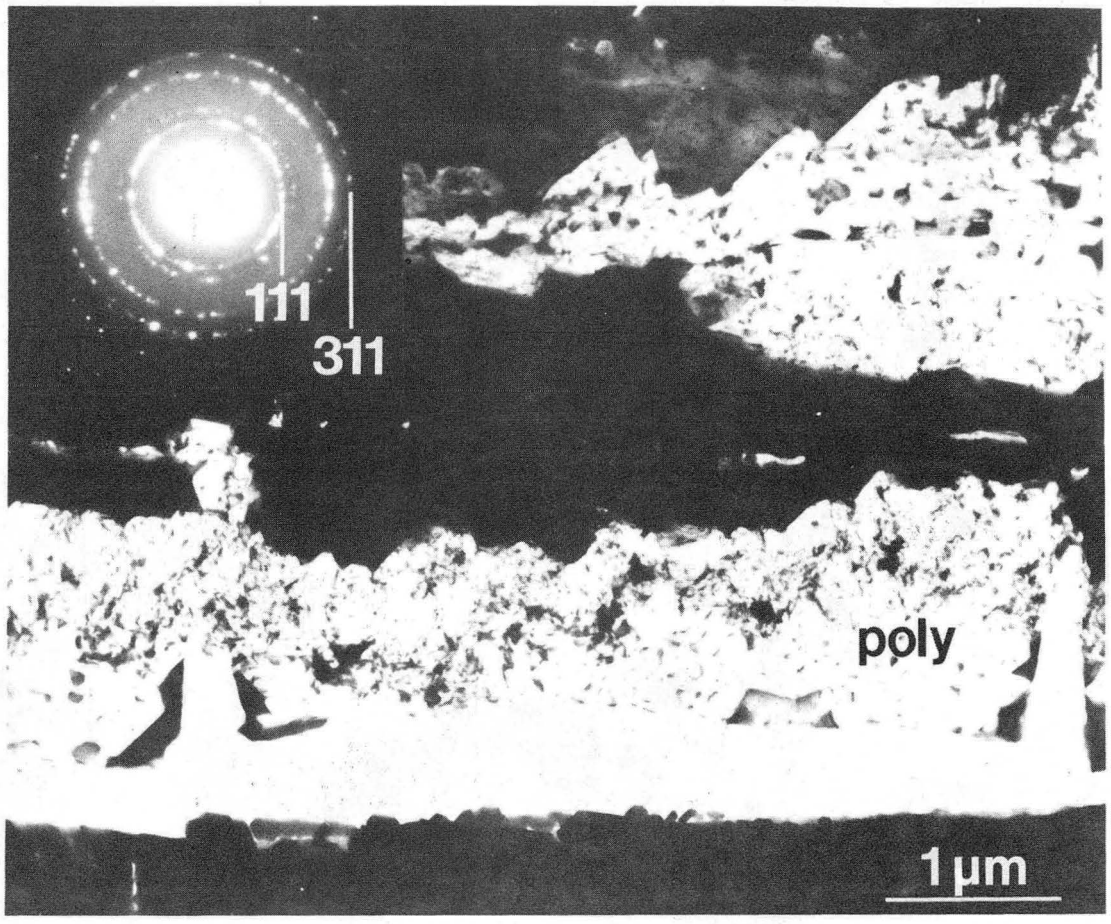

Fig. 4.13 TEM micrograph of separated copper sulfide film formed in polished and unetched CdS. Inset diffraction pattern was taken from polycrystalline cubic portion of film.
XBB 843-1723

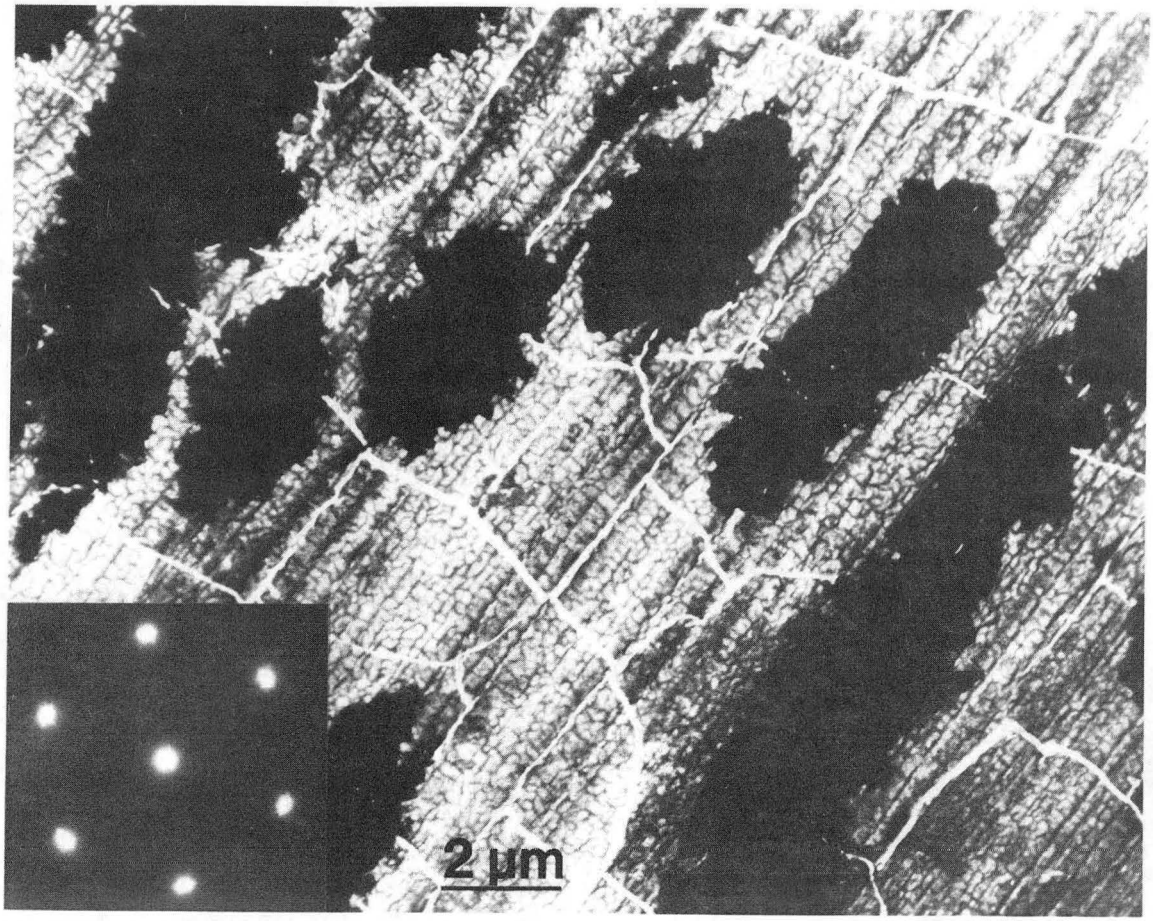

Fig. 4.14 TEM micrograph of separated copper sulfide film formed in polished and unetched CdS. Inset diffraction pattern shows predominantly cubic structure of film in [111] zone-axis orientation. Thick patches are penetrations of hexagonal copper sulfide in deep polishing scratches. XBB 843-1729

film consisted of single-crystal cubic copper sulfide (Fig. 4.14). The striations in this image are replicas of polishing scratches on the CdS surface. The deepest scratches are marked by protrusions of hexagonal copper sulfide.

The predominantly cubic structure of copper sulfide films formed in unetched basal CdS surfaces may explain the results of Cheng et al.[34] who reported that cells formed in polished and unetched surfaces demonstrated poor responses to scanning light spots.

4.2 Discussion

The observations reported in Section 4.1 can be rationalized on the basis of three factors which depend on local surface orientation; lattice misfit, the structural compatibility of the sulfur networks, and the surface nucleation of h.c.p.-to-f.c.c. transformation dislocations.

The lattice misfit between the copper sulfide phases and CdS is a strong function of surface orientation. Table 2.4 shows that the lattice misfit between low chalcocite and CdS varies from -4.7 percent to +0.5 percent as the mismatch direction is varied from $\langle 01\bar{1}0 \rangle$ to [0001]. In fact, lines of zero misfit at approximately 20° from [0001] describe a cone of unextended lines. This cone has elliptical cross-section due to the reduced symmetry of the anion sublattice of low chalcocite.

Consider an interfacial habit plane which contains corresponding unextended lines in both structures. In order to bring the two unextended lines into coincidence, one structure must be rotated

slightly relative to the other. This rotation is about an axis which is perpendicular to both of the unextended lines. After rotation (on the order of 1° for the low chalcocite-CdS couple), the superimposed unextended lines become a single "invariant line." The schematic diagram in Fig. 4.15 illustrates the invariant line construction. Dahmen[91] has demonstrated the utility of this concept in describing precipitate morphologies in alloy systems. Dahmen and Westmacott[92] have shown that matrix-precipitate interfaces generally contain an invariant line if one exists. These observations have important implications for interfacial structure since only lattice misfit perpendicular to the invariant line must be accommodated if the interfacial plane contains an invariant line.

Unlike the low chalcocite-CdS couple, the anion sublattice of the tetragonal phase is smaller than the anion sublattice of CdS in all directions. Therefore, the tetragonal phase-CdS couple does not generate a cone of unextended lines. However, the lattice misfit of directions in the basal plane (corresponding to a {111} plane in the anion sublattice of the tetragonal phase) is approximately 25 percent less than the analogous lattice misfit between low chalcocite and CdS. Thus, if the volume free energy increase due to the substitution of the tetragonal phase for low chalcocite is small compared to the reduction in interfacial strain energy due to the better fit of the tetragonal phase with CdS, then the tetragonal phase should be preferred over the equilibrium low chalcocite phase. It should also be noted that the strain energy increases with overlayer (copper

Fig. 4.15 Schematic illustration of invariant line construction a) Rectangular lattice of matrix transforms to product lattice by expansion in one direction and contraction in the other. Corresponding unextended lines result. b) By rotation of product relative to matrix, unextended lines coincide to become single invariant line. Interface containing invariant line has perfect lattice match along invariant line direction.

a.

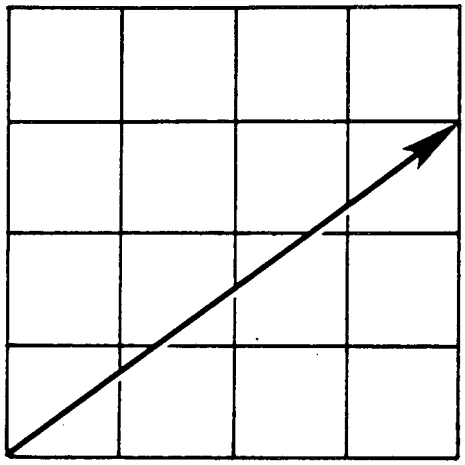

matrix

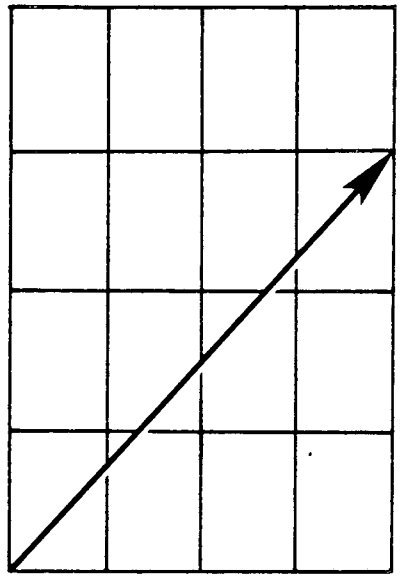

product

b.

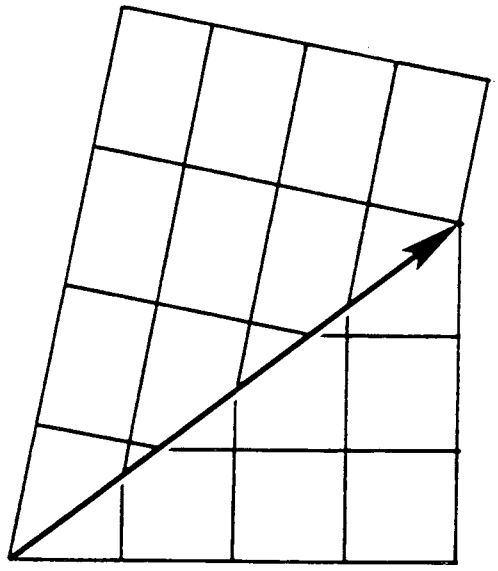

invariant line

XBL 843-1016

sulfide) thickness[8] so that there may be a critical thickness at which formation of the tetragonal phase at the interface is preferred.

In order to form the tetragonal phase, the sulfur network of the CdS must be transformed from h.c.p. to ~f.c.c. during the ion-exchange process. Such a transformation can be accomplished by the passage of Shockley-type partial dislocations with Burgers vectors $1/3 < 10\bar{1}0 >$ on every other close-packed anion plane (Fig. 4.16). since the ion exchange reaction is a low temperature process which conserves anions, the motion of Shockley partials is probably limited to glide on the basal plane. This limitation insures that either the CdS surface orientation must be off-basal so that the required density of Shockley partials can be nucleated at the surface, or some other more elaborate mechanism involving defects present before conversion must be operative. The latter possibility is unreasonable, especially for high quality single-crystal CdS. Therefore, the local surface orientation will determine whether the tetragonal phase can form during conversion. In the case of an exact basal surface, formation of the tetragonal phase should be inhibited, at least until cracks form so that the transformation dislocations can be nucleated.

In the following subsections, these structural considerations are applied to the morphological development of copper sulfide films formed in CdS substrate of various local surface orientations.

4.2.1 Heterojunctions Formed in the (0001) Basal Facet of CdS. For a flat basal surface the nucleation of transformation dislocations is hindered by the fact that the surface is parallel to the dislocation

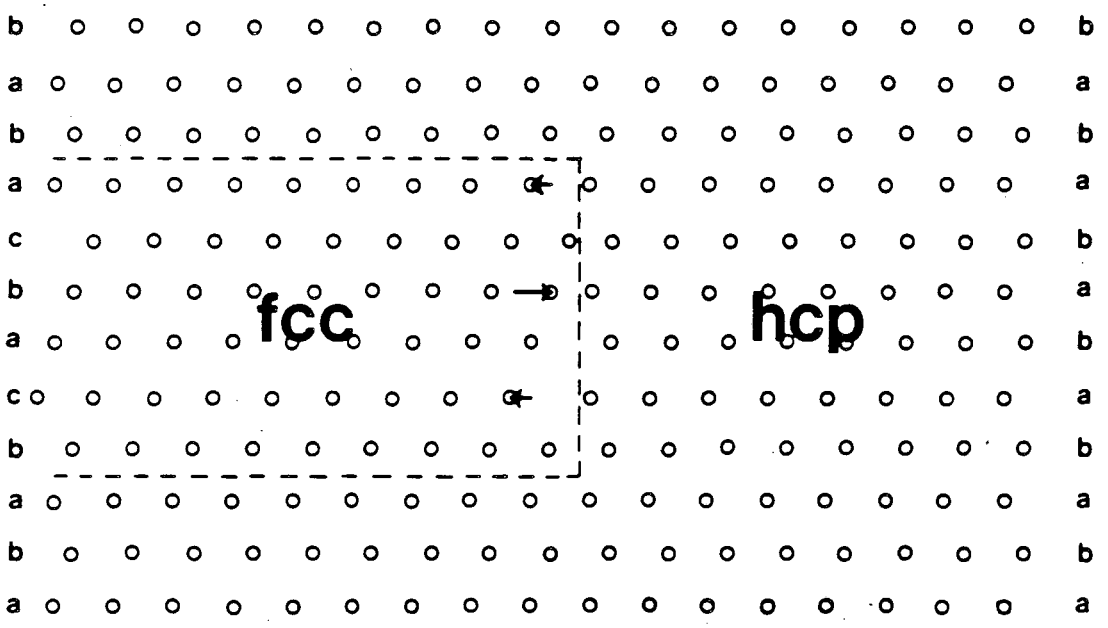

Fig. 4.16 Schematic illustration of h.c.p.-to-f.c.c. transformation by the passage of Shockley partial dislocations on every other close-packed plane. Bundle of three transformation dislocations with total Burgers vector equal to zero is shown. Projection axis is $\langle \bar{2}110 \rangle$ h.c.p., $\langle 110 \rangle$ f.c.c.

XBL 843-1017

glide plane. Thus, the first copper sulfide islands to form are low chalcocite. However, as the reaction proceeds, the strain energy due to the 4.5 percent misfit between low chalcocite and CdS increases.[8] At a critical thickness it becomes favorable to relieve the stress plastically by the introduction of cracks, misfit dislocations, or deformation twins. The introduction of misfit dislocations with Burgers vectors in the basal plane is still inhibited at this stage by the surface geometry.

From the results of Section 4.1, it appears that the reaction can go in two directions. In some areas, $\{01\bar{1}3\}$ microtwins are formed to relieve the stress and prevent cracking. These films remain thin since the reaction is limited by the transport of reactants and/or products ($CdCl_2$) through the previously formed Cu_2S. The second and more frequently observed mode of stress relief is cracking on $\{\bar{2}110\}$. These cracks expose the prism planes, thereby allowing the easy nucleation of both transformation and misfit dislocations. The tetragonal phase then forms at the Cu_2S growth front to reduce the gradient in lattice parameter between the low chalcocite and the CdS. In addition, the stress concentration at the crack tip may assist in the nucleation of the first layers of the tetragonal phase. The second consequence of cracking is that the cracks expose unconverted CdS to the Cu_2Cl_2 solution, thereby accelerating the conversion reaction. At this stage, the good fit of low chalcocite with CdS in the c-direction becomes important and the formation of the tetragonal phase is no longer preferred. Consequently, the deep penetrations of

copper sulfide at cracks (and possibly at grain boundaries) are primarily low chalcocite. The resulting film morphology is illustrated in Fig. 4.17a. If the misfit in the basal interfaces were accommodated entirely by three sets of 60° perfect dislocations (Burgers vectors of the type 1/3 $\langle 2\bar{1}\bar{1}0 \rangle$ with line vectors parallel to $\langle 12\bar{1}0 \rangle$), the perpendicular separation of parallel dislocations in the tetragonal phase-CdS interface would be ~15 nm ($\delta \cong 0.033$). A similar dislocation array with spacing 58 nm ($\delta \cong 0.012$) would be expected in the low chalcocite-tetragonal phase interface.

It should be noted that basal and near-basal interfaces are between the tetragonal phase and CdS, whereas interfaces which are steeply inclined to the basal plane are between low chalcocite and CdS.

It is also interesting that if the surface is nominally basal but rough, as in Fig. 4.6, the first phase to form is still low chalcocite. However, only a thin skin (~5 to 10 mm) of low chalcocite can form before the stress buildup necessitates the formation of the tetragonal phase. However, in the case of the etch pit walls where the surface is off-basal over several square microns, either the thin skin of low chalcocite does not form, or it is transformed to the tetragonal phase as the film thickness. The morphology of these films is discussed below.

4.2.2 Formation of Cu_2S Films in Terraced Off-Basal Surfaces.

The formation of the tetragonal phase in large area (>1 μm^2) off-basal surfaces is not restricted by the lack of suitable nucleation sites for transformation dislocations. Consequently, the

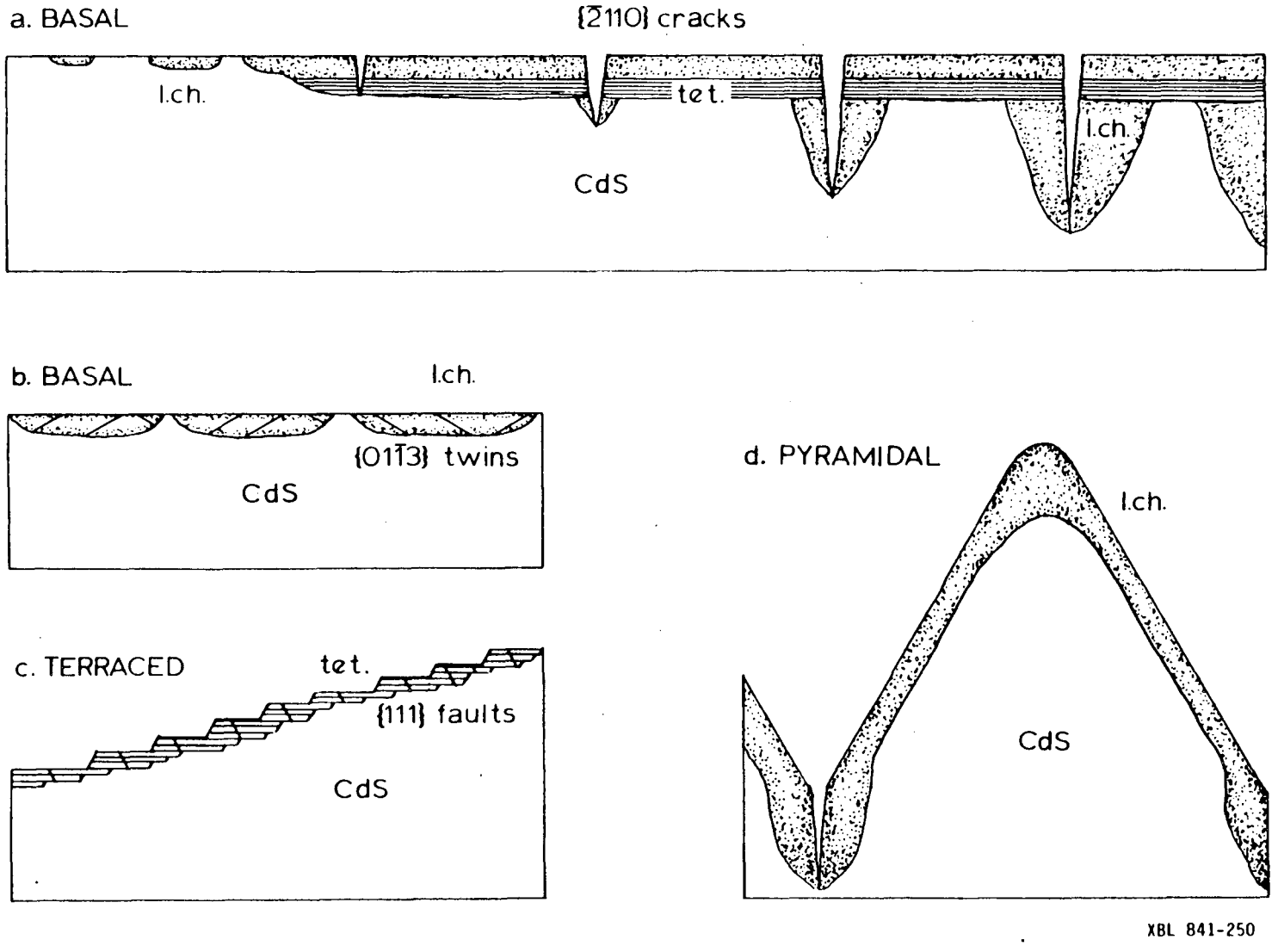

Fig. 4.17 Schematic diagram of observed Cu_2S/CdS heterojunction morphologies in cross-section.

tetragonal phase forms in the early stages of the reaction. Rather than nucleating from cracks, the transformation dislocations can nucleate at the surface. Therefore, a thin skin of low chalcocite, if formed at the outset, will be transformed to the tetragonal phase by the passage of transformation dislocations through the surface layer. Stress due to residual misfit between the tetragonal phase and the CdS can be reduced by the introduction of misfit dislocations from the surface by glide on the three sets of inclined {111}-type planes. Thus, the small component of misfit in the c-direction can also be accommodated. In addition, misfit in one direction in the basal plane can be accommodated by the shape change due to unequal numbers of the three transformation partial dislocations. For example, if the surface normal were 10° from [0001] toward $[01\bar{1}0]$, a sequence of partials $\ldots\vec{\alpha}\vec{\beta}\vec{\alpha}\vec{\gamma}\vec{\alpha}\vec{\beta}\vec{\alpha}\vec{\gamma}\ldots$, where $\vec{\alpha}$, $\vec{\beta}$ and $\vec{\gamma}$ represent the three Burgers vectors of the type 1/3 $<01\bar{1}0>$, would accommodate a misfit of ~1.6 percent in the $\vec{\alpha}([0\bar{1}10])$ direction. The "extra" $\vec{\alpha}$ partials would have a spacing in the interface plane of ~14 nm and a vertical spacing of ~2.5 nm (~4 $\vec{c}_o$). Of course, misfit accommodation by this shape change is impossible if the interface between the tetragonal phase and CdS is on the basal plane (i.e. no transformation dislocations in the interface).

This shape change mechanism can accommodate misfit in only one direction. The remaining misfit must be accommodated elastically or by slip on the inclined {111} sublattice planes. Stacking faults on {111} due to the passage of partial dislocations are visible in Fig. 4.9. Since mismatch can easily be accommodated, these off-basal films remain uncracked and thin.

4.2.3 Heterojunctions Formed in the Pyramidal Hillocks of the Etched $(000\bar{1})$ CdS Surface.

As described in Section 4.1.1, the pyramidal hillocks of the etched sulfur face exhibit complicated surface structures. If the $(000\bar{1})$ surface is etched for ~30 seconds in fresh 37 percent HCl, the hillocks are fairly uniform with $\{\bar{2}11\bar{2}\}$ facets inclined by ~58° to the basal plane.

The formation of the tetragonal phase in $\{\bar{2}11\bar{2}\}$ facets would require a high density of transformation dislocations at the interface with CdS (one Shockley partial every 0.8 nm in the $<\bar{2}113>$ direction), thereby increasing the interfacial energy. In addition, the 2.5 percent misfit between the tetragonal phase and CdS in the c-direction would further discourage the formation of the tetragonal phase. Since the cone of unextended lines for the low chalcocite-CdS couple is at ~70° to the basal plane, the $\{\bar{2}11\bar{2}\}$ facets provide favorable sites for the formation of low chalcocite. In fact, the misfit is less than one percent along the $<\bar{2}113>$ direction which lies in the $\{\bar{2}11\bar{2}\}$ plane. However, since the mismatch along the $<01\bar{1}0>$ direction is significant (~4.4 to 4.7 percent), and since dislocations which could accommodate this mismatch would have to move by a climb mechanism, the deep penetrations of low chalcocite are limited to hillock ridges (Fig. 4.12) and to the regions near cracks at the hillock bases.

The results of this discussion can be summarized by noting that whenever the nominal (local) surface orientation is ~60° or more from the basal orientation, the formation of low chalcocite is preferred.

Conversely, when the nominal (local) surface orientation is within ~30° of the basal orientation, the tetragonal phase will form at the interface with CdS (provided nucleation sites for transformation dislocations are available).

In the case of an over-etched $(000\bar{1})$ surface with secondary hillocks, terraces, ledges, and kinks, the nominal surface orientation is likely to be nearly basal in some areas. As in the terraced etch pit walls of the etched cadmium face, the tetragonal phase may form in these over-etched areas. The high density of h.c.p.-to-f.c.c. transformation dislocations at inclined tetragonal phase-CdS interfaces may contribute to the poorer efficiencies[1] of cells formed on the over-etched or mechanically damages surfaces. Furthermore, Oktik et al.[1] observed that the efficiency of terraced cells improved during short post-conversion heat treatments whereas heat treatment of cells with faceted hillocks had a deleterious effect. This observation suggests that some constituent of the heat treatment atmosphere, perhaps oxygen, acts to compensate the unsatisfied bonds in the cores of transformation dislocations at inclined tetragonal phase-CdS interfaces. If the unsatisfied bond density is low (i.e., faceted hillocks) the air heat treatment serves only to deplete the low chalcocite of copper, thereby degrading the photovoltaic characteristics.

5. TRANSFORMATIONS TO COPPER DEFICIENT PHASES

5.1 Effect of Conversion Temperature on Copper Sulfide Stoichiometry

In an effort to verify the results of Caswell et al.[27] (Section 1.4.1), copper sulfide films were formed in Cu_2Cl_2 baths at temperatures between 65 and 100°C. Separated films were prepared and examined by TEM and diffraction. Copper sulfide films formed in the basal (0001) CdS surface at 99°C for 12 seconds were found to be entirely low chalcocite and the tetragonal phase (Fig. 5.1a). Films formed at 65° for 100 seconds consisted of only djurleite (Fig. 5.1c). At intermediate temperatures, the films were found to be mixtures of low chalcocite and djurleite.

In addition to the stoichiometry variations, the film morphology varied with ion-exchange reaction temperature. At a conversion temperature of 99°C, the cracks were found to be separated by ~2 μm (Fig. 5.1b). Whereas, films converted at 65°C contained closely-spaced pores but no large cracks (Fig. 5.1d).

As described in Section 3.1, the CdS single-crystals were pre-heated to the desired conversion temperature before immersion in the Cu_2Cl_2 solution. The effects of thermal inertia were investigated by mounting the CdS crystals to glass slides and eliminating the pre-heating step. Separated films from mounted specimens were invariably low digenite or low digenite-djurleite mixtures. Figure 5.2 is a HRTEM micrograph of a low digenite ($6a_o$) film formed by immersion of a mounted CdS crystal into a Cu_2Cl_2 bath at 99°C for 12 seconds. The micrographs and the <110> diffraction

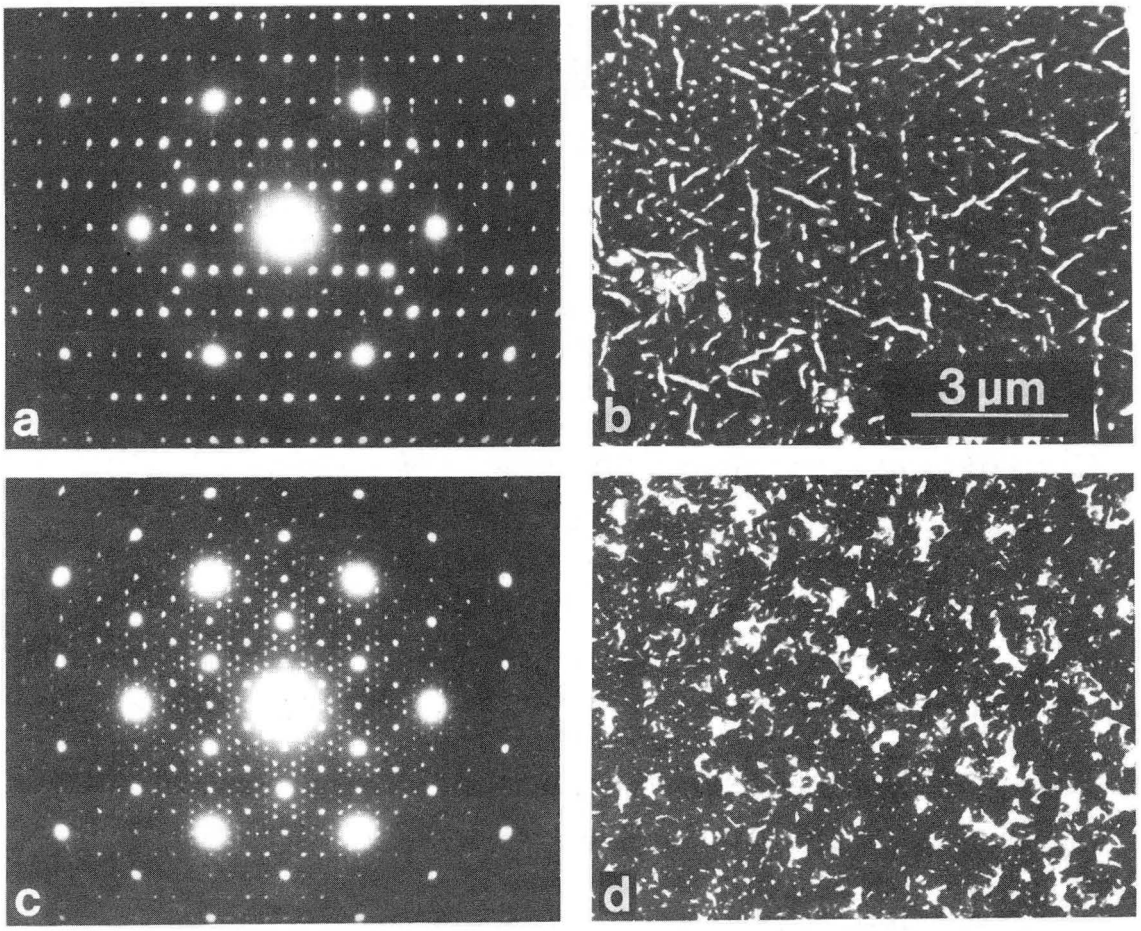

Fig. 5.1 Effect of conversion temperature on copper sulfide phase and film morphology. a) Diffraction pattern of film formed at 99°C for 12 sec. Low chalcocite and three distinguishable variants of tetragonal phase are in [001] and [40$\bar{1}$] zone-axis orientations, respectively. b) Micrograph corresponding to diffraction pattern in a). c) Diffraction pattern of film formed at 65°C for 100 sec. Three distinguishable variants of djurleite are in [100] zone-axis orientation. d) Micrograph corresponding to diffraction pattern in c). Both films were formed in basal facet of etched Cd-face. XBB 837-6420A

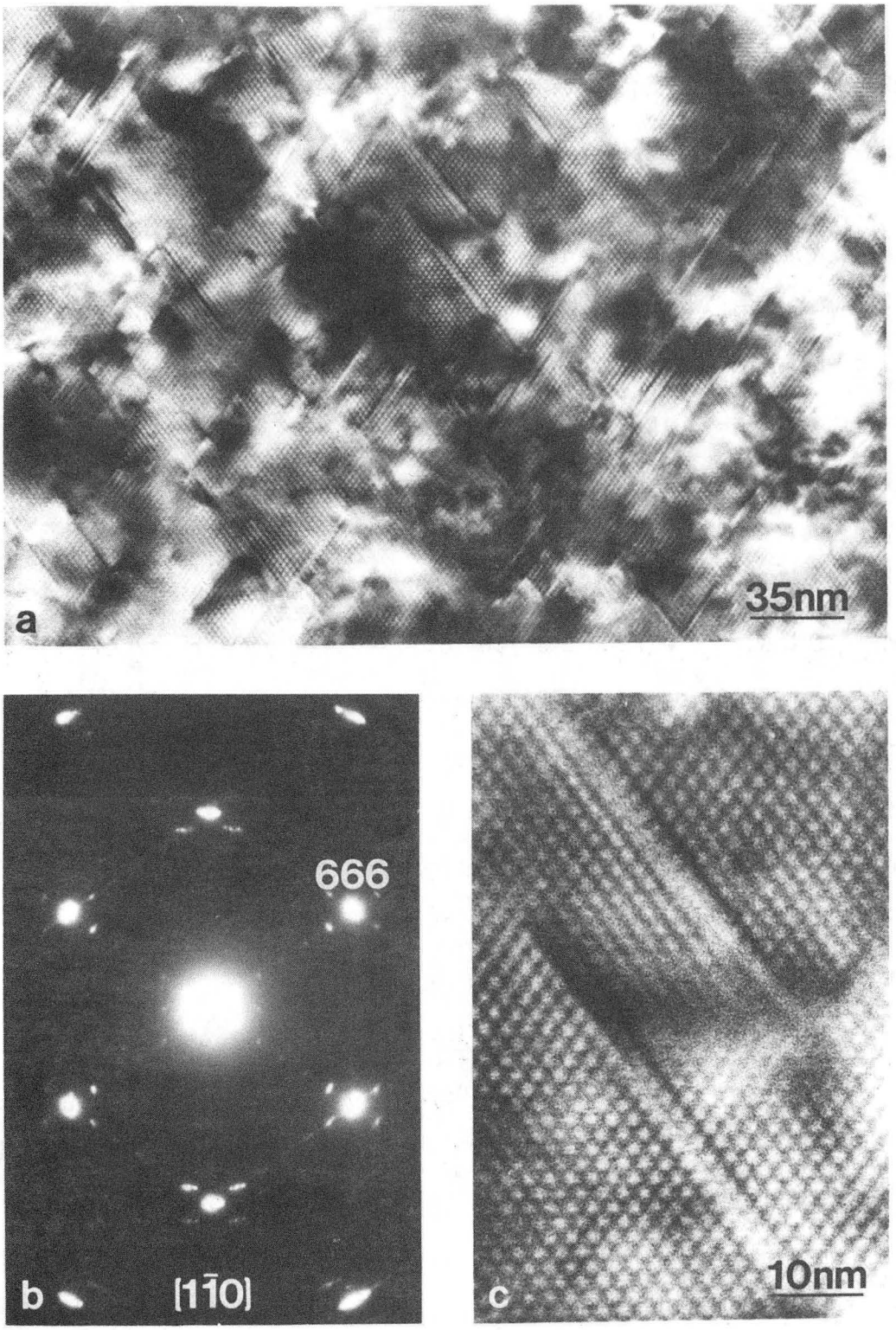

Fig. 5.2 a) HRTEM image of low digenite film formed in Cd-face of CdS. Film is tilted to [1$\bar{1}$0] zone-axis orientation to reveal low digenite ($6a_o$) superlattice and {111} stacking faults. b) Corresponding [1$\bar{1}$0] diffraction pattern. c) higher magnification image of stacking faults. XBB 820-10003A

pattern were obtained by tilting the specimen from <111> to <110> zone-axis orientation. The high density of {111} stacking faults may serve to relieve stresses due to the significant (~5.4 percent) mismatch between low digenite and CdS.

Low digenite-djurleite films examined in cross-section exhibited a complex arrangement of alternating thin plates of djurleite and low digenite ($6a_o$). Figure 5.3 shows that djurleite-low digenite interfaces are flat with the basal plane of the djurleite sulfur network parallel to a {111} plane of low digenite. Also visible in this image are two variants of low digenite. This observation is consistent with the fact that the close-packed sulfur layers can stack in either ABCABC order or CBACBA order. The twin boundaries (Fig. 5.3), lie on {112} planes and consist of stacks of Shockley partial dislocations. Examination of the djurleite-low digenite interface in Fig. 5.4 shows that the interface is completely coherent. This result is expected since the mismatch in the close-packed plane is $\leq$0.2 percent.

5.2 Degradation at Room Temperation

Although the low chalcocite-to-djurleite mechanism of low temperature (20-70°C) degradation in air is fairly well established, very little is known about djurleite nucleation in low chalcocite and the atomic rearrangement required for the transformation. In order to investigate the microstructural changes during low temperature aging, plan-view CdS TEM specimens were prepared by argon ion-milling. The specimen surface layers were converted to $Cu_{2-x}S$, resulting in

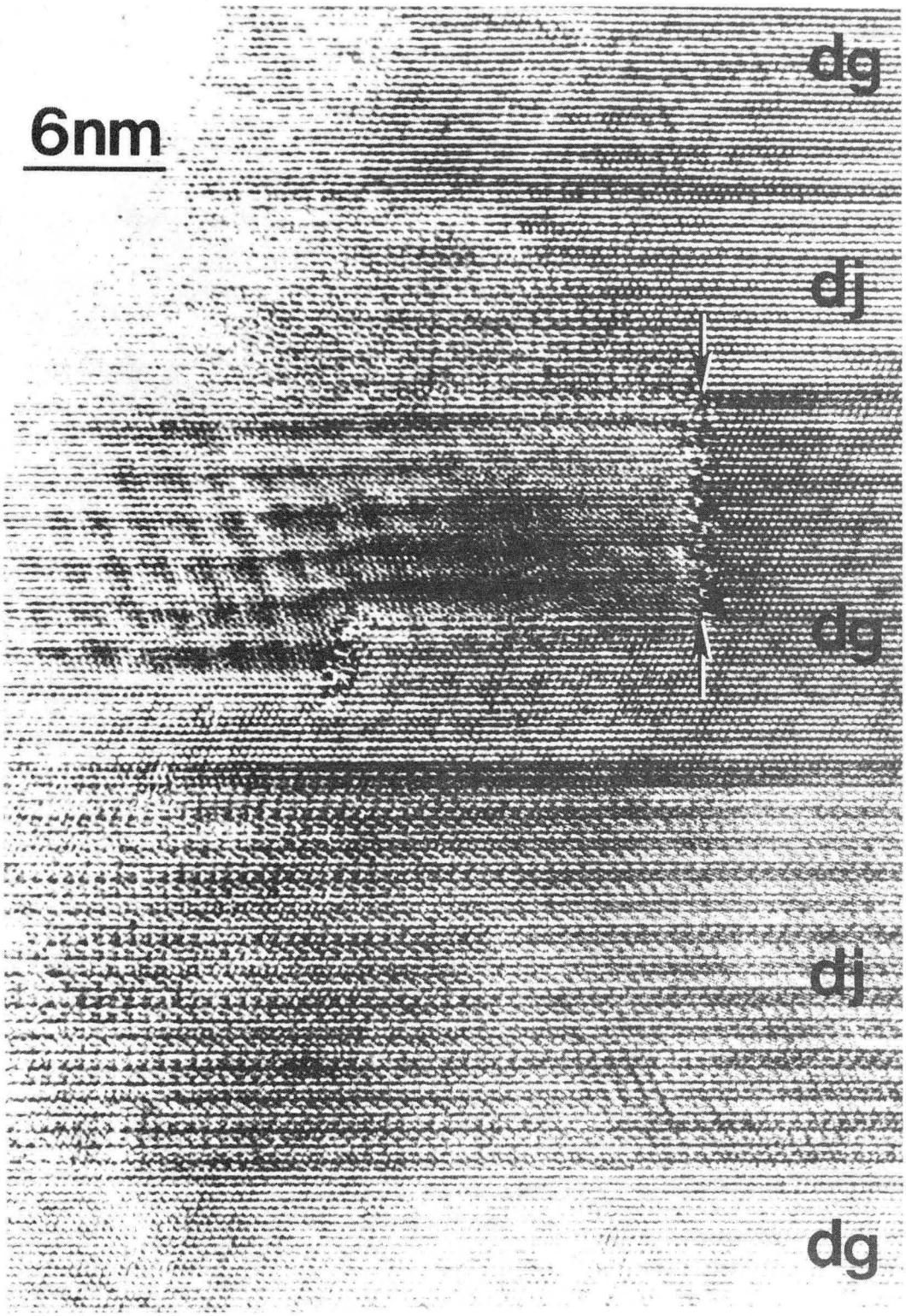

Fig. 5.3 XHRTEM image of djurleite-low digenite ($6a_o$) film formed in the etched S-face of CdS. Horizontal djurleite-low digenite interfaces are basal. Twin boundary on {112} low digenite is indicated by arrows. Low digenite and djurleite are in $[1\bar{1}0]$ and [012] zone-axis orientations, respectively. XBB 843-1727

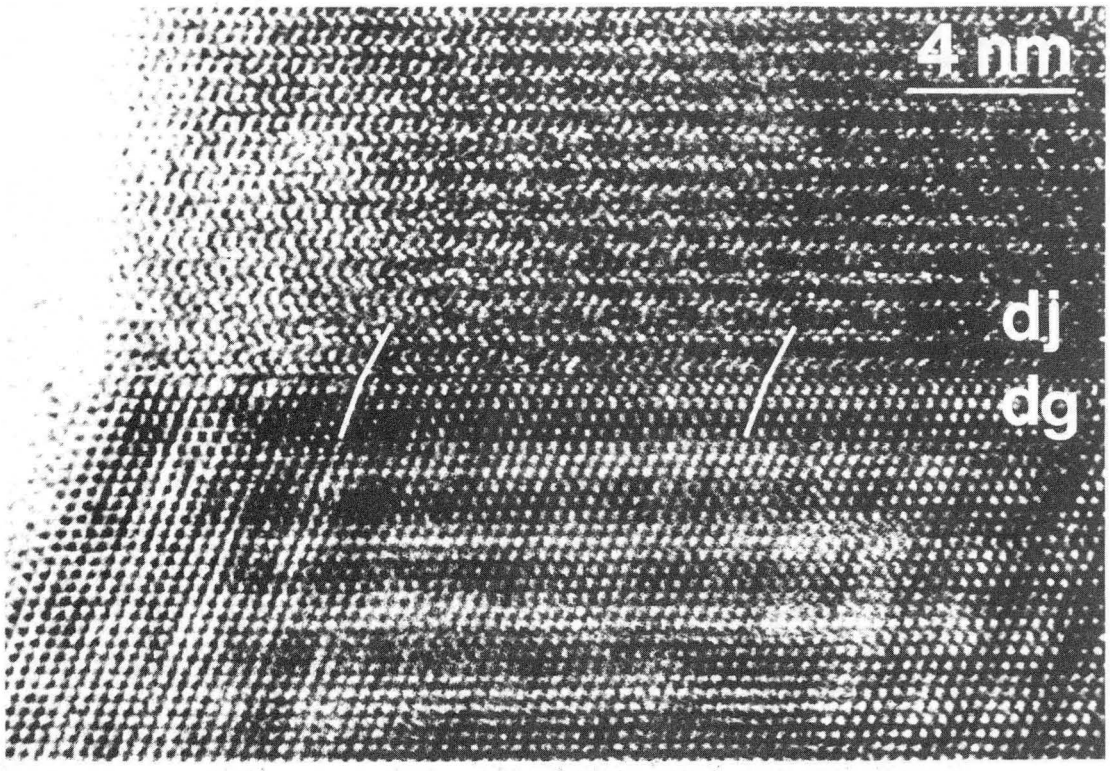

Fig. 5.4 Higher magnification XHRTEM image of low digenite ($6a_o$)-djurleite interface. Interface is on the basal plane and is completely coherent. Low digenite and djurleite are in $[\bar{1}10]$ and [012] zone-axis orientations, respectively. XBB 843-1725

complete conversion of the thin areas to copper sulfide. Specimens were examined in the as-plated condition and then the same areas were re-examined several days later after aging in laboratory air at room temperature. Figure 5.5 shows a djurleite domain which nucleated at a crack and grew in the four days following conversion to low chalcocite. Note that the apparently rectangular lattice of djurleite is rotated 60° with respect to the rectangular lattice of low chalcocite. This fact and the observed shape of the djurleite domain will be discussed in Section 5.4.1.

5.3 Effect of Air Heat Treatments at 150°C

The formation of copper oxide at the $Cu_{2-x}S$ surface during heat treatment is generally agreed upon. However, the morphology of the oxide layer is unknown. In addition, sulfur loss during heat treatment has been reported by Arjona et al.[93] Rickard[94] has observed $CuSO_4 \cdot 5H_2O$ production during x-ray analysis of chalcocite. Czanderna et al.[95] also reported the formation of $CuSO_4$ during heat treatment of copper sulfide. Finally, Loferski et al.[80] have suggested that a $Cu_xS_y O_{1-y}$ semiconductor layer forms during heat treatment in air. The question of which compounds form during air exposure is important since the stoichiometry of the copper sulfide layer will depend on the relative amounts of copper and sulfur that leave the sulfide during heat treatment.

In order to determine the effect of heat treatment on the stoichiometry of the copper sulfide layer, as-prepared heterojunctions were subjected to heat treatments in air at 150°C for various lengths

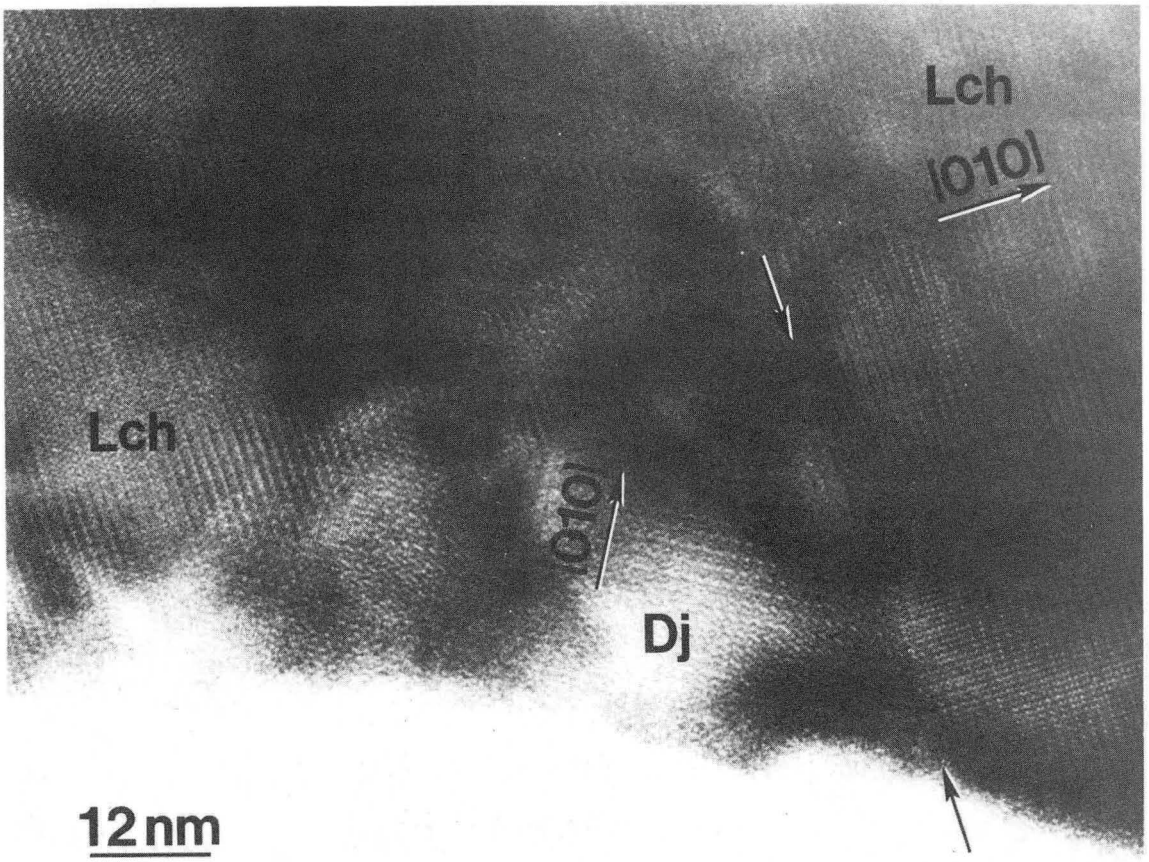

Fig. 5.5 HRTEM image of djurleite (Dj) inclusion in low chalcocite (Lch). Djurleite was formed after four days exposure to laboratory ambient. Djurleite variant is O.R. 60° (described in text). Flat low-misfit interface is indicated by arrows. Djurleite and low chalcocite are in [100] and [001] zone-axis orientations, respectively. XBB 831-733B

of time. The heat treated films were separated and examined in the TEM. Figure 5.6 is a diffraction pattern from a copper sulfide film which was heat treated for 45 minutes before separation. The diffuse rings correspond to the 111 and 220 cuprite (Cu_2O) plane spacings. The dark-field micrograph using a portion of the 111 ring shows that the oxide is in the form of small particles 5 to 10 nm in diameter (Fig. 5.7). In addition, the diffraction pattern shows no evidence of the copper-deficient phases, djurleite and low digenite. Thus, even after extended heat treatment at 150°C, the film is entirely low chalcocite and the tetragonal phase. This result suggests that sulfur may also react during heat treatment at 150°C so that the 2:1 stoichiometry of the copper sulfide layer is preserved.

It should also be noted that the effect of heat treatments is likely to vary with temperature. Heat treatment at 200°C has been shown to reduce the short circuit current output in single crystal cells,[1] suggesting that at 200°C there is a net loss of copper by oxidation of the surface and/or by diffusion into the CdS.

5.4 Structural Rearrangements during Transformations to Copper-Deficient Phases

5.4.1 The Low Chalcocite-to-Djurleite Transformation.

An atomic model for the rearrangement of copper ions during the low chalcocite-to-djurleite transformation is described below. Since much of this work has been published,[54,55] only the essential aspects of the model are presented here.

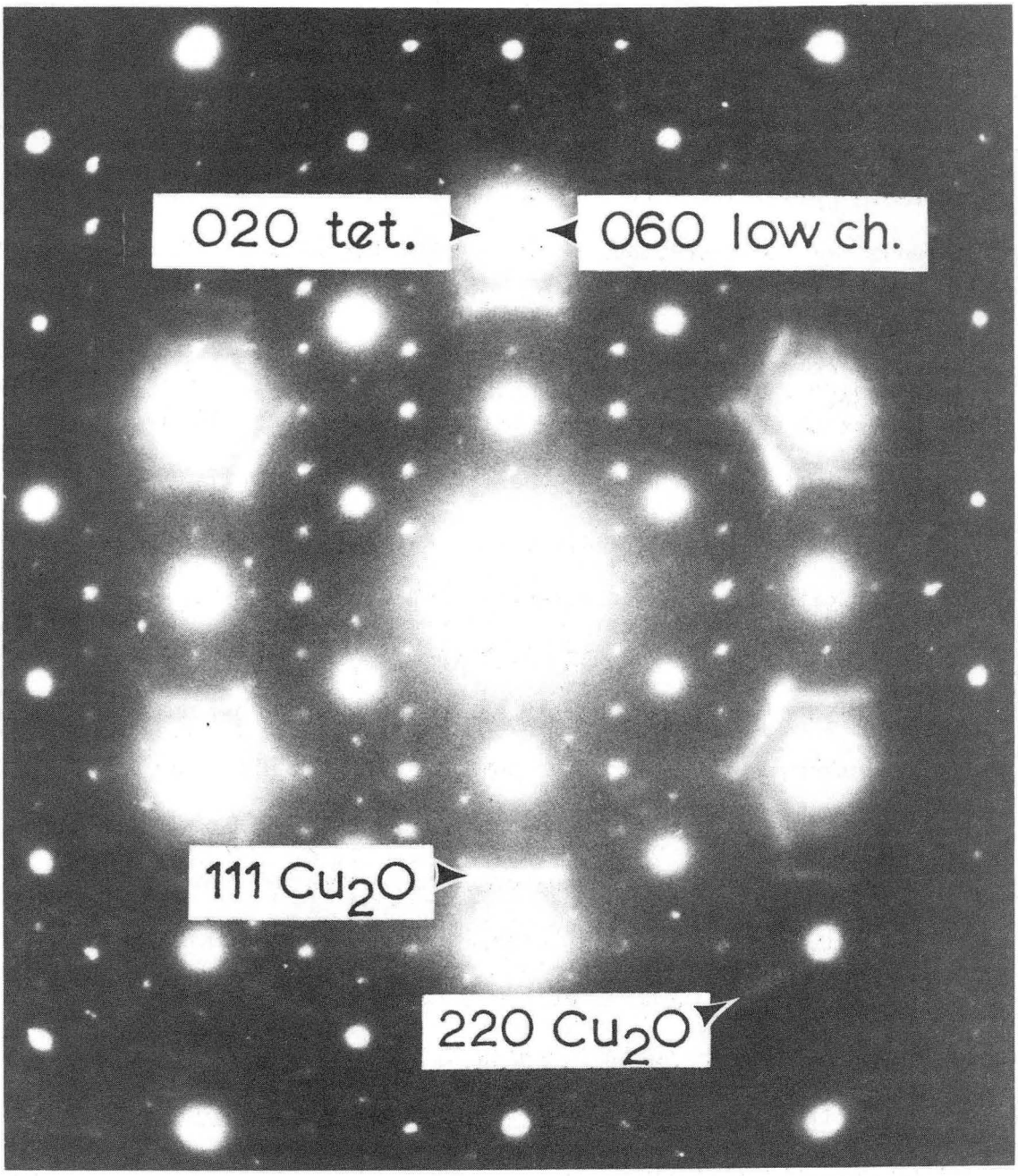

Fig. 5.6 Diffraction pattern from copper sulfide film separated after heat treatment in air for 45 min. at 150°C. Spot patterns of multiple variants of low chalcocite and tetragonal phase are visible. Ring pattern corresponds to cuprite (Cu_2O). Each strong sublattice spot acts as secondary source, giving rise to multiple ring patterns. XBB 837-6417

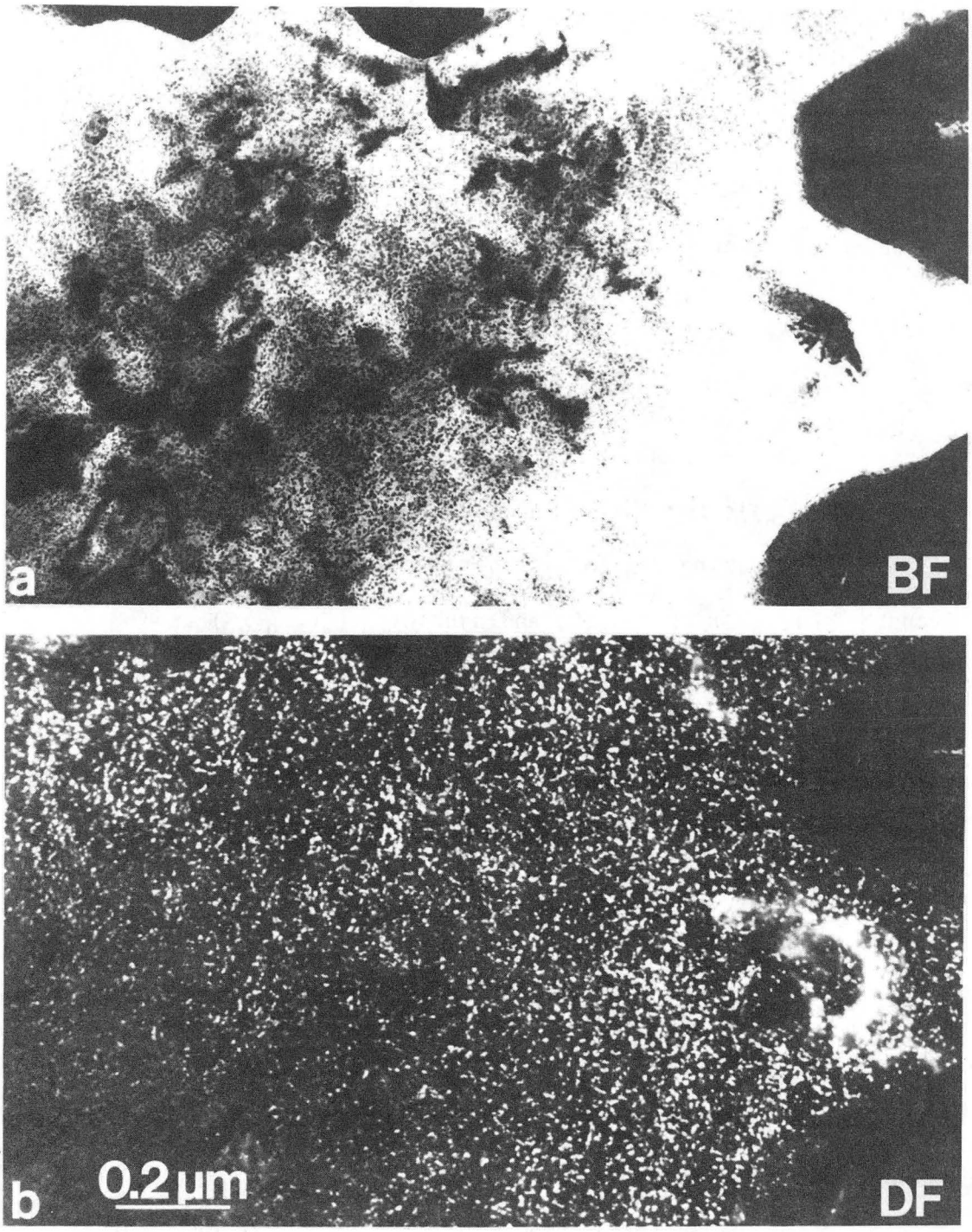

Fig. 5.7 Bright-field/dark-field pair corresponding to diffraction pattern of Fig. 5.6. Dark-field image, using portion of 111 ring of cuprite, reveals cuprite particles 5 to 10 nm in diameter. XBB 837-6418

Figure 5.8 illustrates the relationships of the unit cells of low chalcocite and djurleite to the h.c.p. sulfur network of high chalcocite. In this c-axis projection it is clear that there are two possible orientation relationships (O.R.'s) between the pseudo-rectangular lattices:

O.R. 0° $\quad \measuredangle ([010]_{LCh}, [010]_{Dj}) = 0°, \quad 180°$

O.R. 60° $\quad \measuredangle ([010]_{LCh}, [010]_{Dj}) = 60°, \quad 120°$

where $[001]_{LCh}$ is parallel or antiparallel to $[100]_{Dj}$ in both cases. By comparing the lattice parameter measurements by Evans[60,61] for low chalcocite and djurleite ($Cu_{1.938}S$), the lattice misfit in the close-packed sulfur plane can be calculated as a function of interface orientation. Furthermore, by assuming a linear relationship between subcell volume and composition, the misfit between low chalcocite and djurleite, $Cu_{1.969}S$ can be estimated. Figure 5.9 shows the results of these calculations for planar interfaces which contain the c-axis of the sulfur sublattice (the misfit in the c-direction is ~0.3 percent for $Cu_{1.938}S$ and ~0.05 percent for $Cu_{1.969}S$). There is clearly a minimum in misfit for interfaces approximately perpendicular to $[010]_{LCh}$, if the orientation relationship is O.R. 60°. It was shown by Sands et al.[54] that the preferred low chalcocite-djurleite orientation relationship is O.R. 60° and that the minimum-misfit interface orientations are more frequently adopted than those which result in

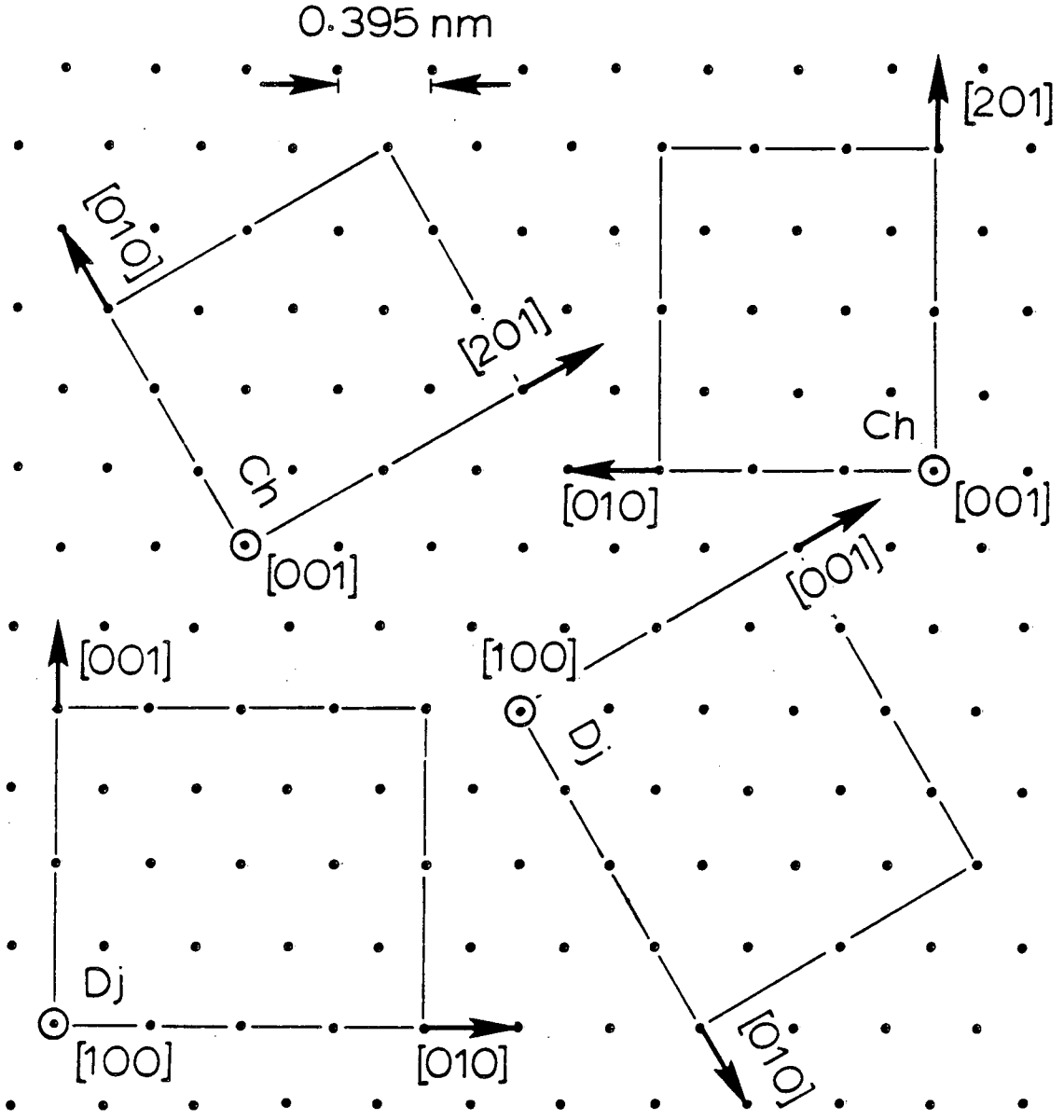

Fig. 5.8 Unit cells of low chalcocite and djurleite in basal plane projection. Two basic orientation relationships are indicated. Network of dots is sulfur sublattice.
XBL 843-1018

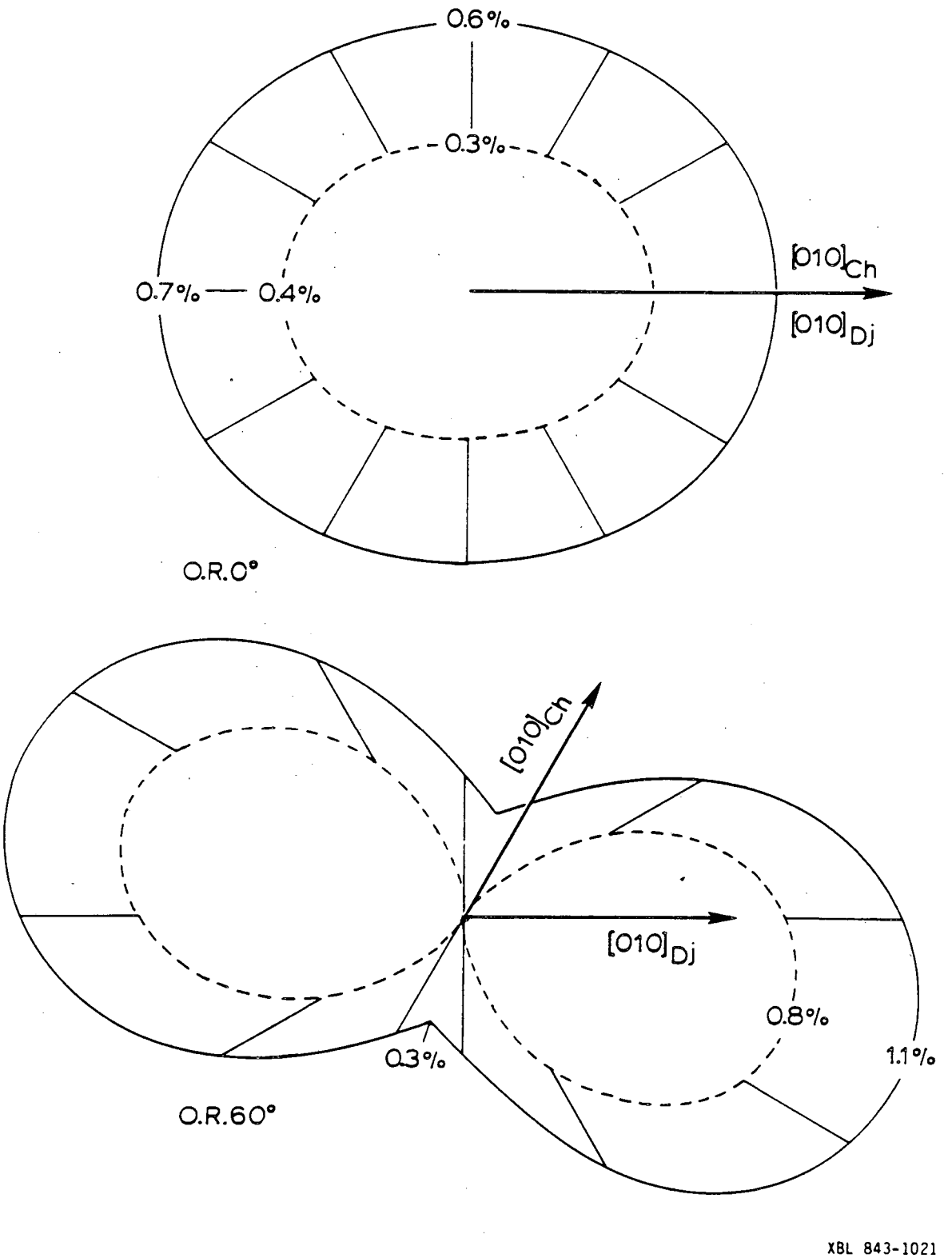

XBL 843-1021

Fig. 5.9 Lattice misfit in basal plane for low chalcocite-djurleite interfaces. Intersection of interface normal and misfit diagram gives percent misfit. Solid lines correspond to misfit between low chalcocite and djurleite, $Cu_{1.938}S$, calculated from lattice parameters measured by Evans.[60,62] Dashed lines correspond to estimated misfit between low chalcocite and djurleite, $Cu_{1.969}S$ (see text).

larger misfit. Figure 5.5 is consistent with these observations. The djurleite domain which has nucleated at a crack during room temperature aging is indeed the O.R. 60° variant and exhibits a flat interface in the minimum misfit orientation. Thus, lattice misfit considerations appear to dictate the shape and orientation relationship of djurleite domains in low chalcocite.

This analysis is reminiscent of the Wulff plot construction used to determine the equilibrium crystal shape[96] except that the surface energy is plotted as a function of orientation for the Wulff construction. To convert the lattice misfit to interfacial misfit energy one would need to account for the anisotropic elastic behavior of low chalcocite and djurleite. Additional contributions to the excess surface energy, such as copper-copper bonding irregularities at the interface, would also have to be considered.

While the above discussion explains the observed shapes and orientations of djurleite domains in low chalcocite, it does not address the specific atomic rearrangements which are required to transform low chalcocite into djurleite. In order to determine the relationship between these two structures, the atom positions of low chalcocite and djurleite ($Cu_{1.938}S$) as reported by Evans[60,62] were examined in an effort to reveal structural units. Low chalcocite was found to consist of alternating rows of $Cu_{12}S_6$ units. The arrangement of these units is diagrammed in Fig. 5.10. Djurleite ($Cu_{1.938}S$) is considerably more complicated. However, orderly $Cu_{20}S_{12}$ units were found at the body center and corner of the unit

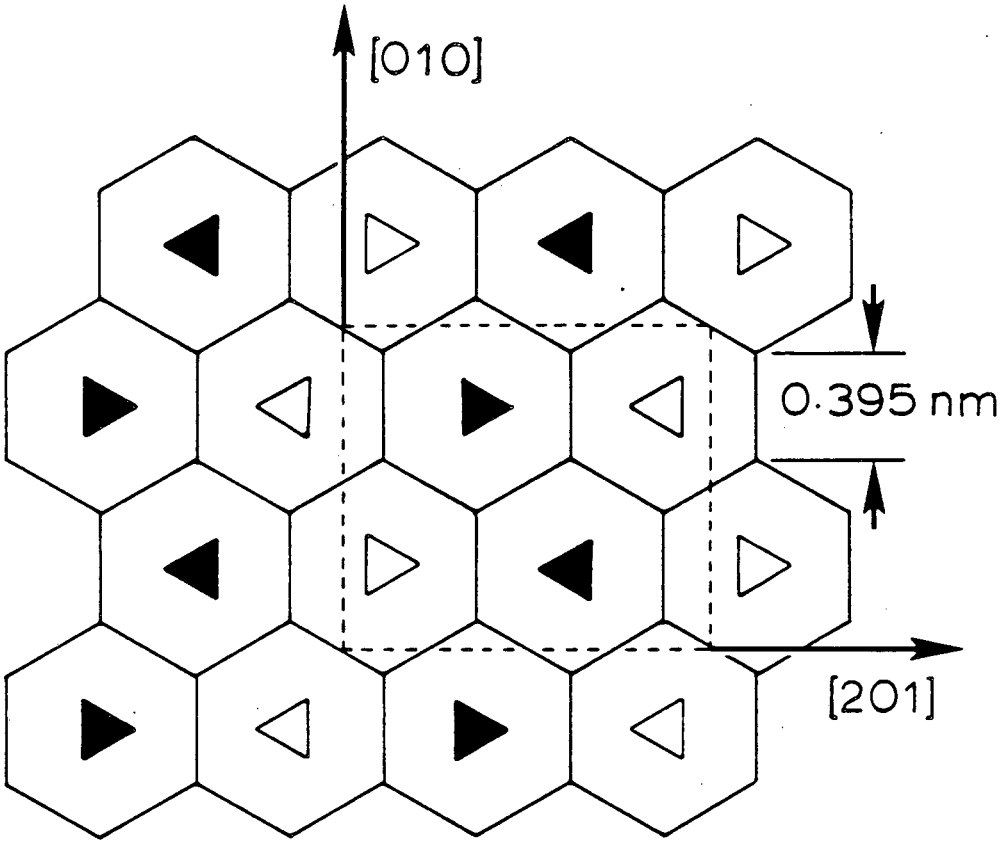

XBL 843-1019

Fig. 5.10 Arrangement of $Cu_{12}S_6$ building units in low chalcocite. Closed triangles represent five-copper layers of $Cu_{12}S_6$ units in plane. Open triangles represent five-copper layers of $Cu_{12}S_6$ units above plane (0.34 nm in [001] direction). Triangles pointing to right (left) indicate that remainder of unit is above (below) five-copper layer.

cell. The $Cu_{20}S_{12}$ unit resembles two low chalcocite $Cu_{12}S_6$ building units placed base-to-base except that, whereas each $Cu_{12}S_6$ unit has a base of five copper ions, the $Cu_{20}S_{12}$ unit cell has a center layer of six copper ions. Thus, the $Cu_{20}S_{12}$ unit of djurleite can be interpreted as a cluster of four copper vacancies. The two clusters per unit cell account for all of the copper vacancies in $Cu_{1.938}S$.

The solid-solution range of djurleite was measured by Potter[25] to be $1.965 > Cu:S > 1.934$. Evans[61,62,71] in analyzing his x-ray results suggested that the copper rich form of djurleite may be $Cu_{1.969}S$. The composition $Cu_{1.969}S$ could be obtained by adding one copper atom to the asymmetric unit of $Cu_{1.938}S$ (or 4 copper atoms to the unit cell). Evans was unable to locate the position of the extra copper atom. However, the analysis in terms of clusters suggests that djurleite, $Cu_{1.969}S$, may contain only one $Cu_{20}S_{12}$ unit per unit cell.

In terms of the cluster model, the low chalcocite to djurleite, $Cu_{1.969}S$, transformation can be described as follows. The djurleite structure can be derived from the low chalcocite structure by the clustering of copper vacancies into $Cu_{20}S_{12}$ units which simultaneously order into the periodic framework of djurleite, $Cu_{1.969}S$. This transformation is diagrammed schematically in Fig. 5.11. Compositions between $Cu_{1.938}S$ and $Cu_{1.969}S$ can be achieved by further clustering of copper vacancies to form $Cu_{20}S_{12}$ units in

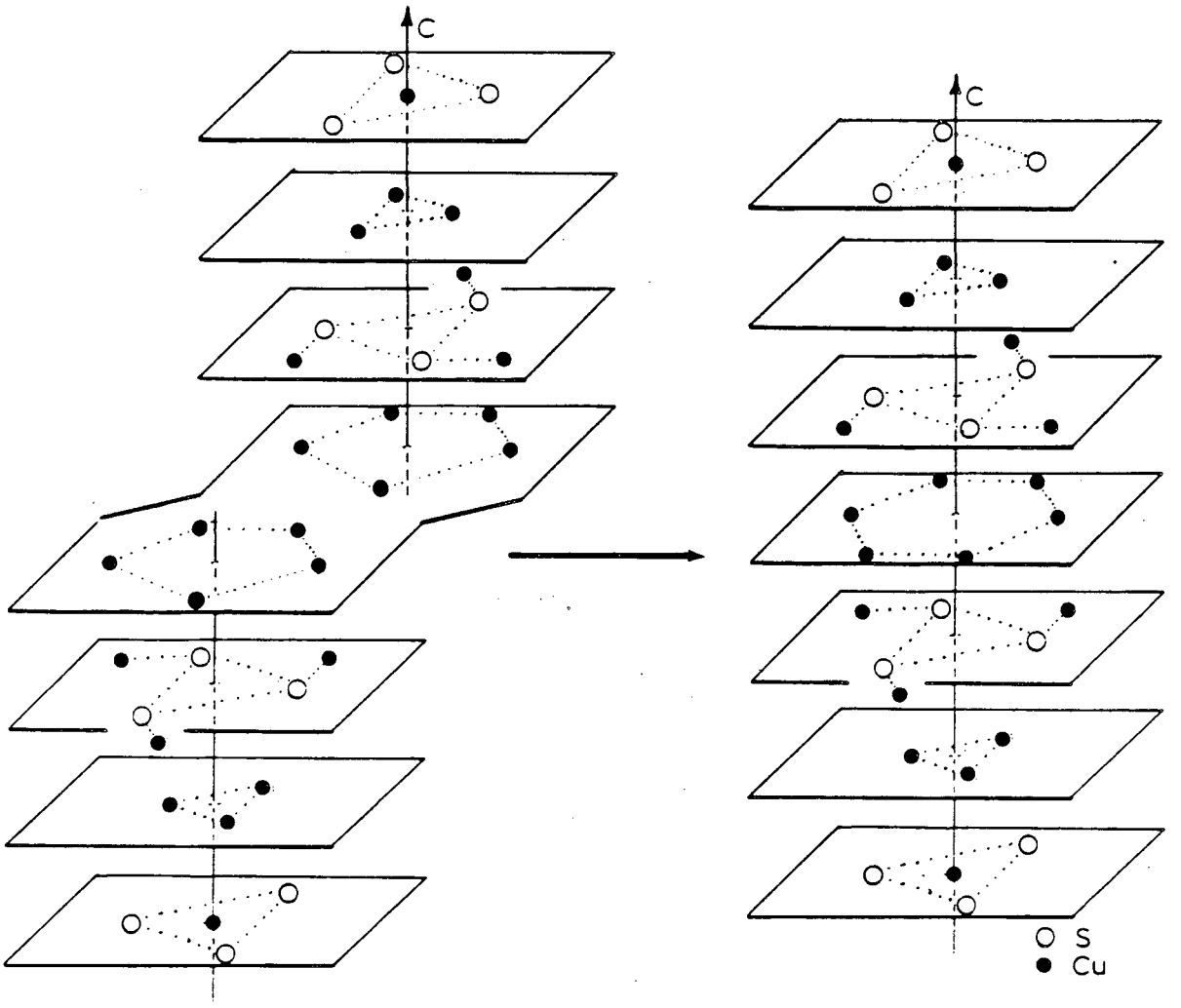

$$2\ Cu_{12}S_6 \longrightarrow Cu_{20}S_{12} + 4\ Cu \downarrow$$

2 Chalcocite Building Units — Djurleite 4-Vacancy Cluster

XBL 829-11379

Fig. 5.11 Schematic illustration of low chalcocite-to-djurleite transformation. Two low chalcocite $Cu_{12}S_6$ units rearrange to form $Cu_{20}S_{12}$ unit of djurleite plus four Cu.

the body-centered sites. The low activation energy for copper ion migration[78] allows these rearrangements to occur in a reasonable time at temperatures as low as 20°C.

5.4.2 The Djurleite-to-Low Digenite Transformation.

Unlike the low chalcocite-to-djurleite transformation, the djurleite-to-low digenite transformation involves extensive rearrangement of the sulfur sublattice (passage of Shockley partial dislocations on every other close-packed sulfur plane). Therefore, the djurleite-to-low digenite transformation should proceed slowly at room temperature. This may explain the observation of metastable copper-deficient phases based upon h.c.p. sulfur sublattices.[25]

6. SUMMARY

The principal findings of this study are summarized below.

1. The first XHRTEM images of the $Cu_{2-x}S$/CdS heterojunction have revealed the presence of the tetragonal phase, a high-pressure polymorph of low chalcocite. This is the first reported observation of the tetragonal phase in $Cu_{2-x}S$ layers prepared by the aqueous ion-exchange method.

2. The XHRTEM images show that the tetragonal phase-CdS interfacial habit plane is within ~30° of the CdS basal plane and that the close-packed sulfur planes of CdS are parallel to a set of the close-packed sulfur planes of the tetragonal phase (~f.c.c. sublattice). Off-basal interfaces are accommodated by ledges and basal terraces.

3. These images also show that the low chalcocite-CdS interfaces are steeply inclined to the basal plane, except during the very early stages of growth in basal facets.

4. The observed interfacial habit planes are consistent with the minimization of lattice misfit and with the compatibility of the f.c.c. and h.c.p. sulfur networks in the basal plane.

5. By considering lattice misfit, the structural compatibility of the sulfur networks, and the surface nucleation of h.c.p.-to-f.c.c. transformation dislocations, the observed $Cu_{2-x}S$/CdS morphologies as a function of local surface orientation can be understood.

6. Low temperature degradation of low chalcocite films has been shown to proceed by the nucleation of the 60° variant of djurleite. Lattice mismatch considerations appear to determine the shape and variant of the djurleite domains.

7. The low chalcocite-to-djurleite transformation can be modeled as the clustering of copper vacancies into $Cu_{20}S_{12}$ units and the simultaneous ordering of these units into the superstructure of djurleite. This transformation involves only the highly mobile copper ions.

8. The djurleite-to-low digenite ($6a_0$) transformation proceeds by the passage of Shockley partial dislocations on every other close-packed sulfur plane. Djurleite-low digenite interfaces are basal and coherent.

9. Heat treatment of $Cu_{2-x}S$/CdS heterojunctions in air at 150°C results in the formation of cuprite ($Cu_{2-x}O$) particles 5 to 10 nm in diameter on the $Cu_{2-x}S$ surface. Even after 45 minutes in air at 150°C, only the copper-rich phases, low chalcocite and the tetragonal phase, are detected.

10. The effects of ion-exchange bath temperature on $Cu_{2-x}S$ stoichiometry have been confirmed. Conversion of CdS to $Cu_{2-x}S$ at 65°C results in djurleite films, whereas conversion at 99°C produces low chalcocite and the tetragonal phase. The effects of thermal inertia are similar.

7. CONCLUSION

The $Cu_{2-x}S$/CdS interface morphology and the phase distribution in the $Cu_{2-x}S$ absorber have been determined. Thus, quantities that depend on the local surface orientation, such as the density of unsatisfied bonds and the interface area, can be estimated. These results will allow more accurate modeling of $Cu_{2-x}S$/CdS device characteristics. In addition, a determination of the optical and electronic properties of the tetragonal phase would yield a more refined description of the $Cu_{2-x}S$/CdS band diagram.

It is hoped that the results of this study will provide a basis for understanding the wide variations in reported cell behavior due to the effects of surface texture, heat treatment and long-term exposure, so that the $Cu_{2-x}S$/CdS device may be improved.

8. SUGGESTIONS FOR FUTURE WORK

A systematic study of the effects of heat treatment temperature and atmosphere on the structure and device characteristics of single-crystal $Cu_{2-x}S$/CdS heterojunctions would be of both fundamental and practical interest. The TEM specimen preparation techniques described in Section 3.2 should make such a study possible.

The relationship between heterojunction morphology and local surface orientation could be further explored by extending the study to include copper sulfide films formed in $Cd_yZn_{1-y}S$ substrates. Again this work would be of practical interest since ZnS is often alloyed with CdS to reduce both the lattice mismatch in the basal plane and the magnitude of the conduction band jump due to the difference in electron affinity between CdS and $Cu_{2-x}S$.

Finally, as mentioned in the conclusion, determination of the optical and electronic properties of the tetragonal phase is of the utmost importance.

ACKNOWLEDGEMENTS

This work would not have been possible without the support, encouragement and scientific guidance of my research supervisors, Professor Jack Washburn and Professor Ron Gronsky. Furthermore, this work could not have been completed in four years without the expert secretarial and administrative support of Kathy Brusse, Madeline Moore and Diana Morris. I also wish to express my gratitude to the technical and scientific staff of the National Center for Electron Microscopy. In particular, I would like to thank Dave Ackland for keeping the microscopes in excellent working order and Dr. Uli Dahmen for many fruitful discussions throughout the course of this work. Many thanks also go to Professor Alan Portis for reading both my M.S. and Ph.D. theses and for serving on my exam committee.

And for making my stay at Berkeley a memorable one, I would like to thank my friends in the "Amorphous Layer" softball team and in the Gronsky and Washburn research groups. Special thanks go to my office mates, Dr. Devendra Sadana, R'Sue Caron, Anthony Yu, and Jurek Mazur, for invigorating lunchtime conversations on everything from politics to science (and the politics of science).

And most of all, I wish to thank my wife, Laura, for her patience and (among other things) her efforts to remind me that there is much more to life than a weekly microscope session.

This work was supported by the Director, Office of Energy Research, Office of Basic Energy Sciences of the U.S. Department of Energy under Contract No. DE-AC03-76SF00098.

10. APPENDICES

10.1 Electron Diffraction of CdS and the $Cu_{2-x}S$ Phases ($x < 0.25$)

For the convenience of future investigators of the Cd-Cu-S system, the indexed diffraction patterns of cadmium sulfide (wurtzite) and the copper sulfide phases (Cu : S > 1.75) are assembled in this section. The three most prominent zone axes, corresponding to the [0001], $[01\bar{1}0]$, and $[\bar{2}110]$ zone axes of CdS, have been chosen. Open circles correspond to kinematically forbidden reflections.

Table 10.1 Key to Patterns in Fig. 10.1

	Phase	Zone Axis	hkl No. 1 (nm^{-1})	hkl No. 2 (nm^{-1})	Comments
a.	CdS	[0001]	$0\bar{1}10$ (2.79)	$\bar{2}110$ (4.83)	
a.	high chalcocite	[0001]	$0\bar{1}10$ (2.92)	$\bar{2}110$ (5.06)	
b.	low chalcocite	[001]	$\bar{4}00$ (2.93)	060 (5.04)	streaks due to faulting on (200)
c.	djurleite $Cu_{1.938}S$	[100]	004 (2.95)	080 (5.08)	
d.	$4a_h x 2c_h$ phase	[0001]	$0\bar{4}40$ (2.97)	$\bar{8}440$ (5.16)	pseudohexagonal (ref. 48)
e.	$2a_h x c_h$ phase	[0001]	$0\bar{2}20$	$\bar{4}220$	

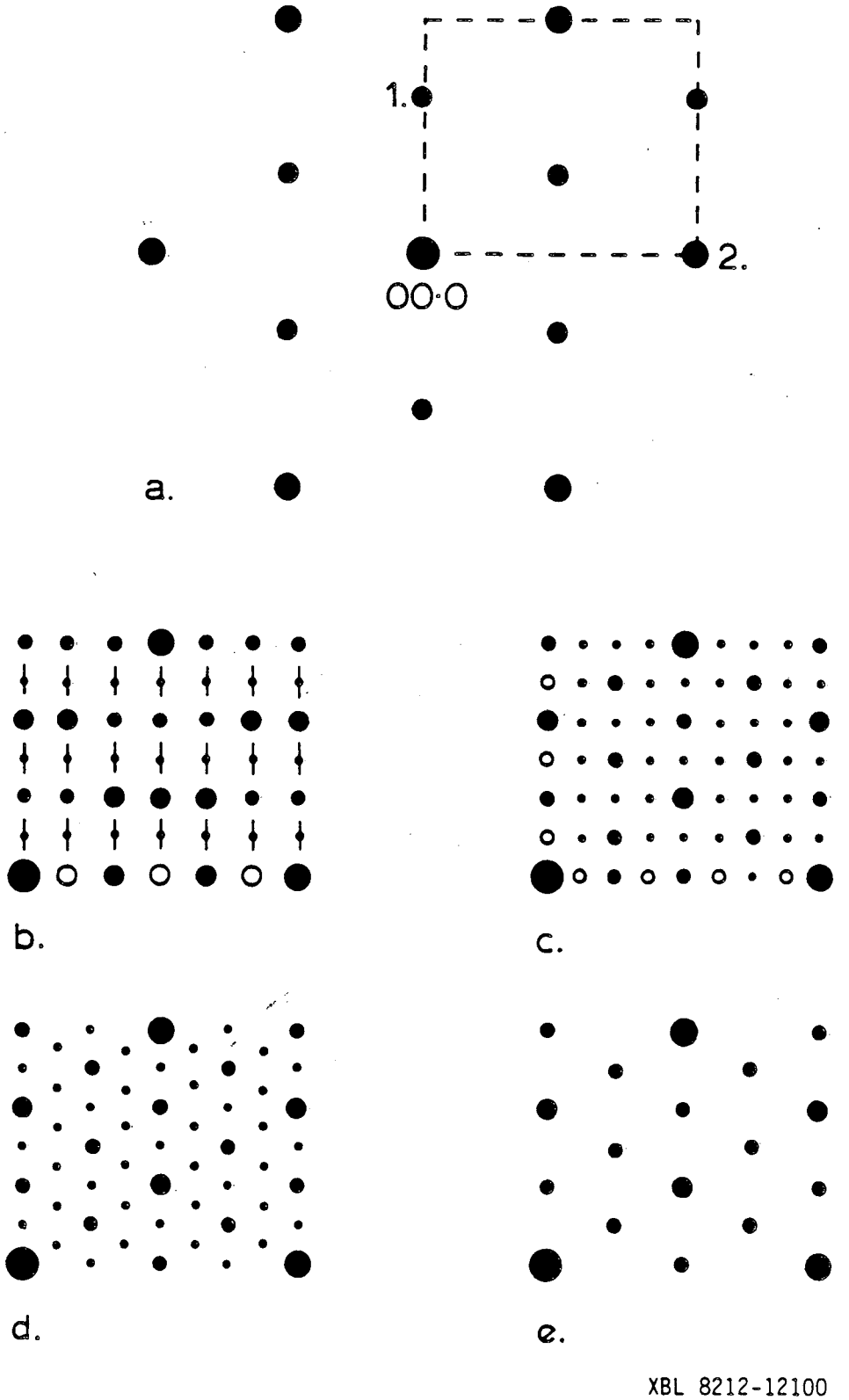

Fig. 10.1 Diffraction patterns of CdS and $Cu_{2-x}S$ phases with h.c.p. sulfur networks in [0001] zone-axis orientation.

Table 10.2 Key to Patterns in Fig. 10.2

	Phase	Zone Axis	hkl No. 1 (nm^{-1})	hkl No. 2 (nm^{-1})	Comments
a.	high digenite	$[1\bar{1}1]$	$\bar{2}\bar{2}0$ (5.09)	$\bar{1}12$ (4.41)	
a.	low digenite $5a_o$	$[1\bar{1}1]$	$\bar{1}0\ \bar{1}0\ 0$ (5.11)	$\bar{5}\ 5\ 10$ (4.42)	no strong superstructure spots in this pattern
b.	anilite	$[20\bar{1}]$	040 (5.10)	$\bar{2}0\bar{4}$ (4.43)	space group Pnma (ref. 97)
c.	anilite	[021]	$\bar{4}00$ (5.07)	024 (4.44)	
d.	tetragonal phase	$[40\bar{1}]$	020 (4.99)	$\bar{1}0\bar{4}$ (4.34)	

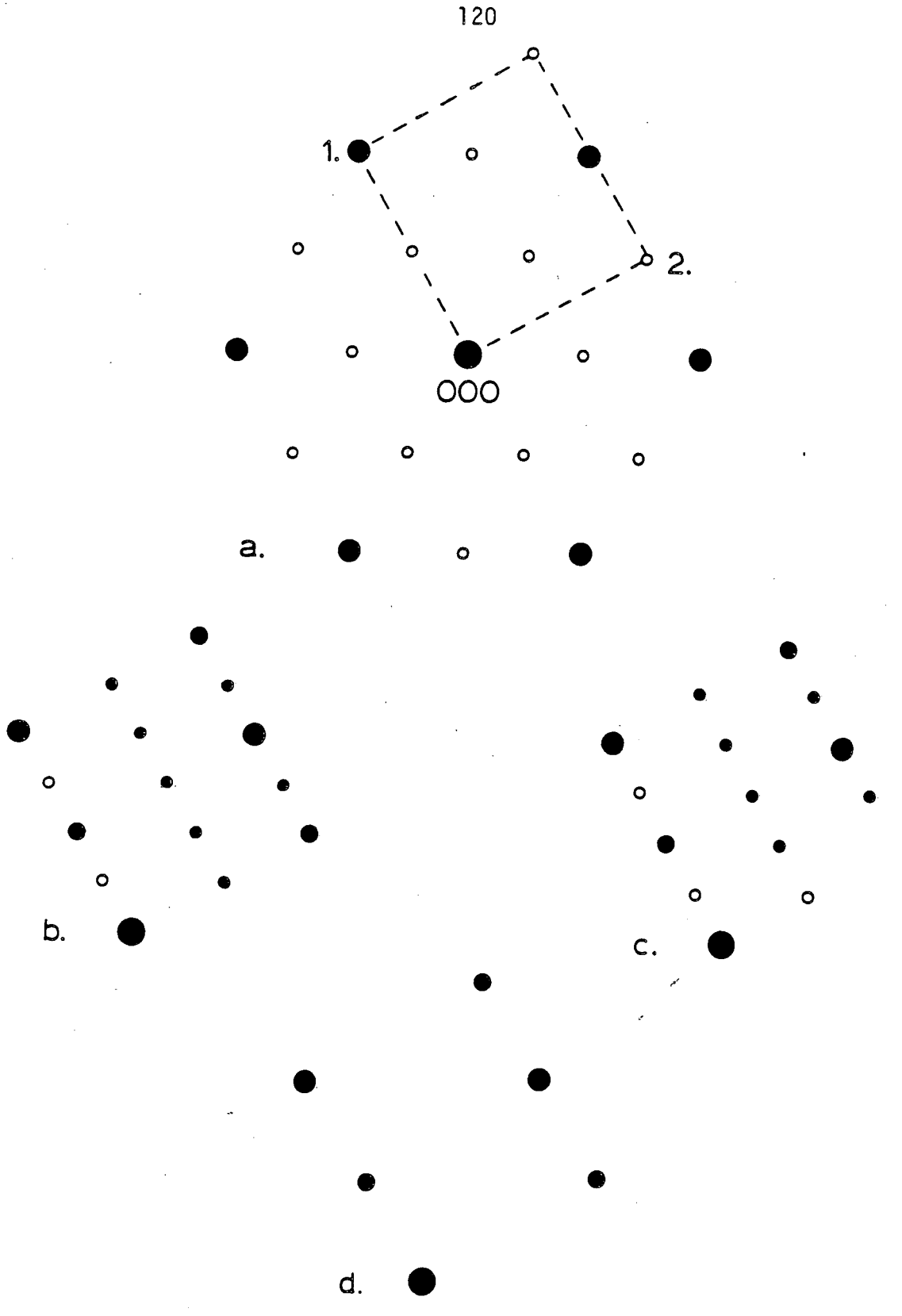

XBL 8212-12104

Fig. 10.2 Diffraction patterns of $Cu_{2-x}S$ phases with f.c.c. sulfur networks in $[1\bar{1}1]$ zone-axis orientation.

Table 10.3 Key to Patterns in Fig. 10.3

	Phase	Zone Axis	hkl No. 1 (nm^{-1})	hkl No. 2 (nm^{-1})
a.	CdS	$[01\bar{1}0]$	0002 (2.98)	$\bar{2}110$ (4.83)
a.	high chalcocite	$[01\bar{1}0]$	0002 (2.98)	$\bar{2}110$ (5.06)
b.	low chalcocite	$[20\bar{1}]$	$\bar{2}04$ (2.96)	060 (5.05)
c.	low chalcocite	[241]	$\bar{2}04$ (2.96)	$\bar{6}30$ (5.07)
d.	djurleite $Cu_{1.938}S$	[001]	800 (2.97)	$0\bar{8}0$ (5.08)
e.	djurleite $Cu_{1.938}S$	$[03\bar{2}]$	800 (2.97)	046 (5.10)
f.	$4a_h x 2c_h$ phase	$[01\bar{1}0]$	0004 (2.99)	$\bar{8}440$ (5.16)
g.	$2a_h x c_h$ phase	$[01\bar{1}0]$	0002	$\bar{4}220$

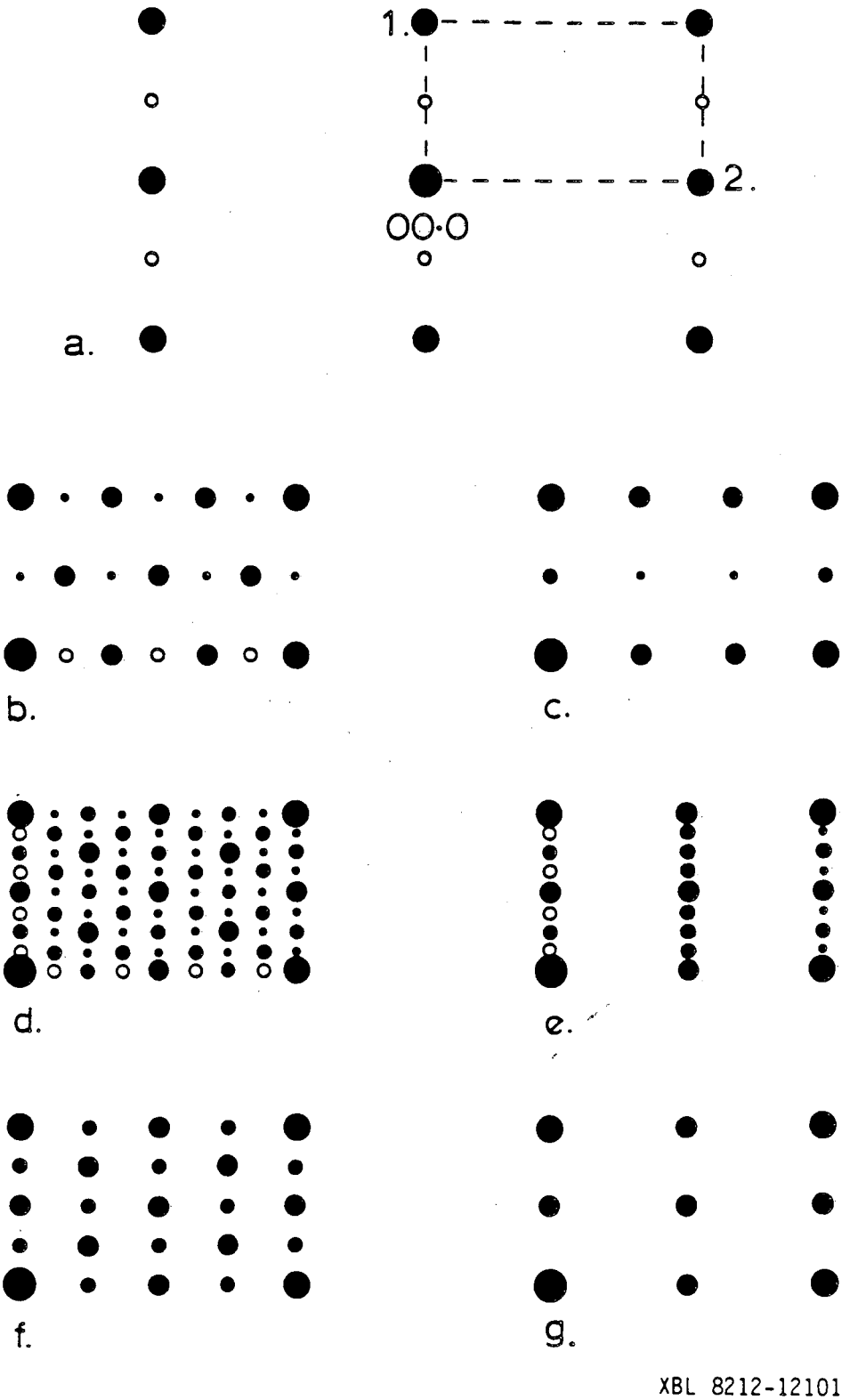

Fig. 10.3 Diffraction patterns of CdS and $Cu_{2-x}S$ phases with h.c.p. sulfur networks in [0110] zone-axis orientation.

Table 10.4 Key to Patterns in Fig. 10.4

	Phase	Zone Axis	hkl No. 1 (nm^{-1})	hkl No. 2 (nm^{-1})
a.	high digenite	[112]	$11\bar{1}$ (3.12)	$2\bar{2}0$ (5.09)
b.	anilite	$[10\bar{1}]$	202 (3.12)	040 (5.10)
b.	anilite	[011]	$0\bar{2}2$ (3.13)	$\bar{4}00$ (5.07)
c.	anilite	$[\bar{1}31]$	202 (3.12)	$\bar{2}\bar{2}4$ (5.11)
c.	anilite	$[3\bar{1}\bar{1}]$	$0\bar{2}2$ (3.13)	224 (5.11)
d.	anilite	$[3\bar{1}1]$	022 (3.13)	$22\bar{4}$ (5.11)
e.	tetragonal phase	$[20\bar{1}]$	102 (3.06)	020 (4.99)
f.	tetragonal phase	$[\bar{2}61]$	102 (3.06)	$\bar{1}\bar{1}4$ (5.01)
g.	low digenite $5a_o$ (also $6a_o$)	[112]	$55\bar{5}$ (3.13)	$10\ \bar{1}\bar{0}\ 0$ (5.11)

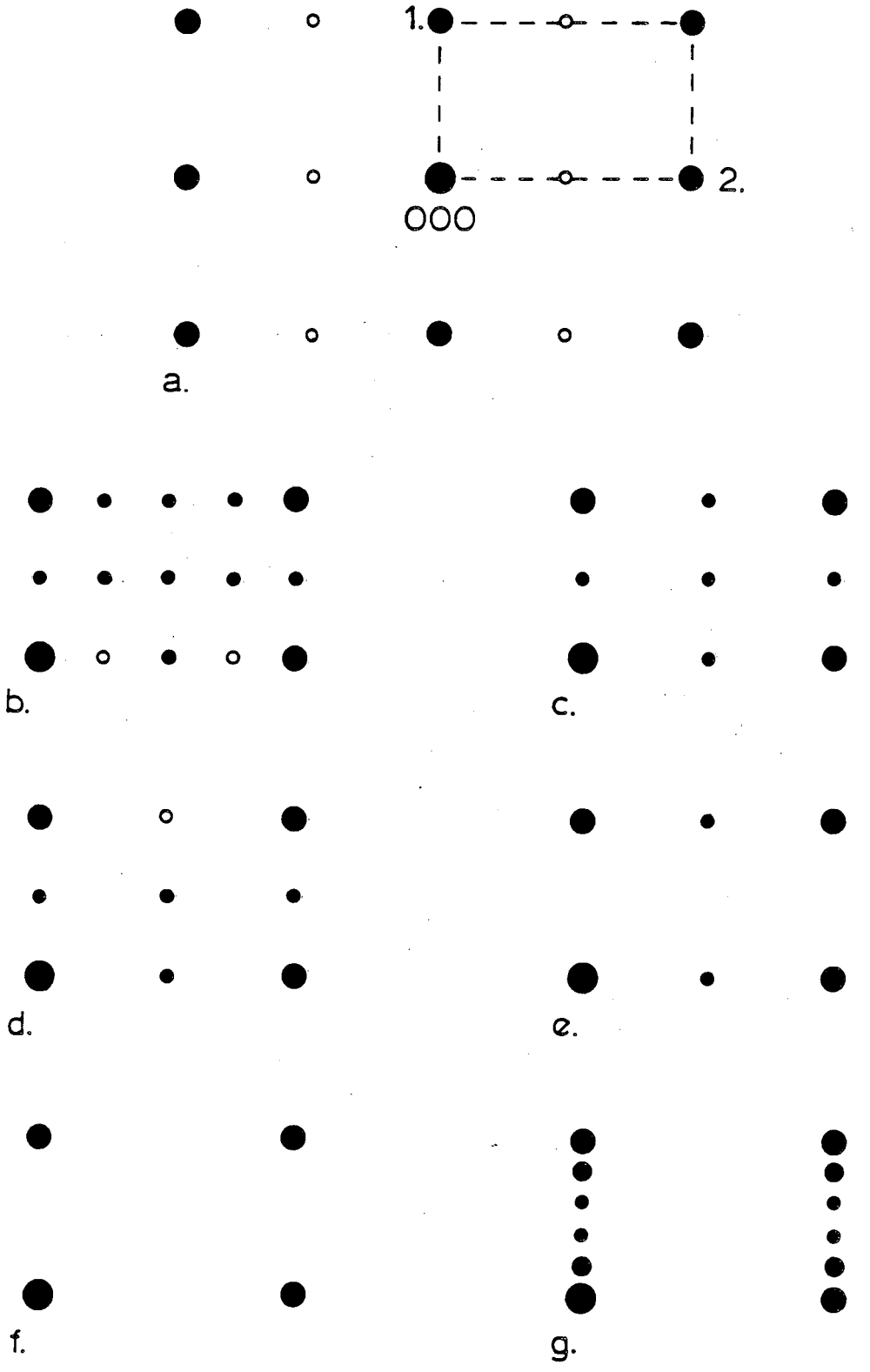

XBL 8212-12102

Fig. 10.4 Diffraction patterns of $Cu_{2-x}S$ phases with f.c.c. sulfur networks in [112] zone-axis orientation.

Table 10.5 Key to Patterns in Fig. 10.5

	Phase	Zone Axis	hkl No. 1 (nm^{-1})	hkl No. 2 (nm^{-1})
a.	CdS	$[\bar{2}110]$	0002 (2.98)	$0\bar{1}10$ (2.79)
a.	high chalcocite	$[\bar{2}110]$	0002 (2.98)	$0\bar{1}10$ (2.92)
b.	low chalcocite	[010]	$\bar{2}04$ (2.96)	$\bar{4}00$ (2.92)
c.	low chalcocite	$[6\bar{4}3]$	$\bar{2}04$ (2.96)	230 (2.91)
d.	djurleite $Cu_{1.938}S$	[010]	800 (2.97)	004 (2.95)
e.	djurleite $Cu_{1.938}S$	[012]	800 (2.97)	$0\bar{4}2$ (2.94)
f.	$4a_h \times 2c_h$ phase	$[\bar{2}110]$	0004 (2.99)	$0\bar{4}40$ (2.98)
g.	$2a_h \times c_h$ phase	$[\bar{2}110]$	0002	$0\bar{2}20$

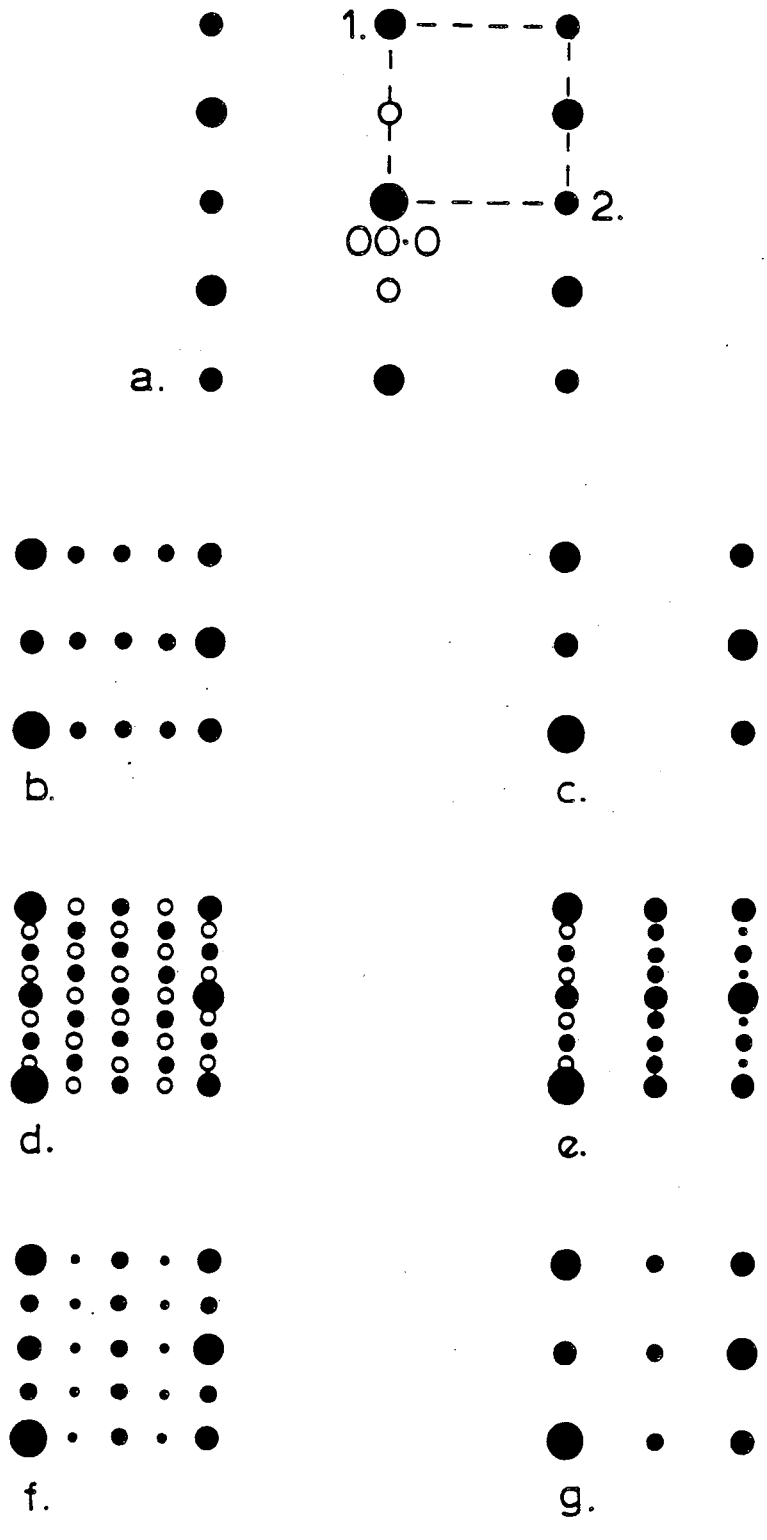

XBL 8212-12103

Fig. 10.5 Diffraction patterns of CdS and $Cu_{2-x}S$ phases with h.c.p. sulfur networks in $[\bar{2}110]$ zone-axis orientation.

Table 10.6 Key to Patterns in Fig. 10.6

	Phase	Zone Axis	hkl No. 1 (nm^{-1})	hkl No. 2 (nm^{-1})
a.	high digenite	$[\bar{1}10]$	002 (3.60)	$\bar{2}\bar{2}0$ (5.09)
b.	anilite	[111]	$2\bar{2}0$ (3.60)	$\bar{2}\bar{2}4$ (5.11)
c.	anilite	[010]	004 (3.63)	$\bar{4}00$ (5.07)
d.	anilite	[100]	004 (3.63)	040 (5.10)
e.	tetragonal phase	[221]	$1\bar{1}0$ (3.52)	$\bar{1}\bar{1}4$ (5.01)
f.	tetragonal phase	[010]	004 (3.55)	$\bar{2}00$ (4.99)
g.	low digenite $5a_o$ (also $6a_o$)	$[\bar{1}10]$	00 10 (3.61)	$\overline{10}$ $\overline{10}$ 0 (5.11)

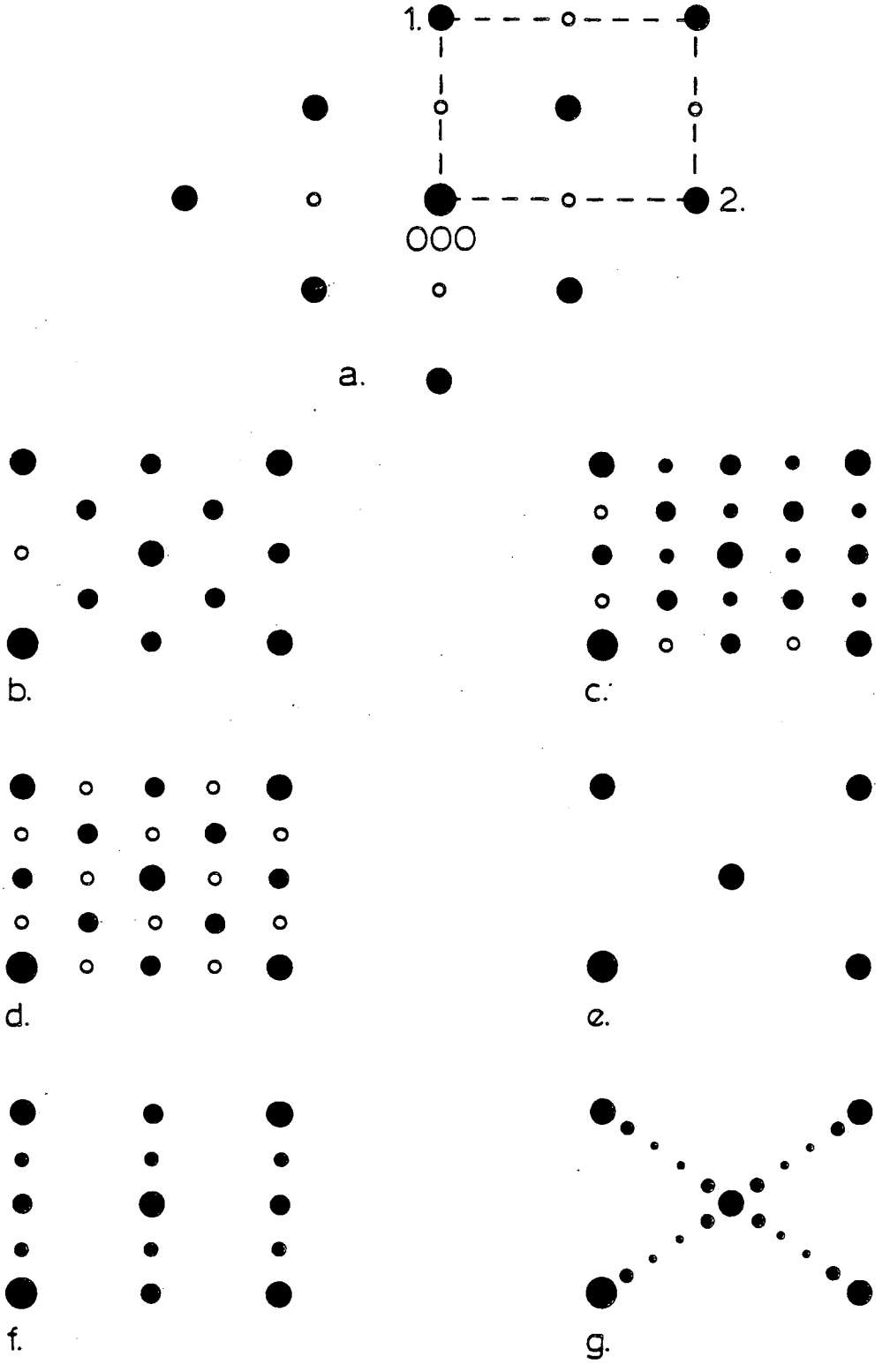

Fig. 10.6 Diffraction patterns of $Cu_{2-x}S$ phases with f.c.c. sulfur networks in $[\bar{1}10]$ zone-axis orientation.

10.2 The Domain Structure of Low Chalcocite

The conversion of CdS to chalcocite and the order-disorder transition in chalcocite result in low chalcocite domain structures with both translation ("antiphase") and orientation ("twin") boundaries. It is generally accepted that the "wet" conversion of CdS to low chalcocite involves the substitution of two Cu^{+} ions for every Cd^{+2} ion, leaving the hexagonal close-packed sulfur substructure essentially intact. Similarly, the order-disorder transition in chalcocite does not involve the sulfur ions to an appreciable degree, the copper ions being in an almost fluid state above the transition temperature (90° to 104°C).[69]

The low chalcocite obtained by both methods has monoclinic space group $P2_1/c$. the lattice of low chalcocite is approximately pseudo-orthorhombic as shown in Fig. 2.3. Ignoring the small distortions of the low temperature sulfur substructure (pseudo-orthorhombic β = 90.08°). The theory genralized by Guymont, Gratias, Portier, and Fayard[98] can be applied to predict the number and type of variants possible in low chalcocite produced by either the cooling of high chalcocite or the low temperature conversion of CdS.

10.2.1 Theory.

The pertinent theory as presented in reference 98 will be summarized below.

The space group of the high temperature phase, G_s, is made up of symmetry elements g_i.

$$G_s = \{g_1, g_2, \ldots, g_m\}$$

with $g_i = (R_i/\tau_i)$

where R_i denotes the orientation component of g_i and τ_i denotes the translation component. A particular g_i can be represented explicitly in Seitz' notation. For example; (1/000) represents the identity operation, $(c_{[1\bar{1}0]}/00\ 1/2)$ reflection through a glide mirror c containing the origin and located in a $(1\bar{1}0)$ plane, $(\bar{1}/110)$ inversion through the position 1/2 1/2 0 $(6^1_{3[001]}/00\ 1/2)$ $\pi/3$ rotation about [001] followed by a 00 1/2 translation.

In the following, H_s, the space group of the low temperature phase, is assumed to be a subgroup of G_s (i.e., G_s contains all of the symmetry elements of H_s and more).

The boundary between each pair of domains in the low temperature phase is characterized by one of the symmetry elements of G_s which was lost on transition to H_s.

Therefore, each boundary has associated with it a "coset" which is the product of the element g (which was lost in the transition) with the space group, H_s, of the low temperature phase. The space group G_s can be decomposed into cosets with respect to H_s by employing the following properties of cosets:

i) Any two cosets of the same decomposition have no common operator.

ii) Any two operators belonging to the same coset are distinct.

iii) Every operator of G_s belongs to one and only one coset.

The number of variants generated by the G_s to H_s transition equals the number of different gH_s cosets contained in G_s plus one, the coset of the reference variant, $(1/000)H_s$. The decomposition can be written as

$$G_s = \bigcup_{i=1}^{n-1} g_i H_s + H_s$$

where n is the "index" of H_s into G_s. This index, n, is a product of the "translation index" and the "point group index." The translation index is the ratio of the number of lattice nodes of G_s to the number of lattice nodes of H_s in their smallest common unit cell. Similarly, the point group index is the ratio of the number of symmetry elements in the point group of G_s to the number of symmetry elements in the point group of H_s. Therefore, the total number of possible variants in the low temperature phase is equal to n, whereas the number of possible boundaries is equal to n-1 (note that this theory yields no direct information concerning the structure of the boundary region).

In the general case there are pure translation boundaries, pure orientation boundaries, mixed "translation-twin" boundaries (associated with the loss of a screw axis or glide plane), and combinations of the above so that G_s can be written

$$G_s = (H_s + \bigcup_{i=1}^{n-1} g_i H_s) + (1/\tau_1)\,(H_s + \bigcup_{i=1}^{n-1} g_i H_s) + \ldots +$$

$$(1/\tau_{p-1})\,(H_s + \bigcup_{i=1}^{n-1} g_i H_s) \quad ,$$

where $(1/\tau_j)$, j=1,...,p-1, represent the p-1 possible pure translation boundaries.

10.2.2 Application to $P6_3/mmc(\underline{a},\underline{c}) \longrightarrow P2_1/c(2\sqrt{3}\underline{a}-\underline{c},3\underline{a},2\underline{c})$.

The translation index, n_t, for the high chalcocite to low chalcocite transition is equal to the volume ratio of the unit cells since they both have primitive lattices. Thus, $n_t = 24$. The point group index, n_p, is given by the ratio of the number of elements in 6/mmm to the number of elements in 2/m. Thus, $n_p = 24/4 = 6$. Therefore, n, the index of this transition is 24·6 = 144. In other words, there are 144 possible variants and 143 possible boundaries.

The 24 symmetry elements of $P6_3/mmc$ (referenced to the origin at $\bar{3}$m1; see Fig. 10.7) are listed in Table 10.7.

Talbe 10.7. Symmetry elements of $P6_3/mmc$

	equivalent positions	symmetry elements
1.	x,y,z	(1/000)
2.	$\bar{y}$,x-y,z	(3^1_2[001]/000)
3.	y-x,$\bar{x}$,z	(3^2[001]/000)
4.	$\bar{y}$,$\bar{x}$,z	($m_{[110]}$/000)
5.	x,x-y,z	($m_{[010]}$/000)
6.	y-x,y,z	($m_{[100}$/000)
7.	$\bar{x}$,$\bar{y}$,$\bar{z}$	($\bar{1}$/000)
8.	y,y-x,$\bar{z}$	($\bar{3}^1$ [001]/000)
9.	x-y,x,$\bar{z}$	($\bar{3}^2$ [001]/000)
10.	y,x,$\bar{z}$	($2_{[110]}$/000)
11.	$\bar{x}$,y-x,$\bar{z}$	($2_{[010]}$/000)
12.	x-y,$\bar{y}$,$\bar{z}$	($2_{[100]}$/000)
13.	$\bar{x}$,$\bar{y}$,1/2+z	(2_1 [001]/00 1/2)
14.	y,y-x,1/2+z	(6^5_3 [001]/100 1/2)
15.	x-y,x,1/2 + z	(6^1_3 [001]/100 1/2)
16.	x,y,1/2-z	($m_{[001]}$/100 1/2)
17.	$\bar{y}$,x-y,1/2-z	($\bar{6}^5$ [001]/100 1/2)
18.	y-x,$\bar{x}$,1/2-z	($\bar{6}^1$ [001]/100 1/2)
19.	y,x,1/2+z	(c [1$\bar{1}$0]/100 1/2)
20.	$\bar{x}$,y-x,1/2+z	(c [210]/100 1/2)
21.	x-y,$\bar{y}$,1/2+z	(c [120]/100 1/2)
22.	$\bar{y}$,$\bar{x}$,1/2-z	(2 [1$\bar{1}$0]/100 1/2)
23.	x,x-y,1/2-z	(2 [210]/100 1/2)
24.	y-x,y,1/2-z	($2_{[120]}$/100 1/2)

The symmetry elements of $P2_1/c$ referenced to the unit cell of $P6_3/mmc$ are given in Table 10.8.

Table 10.8 Symmetry elements of $P2_1/c$.

equivalent positions in monoclinic unit cell with origin at the inversion center of $P2_1/c$ (1/2 1/20 in $P6_3/mmc$ unit cell).	symmetry elements with reference to hexagonal unit cell.
1. x,y,z	(1/000)
2. $\bar{x},\bar{y},\bar{z}$	($\bar{1}$/110)
3. $\bar{x}$,1/2+y,1/2-z	(2 [110]/121)
4. x,1/2-y,1/2+z	(m [010]/021)

The following decomposition can now be made:

$\{P6_3/mmc\}\ (\underline{a},\underline{c}) =$ $\{P2_1/c\}\ (2\sqrt{3}\underline{a}-\underline{c},3\underline{a},2\underline{c})$
+ {(13), (16), (20), (23)}
+ {(2), (6), (8), (12)}
+ {(14), (17), (21), (24)}
+ {(3), (4), (9), (10)}
+ {(15), (18), (19), (22)}
+ multiplication of the above by each of the remaining 23 pure translation operators,

where the numbers in parentheses refer to the symmetry elements of Table 10.7. Using the convention suggested in reference 98, this expression can be simplified:

$\{P6_3/mmc\}\ (\underline{a},\underline{c}) =$ $\{P2_1/c\}\ (2\sqrt{3}\underline{a}-\underline{c},3\underline{a},2\underline{c})$
+ $(m_{[001]}/00\ 1/2)\{P2_1/c\}\ (2\sqrt{3}\underline{a}-\underline{c},3\underline{a},2\underline{c})$
+ $(m_{[100]}/000)\{P2_1/c\}\ (2\sqrt{3}\underline{a}-\underline{c},3\underline{a},2\underline{c})$
+ $(2_{[120]}/00\ 1/2)\{P2_1/c\}\ (2\sqrt{3}\underline{a}-\underline{c},3\underline{a},2\underline{c})$
+ $(m_{[110]}/000)\{P2_1/c\}\ (2\sqrt{3}\underline{a}-\underline{c},3\underline{a},2\underline{c})$
+ $(2_{[1\bar{1}0]}/00\ 1/2)\{P2_1/c\}\ (2\sqrt{3}\underline{a}-\underline{c},3\underline{a},2\underline{c})$
+ multiplication of the above by each of the remaining 23 pure translation operators.

Notice that this transition does not result in any translation-twin boundaries (the requirement for which is that the coset representing the boundary operation contain only screw axes or glide plane operators).

The six pure orientation variants and four of the 24 pure translation variants are diagrammed in Figure 10.7.

10.2.3 Summary of High Resolution Transmission Electron Miscrocopy Observations.

The decomposition of the high temperature space group into cosets relative to the low temperature space group has facilitated prediction of the possible boundaries in low chalcocite. However, this theory gives no information regarding the energetics of the various boundaries. The predominance of certain boundaries over others cannot be predicted without including specific information such as boundary orientation. Also, by neglecting small strains at the outset, effects which may, for instance, lead to microstructures consisting of small domains of each of the six orientation variants so as to relieve any long range strains (this is a common occurrence in as-plated films of djurleite, $Cu_{1.96}S$, formed on basal CdS substrates) have been ignored.

The following observations serve as a summary of the recent experimental progress in the study of boundaries in low chalcocite.

In low chalcocite films with normal [001] (formed by conversion of the basal faces of CdS single crystals), the dominant boundary is represented by the pure translation operator (1/210) (= $1/4[201]_{low\ ch.}$)

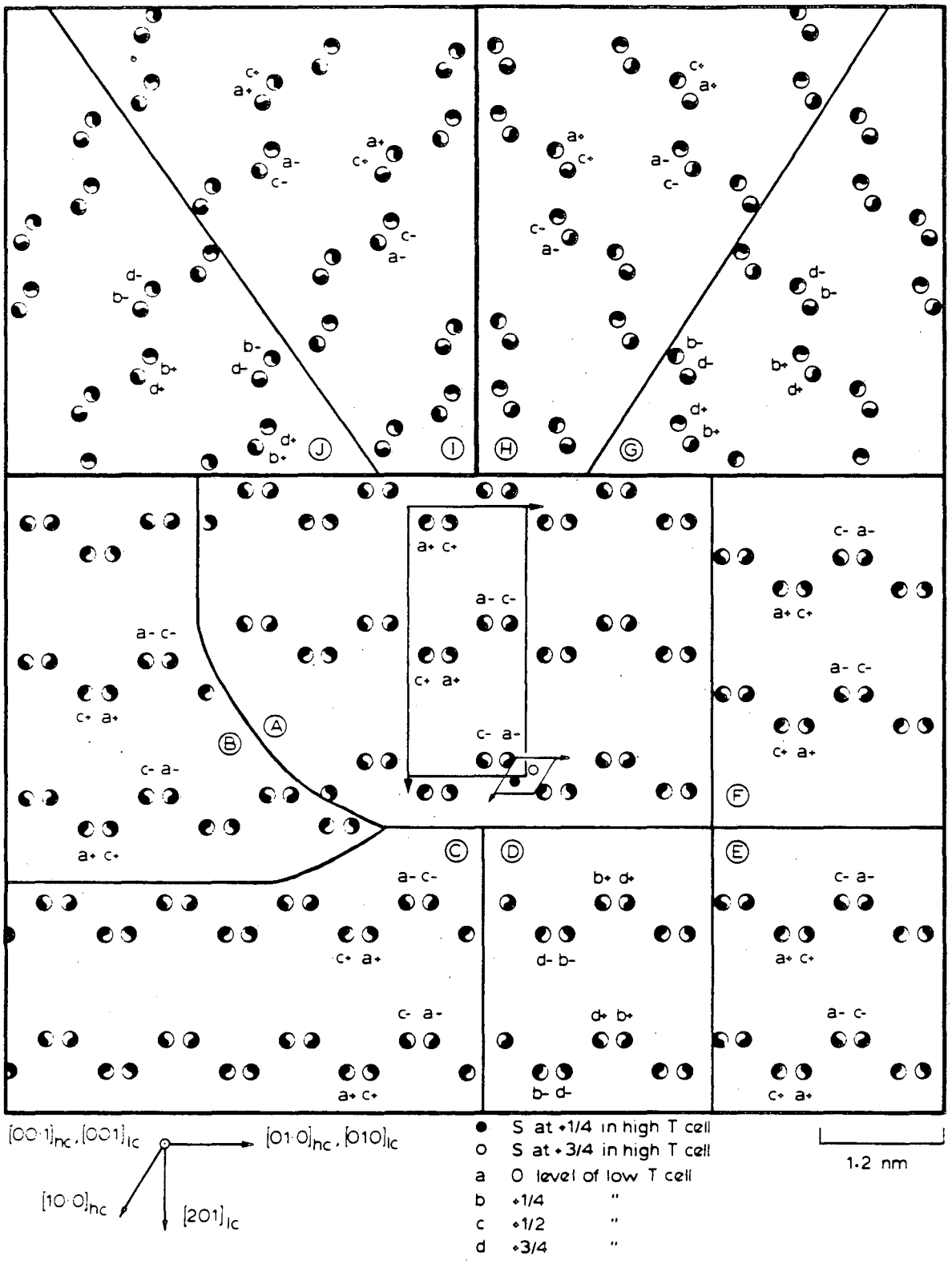

Fig. 10.7 Schematic diagram of orientation and translation variants in low chalcocite. A = (1/000), B = (1/110), C = (1/010), D = $(m_{[001]}/00\ 1/2)$, E = (1/001), F = (1/210), G = $(2_{[120]}/00\ 1/2)$, H = $(m_{[100]}/000)$, I = $(m_{[110]}/000)$, and J = $(2_{[1\bar{1}0]}/00\ 1/2)$. XBL 831-7587

These boundaries invariably lie on $(100)_{\text{low ch.}}$ (perpendicular to the boundary vector). Deviation from this plane has not yet been observed, even though these boundaries are extremely common (the average boundary separation if often less than 7.5 nm; see Fig. 10.8). Structural analysis of low chalcocite shows that these (1/210) boundaries may accommodate nonstoichiometry in $Cu_{2-x}S$ films.[54]

Basal films also contain (1/110)-type pure translation boundaries. These boundaries do not have a preferred habit plane and tend to wander. Also found are $(m_{[001]}/00\ 1/2)$ orientation boundaries which are difficult to observe by HRTEM unless they intersect another boundary (see Figure 10.9). The remaining orientation boundaries are observed infrequently in low chalcocite.

$Cu_{2-x}S$ films formed on CdS faces which contain the c-axis show markedly different domain structures. These $[010]_{\text{low ch.}}$ films contain high densities of wandering (1/110) translation boundaries. (1/110) boundaries are occasionally found to lie flat on the basal plane, indicating that they may be debris from the basal plane slip of sublattice dislocations (see Figure 10.10). These boundaries are found to interact with sublattice dislocations, usually resulting in either annihilation of the boundary or formation of a (1/210) boundary. Unlike the basal film case, these (1/210) boundaries wander until the boundary plane approaches $(100)_{\text{low ch.}}$. At an angle of approximately 60° to $(100)_{\text{low ch.}}$ plane, the boundary "snaps" into its rigid posture on (100) (see Figure 10.11).

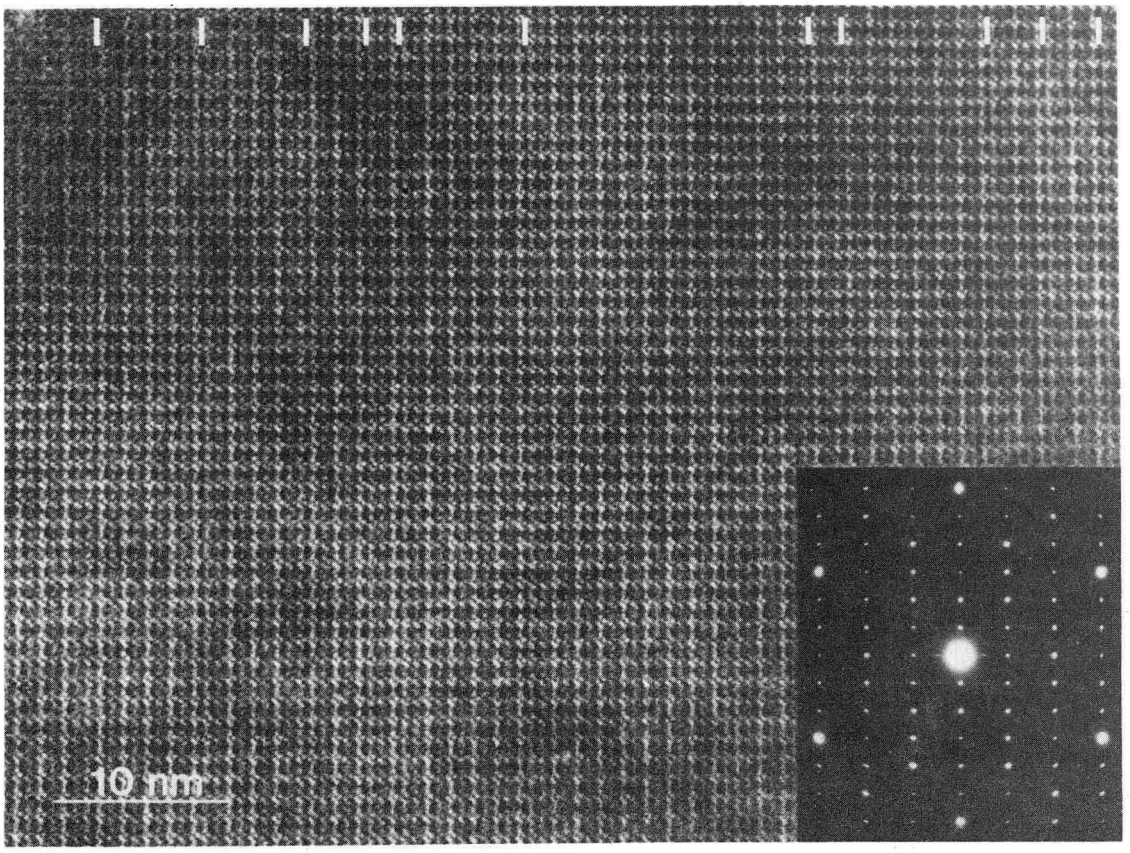

Fig. 10.8 HRTEM image of low chalcocite film with 1/4[201] translation boundaries (indicated by hash marks). Low chalcocite is in [001] zone-axis orientation. XBB 829-7600

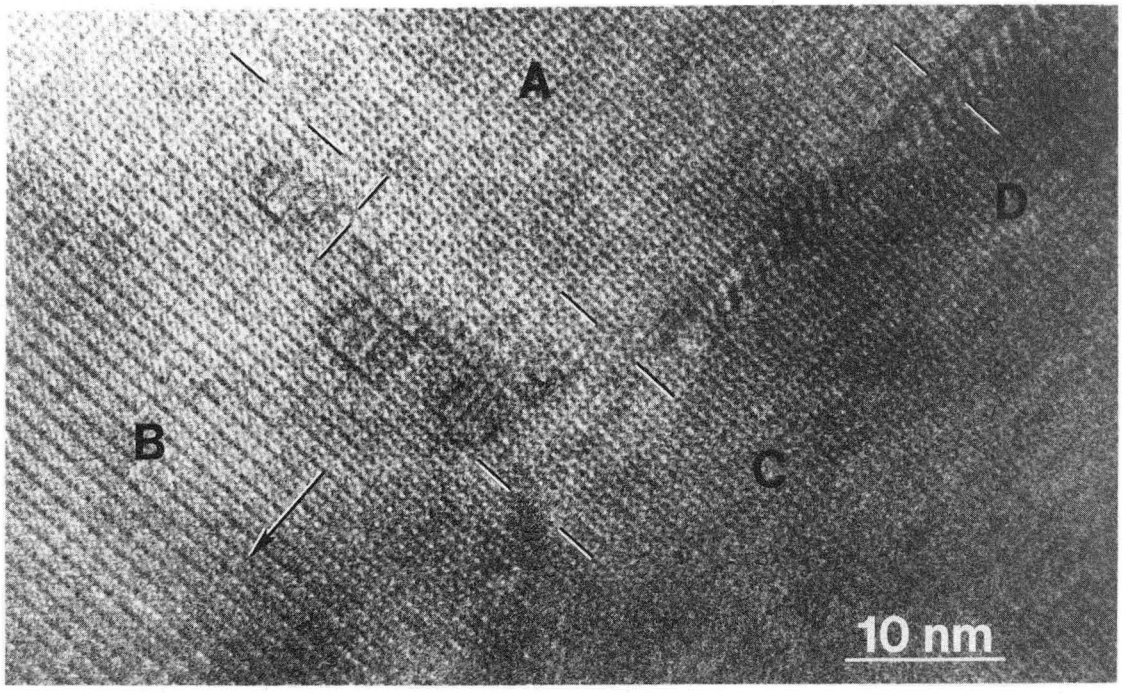

Fig. 10.9 HRTEM image of low chalcocite film in [001] zone-axis orientation with domain A as reference variant (1/000); B is (1/100), C is ($m_{[001]}$/00 1/2), and D is (1/0$\bar{1}$0) with reference to high temperature hexagonal subcell. Arrow indicates [010] direction of low chalcocite and hexagonal subcell. See Fig. 10.7 for schematic diagram.
XBB 820-10000A

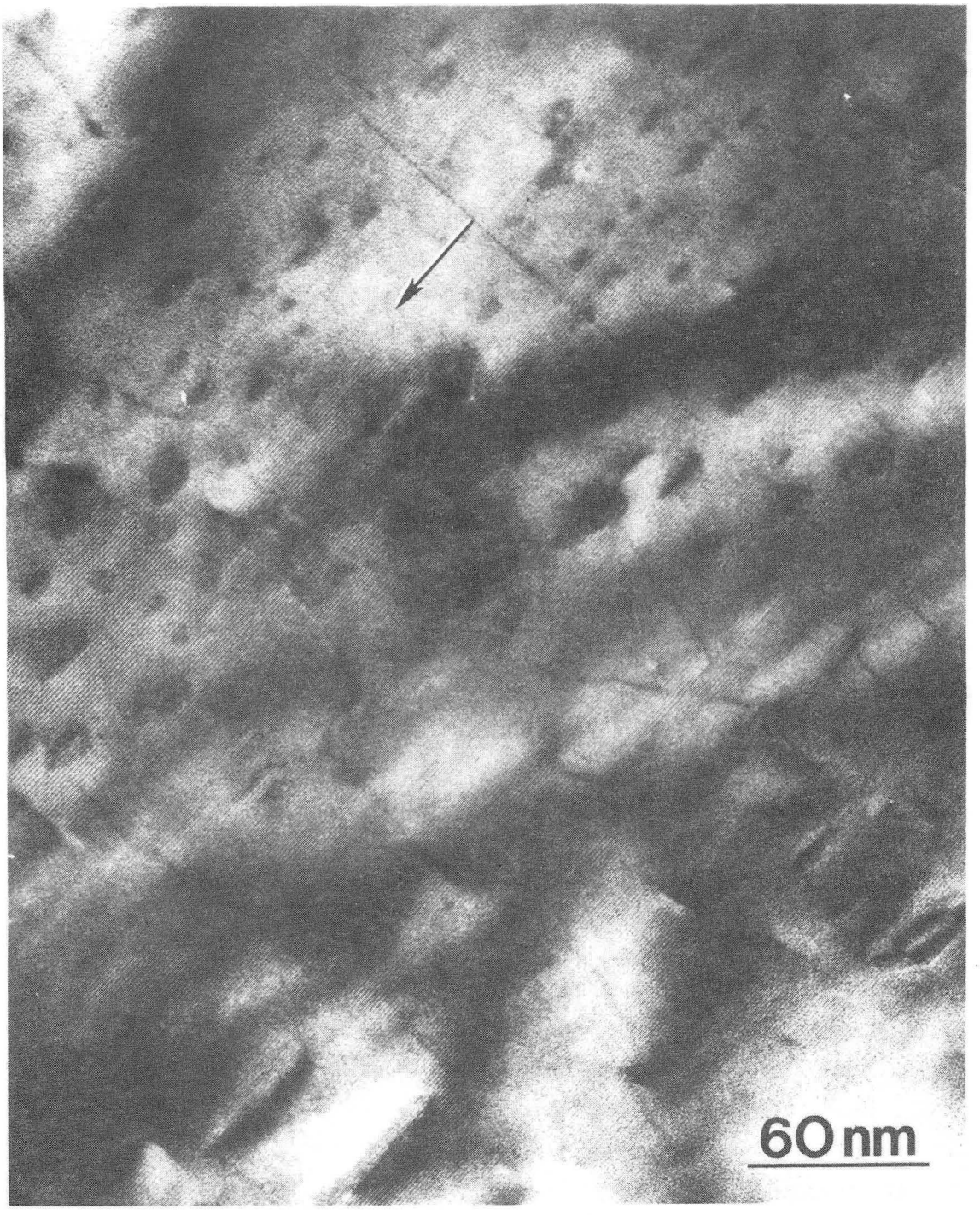

Fig. 10.10 HRTEM image of low chalcocite film in [010] zone-axis orientation. Note wandering (1/110) boundaries. Flat (1/110) boundaries are due to basal slip of sublattice dislocations. Arrow indicates [001] direction.
XBB 820-10669A

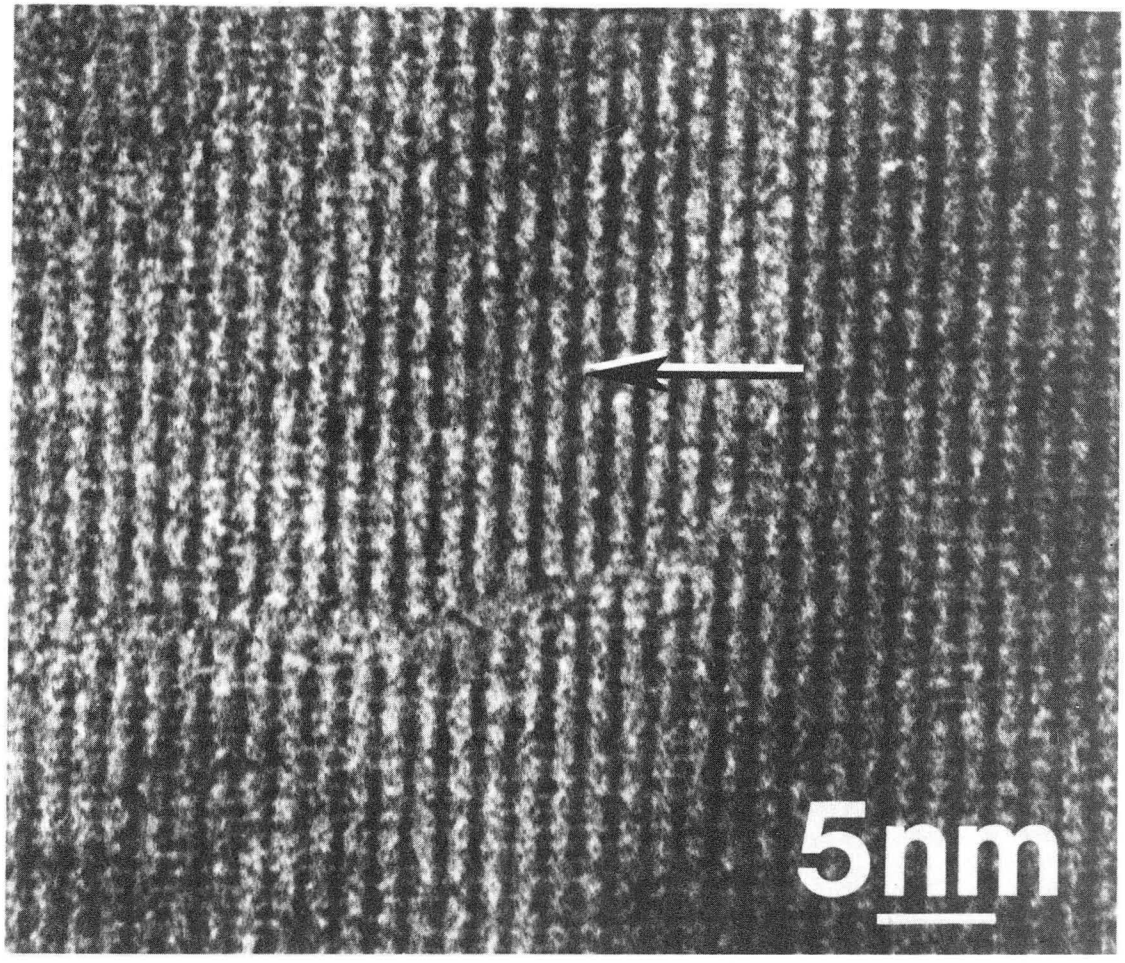

Fig. 10.11 HRTEM image of low chalcocite in [010] zone-axis orientation. Note 1/4[201] antiphase boundary. Arrow indicates [201] direction. XBB 843-1724

10.3 High Chalcocite and "Protodjurleite": The Transition State

Ordinary beam heating of copper sulfide thin films in the TEM is sufficient to raise the local specimen temperature to above 100°C. This fact makes the TEM a convenient tool for the study of order-disorder phenomena in $Cu_{2-x}S$.

For compositions very close to Cu_2S, the extent of the two-phase region between the order-disorder "solidus" and "liquidus" is small so that one can observe the rapidly reversible order-disorder transition by manipulating the fine control of the second condenser lens. The observation can be made either in real space (high resolution) or in diffraction. Figure 10.12 consists of a pair of basal diffraction patterns from the same area of a Cu_2S film. At this illumination level, a single ultrafine increment of condenser lens current was sufficient to complete the transition. Repeated cycles revealed the three sets of discernible orientation variants, often in a cyclic fashion and with no detectable hysteresis. The haloes of radius ~1/12 $Å^{-1}$ about $0\bar{1}10$-type high chalcocite spots are representative of the high chalcocite transition state. The geometry of these diffuse intensity contours can be interpreted in terms of cation clusters.[99]

Specimens with (2-x) between 1.97 and 1.99 show a somewhat more complicated behavior. For these compositions, the two-phase region between "solidus" and "liquidus" is approximately 3°C wide. Consequently, the transition is more gradual and should result in a two-phase mixture of low chalcocite and djurleite ($Cu_{1.965}S$). Figure 10.13 shows such a transition. The high chalcocite phase (Fig.

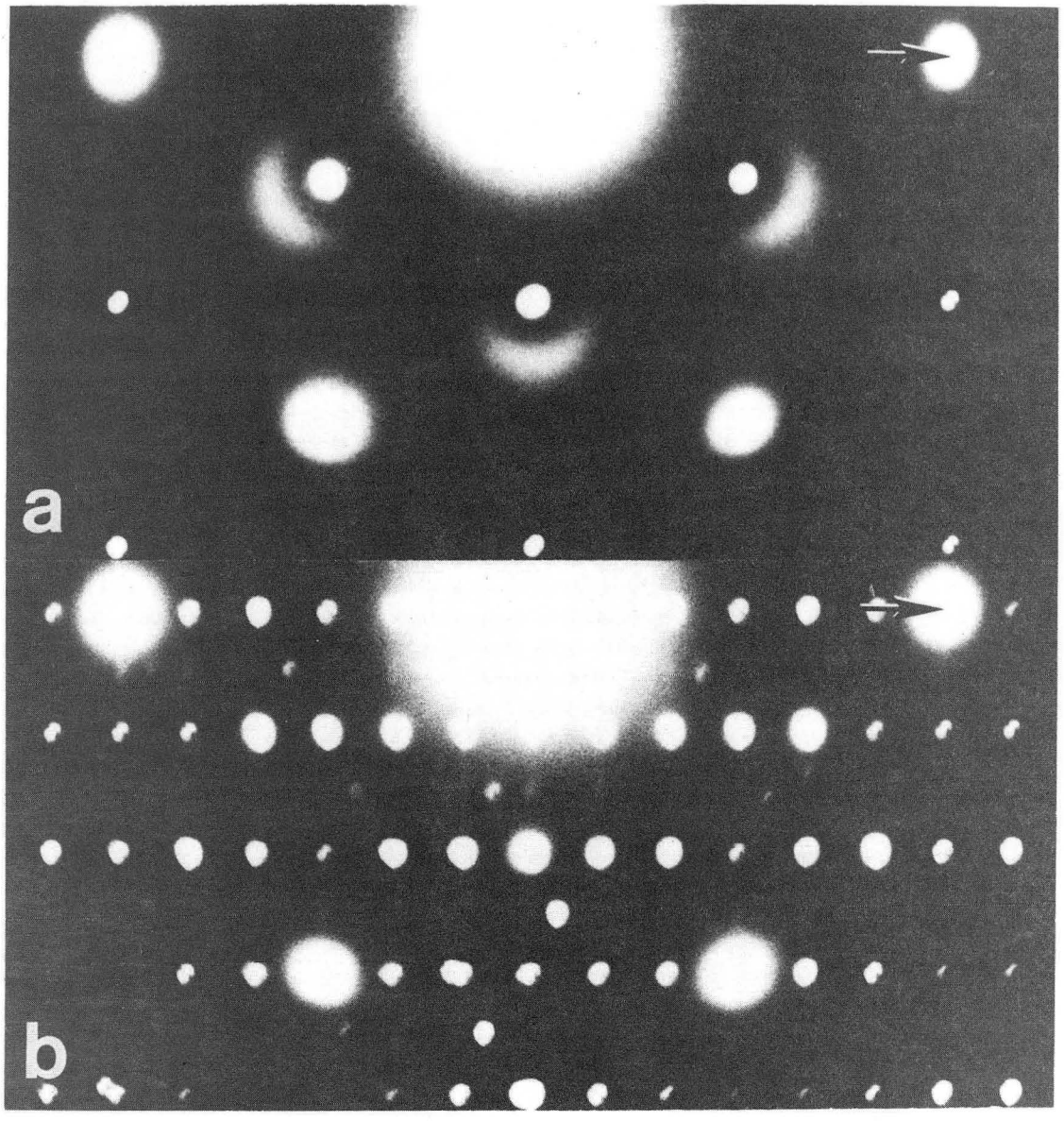

Fig. 10.12 Transmission electron diffraction patterns showing order-disorder transformation in chalcocite ([001] zone-axis orientation). Arrow in a) points to $\bar{2}110$ spot of high chalcocite. Arrow in b) points to 060 spot of low chalcocite. XBB 833-2664A

Fig. 10.13 Transmission electron diffraction patterns showing cooling sequence from high chalcocite (a) to mixture of low chalcocite and djurleite (d). Note $2a_h$ pattern of protodjurleite in b). Arrow in a) points to $\bar{2}110$ spot of high chalcocite. Arrow in d) points to 080 and 046 spots of two djurleite variants and 630 spot of one low chalcocite variant. Low chalcocite and djurleite are in [001] and [100] zone-axis orientations, respectively.

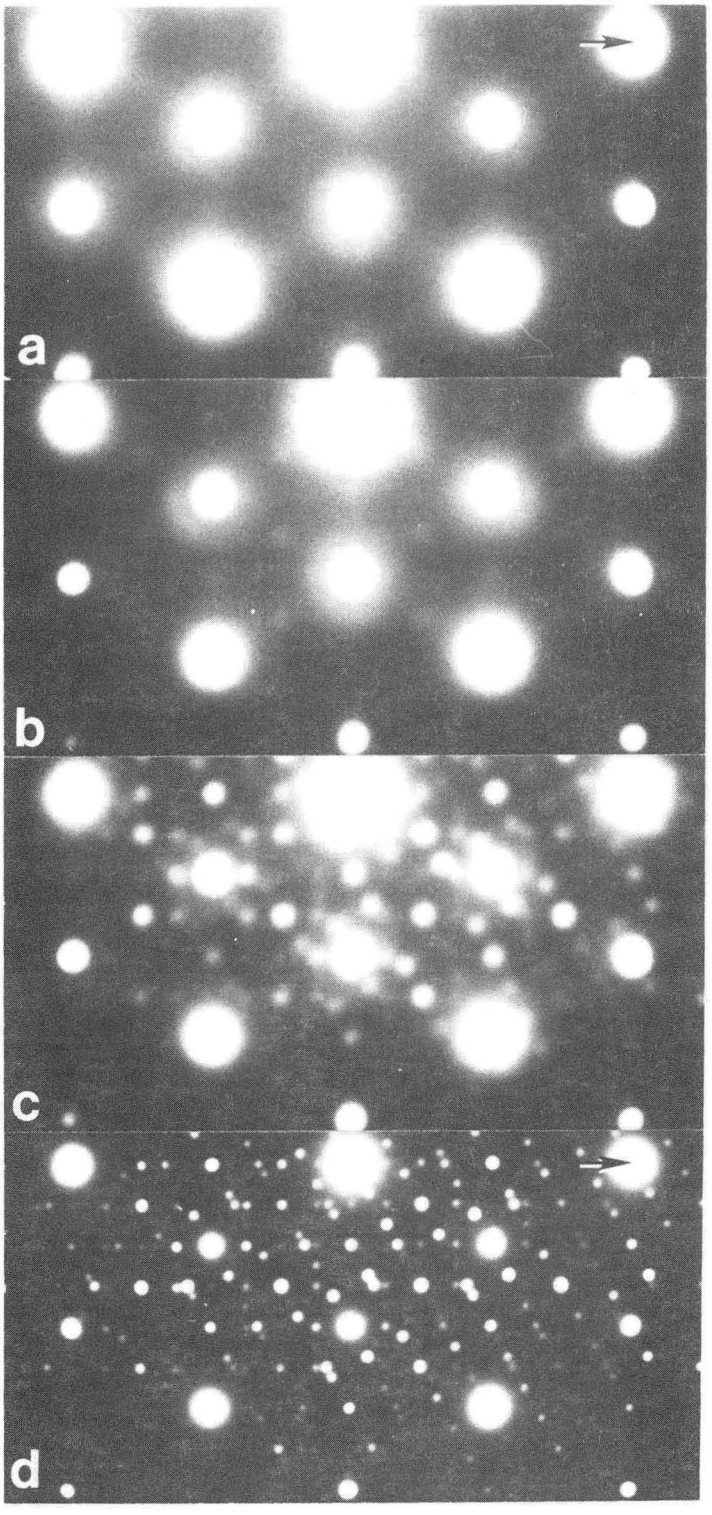

XBB 833-2663A

10.13a) shows some diffuse scattering on lines or planes connecting the main spots. Slight cooling intensifies the 1/12 $Å^{-1}$ haloes. In addition, spots at the 2 a_{hex} positions appear, forming what is known as the "protodjurleite" phase.[25,65] This phase is suspected to be a metastable super-cooled version of djurleite with a composition of approximately $Cu_{1.970}S$.[100] A laser grating consisting of a djurleite microdomain model gives an optical diffraction pattern with the same qualitative features. Thus, protodjurleite may not be a distinct phase. The microdomain model is being tested with HRTEM. Further cooling results in the formation of several orientation variants of low chalcocite and djurleite (Fig. 10.13d).

Figure 10.14 is a pair of diffraction patterns obtained from a region tilted 21° from [0001] about $[0\bar{1}10]$. The geometry of the diffuse scattering strongly suggests that the haloes are intersections of cylinders parallel to [0001]* and that the diffuse scattering between the main spots is in the form of walls of intensity containing the [0001]* direction. Thus, the transition state is characterized by ordering of copper within the basal layers rather than ordering in the [0001]* direction.

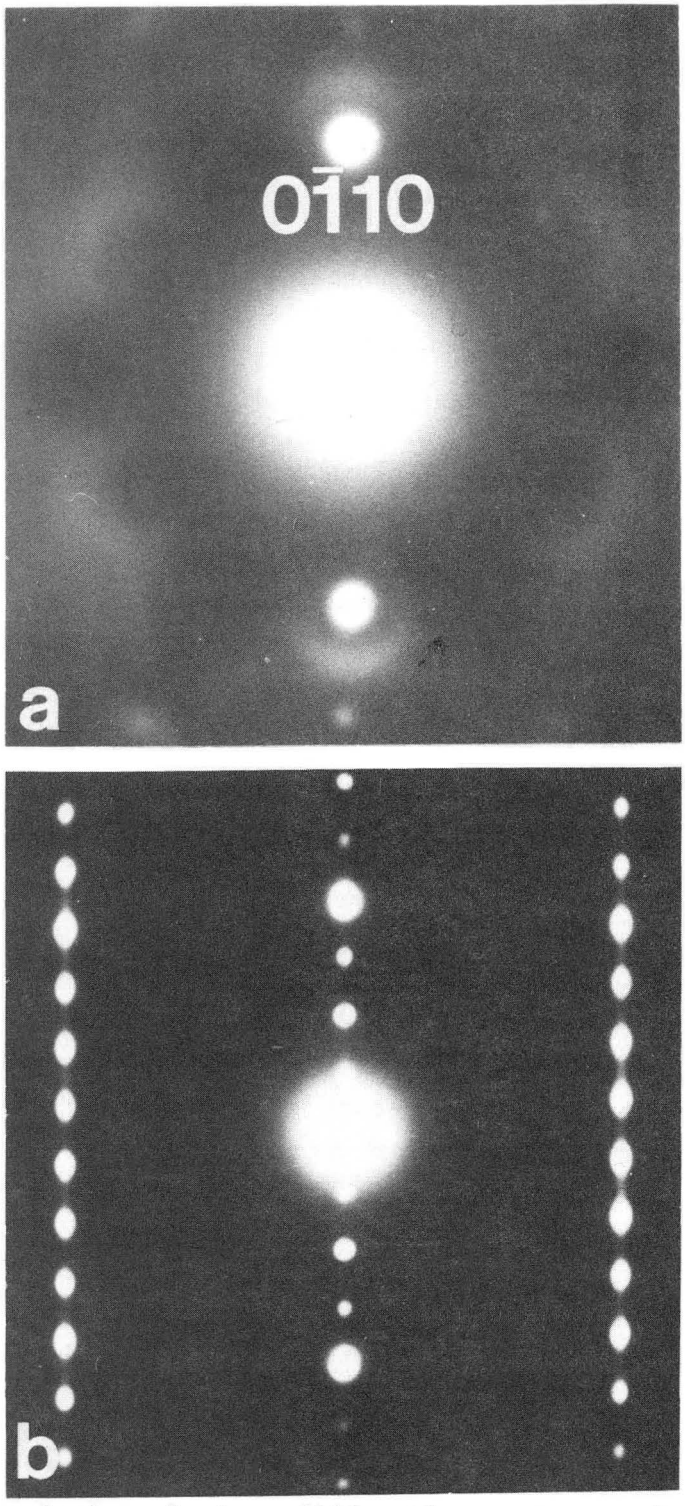

Fig. 10.14 Transmission electron diffraction patterns of a) high chalcocite and b) low chalcocite tilted ~21° about [0$\bar{1}$10] from [0001] zone-axis orientation. Geometry of diffuse intensity suggests that walls of intensity contain [0001]* direction. XBB 833-2666A

11. REFERENCES

1. S. Oktik, G. J. Russell and J. Woods, Solar Energy Mat. 9, 77 (1983).
2. L. D. Partain, P S. McLeod, J. A. Duisman, T. M. Peterson, D. E. Sawyer and C. S. Dean, J. Appl. Phys. 54, 6708 (1983).
3. M. A. Green, "Solar Cells," Prentice-Hall, Englewood Cliffs, N.J. (1982).
4. S. J. Fonash, "Solar Cell Device Physics," Academic Press, New York (1981).
5. Ibid, ch. 5.
6. R. L. Anderson, Solid-St. Electron. 5, 341 (1962).
7. J. J. Loferski, J. Appl. Phys. 27, 777 (1956).
8. J. H. van der Merwe and C. A. B. Ball in "Epitaxial Growth-Part B," Academic Press, New York, 494 (1975).
9. T. Peterson and J. Washburn, phys. stat. sol. (a) 22, 721 (1974).
10. D. C. Reynolds, G. Leies, L. L. Antes and R. E. Marburger, Phys. Rev. 92, 53 (1954).
11. D. A. Cusano, Solid-St. Electron. 6, 217 (1963).
12. A. E. Carlson, WADC Tech. Rep., Clevite Corp., 1956, p. 56.
13. L. R. Shiozawa, G. A. Sullivan and F. Augustine, Proc. 7th IEEE Photovoltaic Spec. Conf., IEEE, New York, 1968, p. 39.
14. J. A. Bragagnolo, A. M. Barnett, J. E. Phillips, R. H. Hall, A. Rothwarf and J. D. Meakin, IEEE Trans. Electron Dev. ED-27, 645 (1980).
15. R. Hill, Solid-St. and Electron Dev. 2, S49 (1978).

16. S. Martinuzzi, Solar Cells 5, 243 (1982).

17. G. A. Roderick, Proc. 3rd Comm. of European Communities Conf. on Photovoltaic Solar Energy, Reidel, Dordrecht, 1980, p. 327.

18. E. Eser and R. B. Hall, Thin Solid Films 86, 31 (1981).

19. H. J. Hovel, "Semiconductors and Semimetals--Vol. II: Solar Cells," Academic Press, New York (1975).

20. A. G. Stanley, Appl. Solid-St. Sci. 5, 251 (1975).

21. N K. Mukherjee, F. Pfisterer, C. H. Hewig, H.-W. Schock and W. H. Bloss, J. Appl. Phys. 48, 1538 (1977).

22. B. Baron, A. W. Catalano, and E. A. Fagen, Proc. 13th IEEE Photovoltaic Spec. Conf, IEEE, New York, 1978, p. 406.

23. S. Salkalachen, S. Jatar, A. C. Rastogi, and V. G. Bhide, Solar Cells 3, 341 (1981).

24. F. Pfisterer, H.-W. Schock and J. Worner, Proc. 3rd Comm. of European Communities Conf. on Photovoltaic Solar Energy, Reidel, Dordrecht, 1980, p. 762.

25. R. W. Potter, Econ. Geology 72, 1524 (1977).

26. N. Convers Wyeth and A. W. Catalano, Proc. 12th IEEE Photovoltaic Spec. Conf., IEEE, New York, 1976, p. 471.

27. B. G. Caswell, G. J. Russell and J. Woods, J. Phys. D: Appl. Phys. 10, 1345 (1977).

28. T. Sands, M. S. Thesis, University of California, Berkeley, Nov. 1981, p. 8 (LBL-13659).

29. K. Bogus and S. Mattes, Proc. 9th IEEE Photovoltaic Spec. Conf., IEEE, New York, 1972, p. 106.

30. H. J. Mathieu, K. K. Reinhartz, and H. Rickert, Proc. 10th IEEE Photovoltaic Spec. Conf., IEEE, New York, 1973, p. 93.

31. B. G. Caswell, G. J. Russell and J. Woods, J. Phys. D: Appl. Phys. 8, 1889 (1975).

32. A. Rothwarf, J. Phillips, and N. Convers Wyeth, Proc. 13th IEEE Photovoltaic Spec. Conf., IEEE, New York, 1978, p. 399.

33. F. Pfisterer, H.-W. Schock and W. H. Bloss, Proc. 12th IEEE Photovoltaic Spec. Conf., IEEE, New York, 1976, p. 502.

34. C. H. Cheng, B. Merritt, C. W. Tu and K. A. Jones, Solar Cells 10, 287 (1983).

35. E. Eser, Solar Cells 8, 157 (1983).

36. G. H. Hewig and W. H. Bloss, Proc. 12th IEEE Photovoltaic Spec. Conf., IEEE, New York, 1976, p. 483.

37. G. A. Wolff, J. J. Frawley and J. R. Hietanen, J. Electrochem. Soc. 111, 22 (1964).

38. W. H. Strethlow, J. Appl. Phys. 41, 1810 (1970).

39. C. H. Cheng and K. A. Jones, J. Electrochem. Soc. 127, p. 1375 (1980).

40. K. A. Jones, C. H. Cheng, and B. F. Shirreffs, Proc. 13th IEEE Photovoltaic Spec. Conf., IEEE, New York, 1978, p. 513.

41. L .C. Burton and H. M. Windawi, J. Appl. Phys. 47, 4621 (1976).

42. L. Hmurcik and R. A. Serway, J. Appl. Phys. 53, 9073 (1982).

43. T. teVelde, Solid St. Electron. 16, 1305 (1973).

44. H. M. Windawi, Proc. 11th IEEE Photovoltaic Spec. Conf., IEEE, New York, 1975, p. 46.

45. H. M. Windawi, International Workshop: CdS Solar Cells and Other Abrupt Heterojunctions, University of Delaware, 1975, p. 177.

46. B. G. Caswell and J. Woods, phys. stat. sol. (a) 44, K47 (1977).

47. W. Palz, J. Besson, T. Nguyen Duy, and J. Vedel, Proc. 9th IEEE Photovoltaic Spec. Conf., IEEE, New York, 1972, p. 91.

48. W. Cook, L. Shiozawa, and F. Augustine, J. Appl. Phys. 41, 3058 (1970).

49. J. Besson, T. Nguyen Duy, A. Gauthier, W. Palz, C. Martin and J. Vedel, Proc. 11th IEEE Photovoltaic Spec. Conf., IEEE, New York, 1975, p. 468.

50. R. J. Mytton, L. Clark, R. W. Gale, and K. Moore, Proc. 9th IEEE Photovoltaic Spec. Conf., IEEE, New York, 1972, p. 133.

51. A. C. Rastogi and S. Salkalachen, Solar Cells 9, 185 (1983).

52. G. J. Russell and J. Woods, phys. stat. sol. (a) 46, 433 (1978).

53. J. Echigoya and J. W. Edington, phys. stat. sol. (a) 72, 304 (1982).

54. T. D. Sands, J. Washburn and R. Gronsky, phys. stat. sol. (a) 72, 551 (1982).

55. T. D. Sands, R. Gronsky, and J. Washburn, Proc. 16th IEEE Photovoltaic Spec. Conf., IEEE, New York, 1982, p. 862.

56. D. B. Holt and D. M. Wilcox, J. Crystal Growth 9, 193 (1971).

57. E. H. Roseboom Jr., Econ. Geology 61, 641 (1966).

58. S. S. Devlin, J. M. Jost, and L. R. Shiozawa, Tech. Rept. WADD-TR-60-11 (PB161938), 1960, p. 157.

59. S. Djurle, Acta Chem. Scand. 12, 1415 (1958).

60. H. T. Evans, Jr., Nature Phys. Sci. 232, 69 (1971).

61. H. T. Evans, Jr., Z. Krist, 150, 299 (1979).

62. H. T. Evans, Jr., Science 203, 356 (1979).

63. N. Morimoto and G. Kullerud, Am. Mineralogist 48, 110 (1963).

64. A. Janosi, Acta Cryst. 17, 311 (1964).

65. A. Putnis, Am. Mineralogist 62, 107 (1977).

66. C. Manolikas, P. Delavignette and S. Amelinckx, phys. stat. sol. (a) 33, K77 (1976).

67. C. Conde, C. Manolikas, D. van Dyck, P. Delavignette, J. van Landuyt and S. Amelinckx, Mat. Res. Bull. 13, 1055 (1978).

68. M. J. Buerger and B. J. Wuensch, Science 141, 276 (1963).

69. R. Sadanaga, M. Ohmasa, and N. Morimoto, Miner. J. (Japan) 4, 275 (1965).

70. B. J. Mulder, Kristall und Technik 8, 825 (1973).

71. H. T. Evans, Jr., Am. Mineralogist 66, 807 (1981).

72. J. A. Tossell, Phys. Chem. Minerals 2, 225 (1978).

73. N. Morimoto and K. Koto, Am. Mineralogist 55, 106 (1970).

74. D. van Dyck, C. Conde and S. Amelinckx, phys. stat. sol. (a) 56, 327 (1979).

75. D. van Dyck, C. Conde-Amiano, and S. Amelinckx, phys. stat. sol. (a) 58, 451 (1980).

76. B. J. Skinner, Econ. Geology 65, 724 (1970).

77. F. Dachille and R. Roy, Nature 186, 34 and 71 (1960).

78. T. Kanashiro, T. Ohno, M. Satoh, K. Okamoto, A. Kojima, and F. Akao, Solid State Ionics 3/4, 327 (1981).

79. A. C. Rastogi, S. Salkalachen and V. G. Bhide, Thin Solid Films 52, 1, (1978).

80. J. J. Loferski, J. Shewchun, E. A. DeMeo, R. Arnott, E. E. Crisman, R. Beaulieu, H. L. Hwang, and C. C. Wu, Proc. 12th IEEE Photovoltaic Spec. Conf., IEEE, New York, 1976, p. 496.

81. F. A. Shirland, J. Appl. Phys. 50, 4714 (1979).

82. Sir P. Hirsch, A. Howie, R. B. Nicholson, D. W. Pashley, and M. J. Whelan, "Electron Microscopy of Thin Crystals," Robert E. Krieger Pub. Co., Malabar, Florida (1977).

83. G. Thomas and M. J. Goringe, "Transmission Electron Microscopy of Materials," John Wiley and Sons, New York (1979).

84. J. C. H. Spence, "Experimental High-Resolution Electron Microscopy," Claredon Press, Oxford (1981).

85. J. W. Edington, "Practical Electron Microscopy in Materials Science, Vol. 2, Electron Diffracton in the Electron Microscope," Philips Technical Library, Eindhoven (1975).

86. R. Gronsky in Treatise on Materials Science and Technology, Vol. 19B, H. Herman (Ed.), Academic Press, New York (1983), p. 325.

87. C. Kittel, "Introduction to Solid State Physics," 5th Edition, John Wiley and Sons, New York (1976), Chapt. 2.

88. G. Thomas and M. J. Goringe, "Transmission Electron Microscopy of Materials," John Wiley and sons, New York (1979), p. 315.

89. O. J. Scherzer, J. Appl. Phys. 20, 20 (1949).

90. O. L. Krivanek, Optik 45, 97 (1976).

91. U. Dahmen, Acta Met. 30, 63 (1982).

92. U. Dahmen and K. H. Westmacott, Proc. of an International Conf. on Solid--Solid Phase Transformations, AIME, New York, 1982, p. 433.

93. F. Arjona, F. Rueda, E. García-Camarero, M. León and L. Arizmondi, 12th IEEE Photovoltaic Spec. Conf., IEEE, New York, 1976, p. 515.

94. D. T. Rickard, TMPM Tschermaks Min. Petr. Mitt. 19, 60 (1973).

95. A. W. Czanderna, E. T. Prince, and H. F. Helbig, Proc. SPIE, Vol. 248, SPIE, Bellingham, Washington, 1980, p. 74.

96. J. W. Christian, "The Theory of Transformations in Metals and Alloys," 2nd Ed., Part I, Pergamon, Oxford (1975), p. 153.

97. K. Koto and N. Morimoto, Acta Cryst. B26, 915 (1970).

98. M. Guymont, D. Gratias, R. Portier, and M. Fayard, phys. stat. sol (a) 38, 629 (1976).

99. R. de Ridder, G. Van Tendeloo, D. van Dyck and S. Amelinckx, phys. stat. sol. (a) 38, 663 (1976).

100. B. J. Mulder, phys. stat. sol. (a) 18, 633 (1973).

TECHNICAL INFORMATION DEPARTMENT
LAWRENCE BERKELEY LABORATORY
UNIVERSITY OF CALIFORNIA
BERKELEY, CALIFORNIA 94720